research report

Advancing Seismic Simulation of Cold-Formed Steel Framed Buildings

Report RP15-3

July 2015

American Iron and Steel Institute

DISCLAIMER

The material contained herein has been developed by researchers based on their research findings and is for general information only. The information in it should not be used without first securing competent advice with respect to its suitability for any given application. The publication of the information is not intended as a representation or warranty on the part of the American Iron and Steel Institute or of any other person named herein, that the information is suitable for any general or particular use or of freedom from infringement of any patent or patents. Anyone making use of the information assumes all liability arising from such use.

VIRGINIA POLYTECHNIC INSTITUTE AND STATE UNIVERSITY

The Charles E. Via, Jr. Department of
Civil and Environmental Engineering
Blacksburg, VA 24061

Structural Engineering and Materials

ADVANCING SEISMIC SIMULATION OF COLD-FORMED STEEL FRAMED BUILDINGS

by

David A. Padilla-Llano, Ph.D.
Graduate Research Assistant

Chu Ding, M.Sc.
Graduate Research Assistant

Cristopher D. Moen, Ph.D., P.E.

Matthew R. Eatherton, Ph.D., P.E., S.E.

Report No. CE/VPI-ST-15/05

July 2015

Summary

The objective of this research is to create a computationally efficient seismic analysis framework for cold-formed steel (CFS) framed-buildings supported by hysteretic nonlinear models for CFS members and screw-fastened connections. Design of CFS structures subjected to lateral seismic forces traditionally relies on the strength of subassemblies subjected to lateral loading of systems, such as strapped/sheathed shear walls and diaphragms, to provide adequate protection against collapse. Enabling performance-based seismic design of CFS buildings requires computationally efficient and accurate modeling tools that predict the nonlinear cyclic behavior of CFS buildings, the individual CFS components and connections. Such models should capture the energy dissipation and damage due to buckling and cross-sectional deformations in thin-walled CFS components subjected to cyclic loads such as those induced by earthquakes. Likewise, models for screw-fastened CFS connections should capture the energy dissipation and damage due to tilting, bearing, or screw shear when subjected to cyclic loading.

In this dissertation, an analysis framework for CFS structures that captures the nonlinear cyclic behavior of critical components including axial members, flexural members, and screw fastened connections is presented. A modeling approach to simulate thin-walled behavior in CFS members is introduced where parameters were developed using results from an experimental program that investigated the cyclic behavior and energy dissipation in CFS axial members and flexural members. Energy dissipation and cyclic behavior of CFS members were characterized for members experiencing global, distortional and local buckling. Cyclic behavior and energy dissipation in thin steel plates and members was further investigated through finite element analysis in ABAQUS to provide a strategy for modeling steel columns cyclic behavior including local buckling. Model parameters were developed as generalized functions of the hysteretic energy dissipated and slenderness. The capabilities of the analysis framework are demonstrated through simulations of CFS wood sheathed shear wall cyclic responses validated with experimental results from full scale shear wall tests.

An ABAQUS user element (UEL) is provided for simulating CFS screw-fastened connections that was verified against experimental responses. The connection model is employed in CFS sheathed shear wall simulations of recent monotonic and cyclic experiments where each screw-fastened connection is represented by UEL.

Table of Contents

List of Figures

List of Tables

Chapter 1: Introduction

The objective of this research work is to develop a computationally efficient analysis framework for cold-formed steel (CFS) framed buildings subjected to extreme loading (e.g., seismic loading) supported by hysteretic nonlinear models that can capture the nonlinear cyclic behavior of all the critical components. The steel industry increasing interest on using cold-formed steel for multi-story building construction able to withstand extreme loads such as earthquake induced lateral loads, requires development of analysis tools and guidelines that allow flexibility in modeling and safe design of actual CFS structures. Furthermore, the shift towards performance-based earthquake engineering has created considerable interest in understanding and controlling building seismic performance at different seismic hazard levels. Current analysis and prescriptive design procedures for CFS lateral load-resisting systems (e.g., steel/wood sheathed CFS shear walls and diaphragms), are expected to provide adequate protection against collapse [1], but lack the ability to predict and design for performance levels. These prescriptive procedures provide no information about energy dissipation, strength degradation, and stiffness degradation of these systems and their components (e.g., floor joists, drag struts and boundary chord studs). They also neglect the resistance from other CFS components that are not part of the lateral-load resisting system (e.g., gravity load supporting walls).

To develop seismic performance factors (i.e., R, Ω_0, and C_d) and include different hazard levels in addition to collapse, it is necessary to consider ground motions suites, many ground motion intensities, as well as, different structural layouts [2]. This in turn translates into a sizable number of analyses (i.e., thousands of nonlinear response history analyses) that require computationally efficient and reasonably accurate modeling tools. These tools should allow flexibility on modeling different structural layouts and capture the energy dissipation and the major response characteristics in CFS systems (e.g., shear walls, diaphragms), their components (i.e., studs and joists) and connections subjected to cyclic loading. Developing such models requires characterizing the cyclic behavior and energy dissipation in CFS systems, members and connections through experiments and analysis.

Research efforts to understand seismic behavior of cold-formed steel structures traditionally focus on studies of shear wall response. These include experimental and analytical

studies of the most common CFS shear wall configurations used in construction including wood, steel or gypsum sheathed and steel strapped shear walls (e.g., [3-14]). More recent efforts grouped under the CFS-NEES projects, seek to advance understanding in the seismic behavior of cold-formed steel buildings and the building blocks (e.g., members, connections, shear walls, floor diaphragm) for developing nonlinear models and response history analysis [15]. These projects include shear wall tests [6,7,12,13], characterization of sheathing to steel connections [16,17], characterization of moment-rotation responses including the post-buckling part of the response in CFS flexural members exhibiting local and distortional buckling [18], and the recently completed shake table tests of the full scale CFS-NEES building that was subjected to various ground motions at different stages of construction to evaluate the different structural element contributions to the seismic response [19,20]. Detailed background information pertinent to the research presented in this dissertation is summarized in the corresponding chapters.

Within this framework towards a better understanding of CFS building seismic behavior, there is still a need to expand the knowledge of the behavior at the more basic levels, i.e., member cyclic behavior including buckling deformations, screw-fastened connections behavior, and how they contribute to systems (e.g., shear walls, diaphragms) energy dissipation, and overall building response. Understanding at the member and connection level facilitates consideration of different structural layouts, lateral-force resisting systems, and hazard levels in analysis and design. For example, the cold-formed steel structure in Fig. 1.1 comprises numerous CFS members forming shear walls, floor diaphragms and gravity load carrying walls that during an earthquake are subjected to cyclic axial and flexural loads. The seismic behavior and performance of this building can be assessed using computationally efficient models that account for the behavior of the individual components (i.e., joist, studs, and connections). In Fig. 1.1 for instance, joists, studs and connections can be modeled using nonlinear hysteretic models that are assembled to simulate the cyclic behavior of the whole building. This dissertation introduces a computationally efficient component based analysis framework for cold-formed steel framed buildings supported by nonlinear hysteretic models for CFS members and screw-fastened connections. The proposed analysis framework contributes to advancing performance-based seismic analysis and design of cold-formed steel framed buildings.

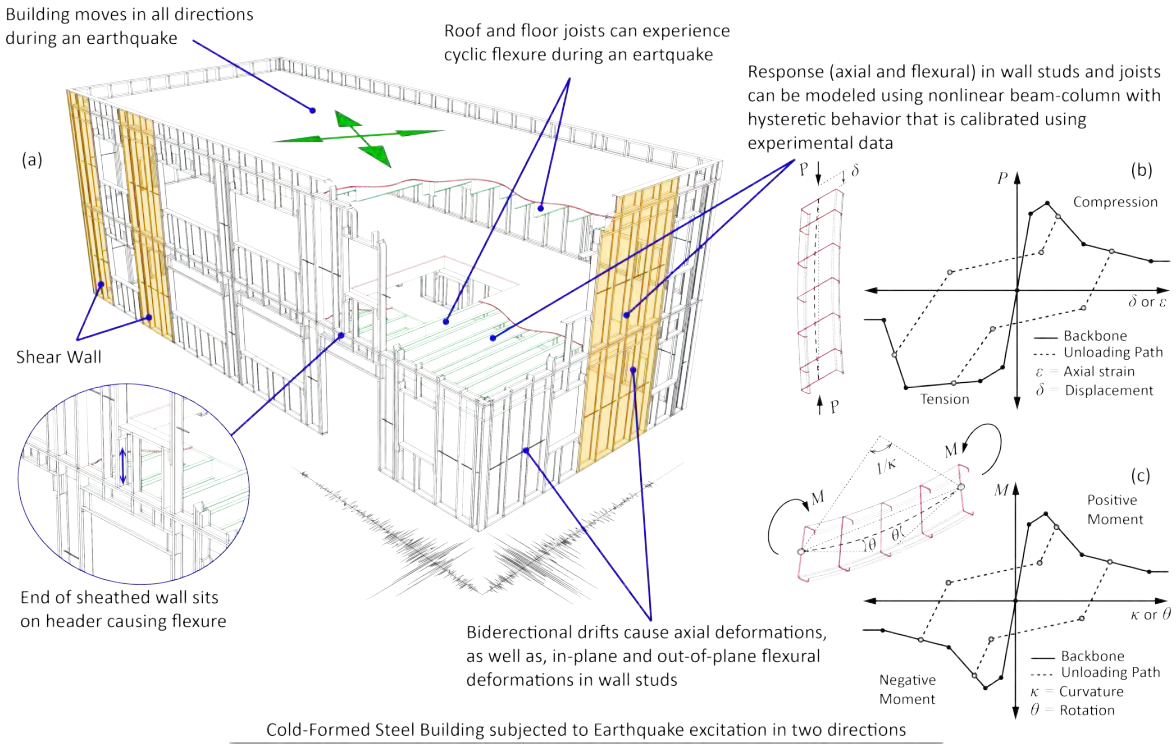

Fig. 1.1. Cold-formed steel framing members experience cyclic axial and flexure forces during earthquake excitations (adapted from CFS-NEES building model [19]) with behavior that can be represented by phenomenological models [21].

Thin-walled cold-formed steel members subjected to compressive stresses are prone to inelastic buckling deformations that reduce stiffness and affect their post-peak strength behavior. When subjected to cyclic loading, buckling deformations reverse and combine with yielding strains in tension at the highly stressed locations. Energy dissipates through accumulation of these inelastic strains that can lead to fracture and tearing of the material (see Fig. 1.2).

The types of buckling deformations experienced by thin-walled members are different depending on the geometry and elastic buckling properties. For common cold-formed steel members the AISI Direct Strength Method (DSM) [22] identifies three types of buckling limit states: global (Fig. 1.2a and 1.2d), distortional (Fig. 1.2b and 1.2e), and local buckling (Fig. 1.2c and 1.2f). Depending on which of these limit states governs, the distribution (or concentration) of inelastic strains as well as cyclic strength and stiffness deterioration may vary. For example Fig. 1.2a shows inelastic strains due to buckling of the stiffening lips in a CFS stud experiencing global buckling while Fig. 1.2f shows inelastic strains concentration from local buckling in the web of a CFS joist subjected to uniform bending. Characterizing the relationship between the different types of buckling deformations and the cyclic behavior is one of the objectives of this

research towards providing the analytical tools for the seismic analysis framework for CFS structures.

Fig. 1.2. Cold-formed steel member failure modes: (a) global buckling in axial member; (b) distortional buckling in axial member; (c) local buckling in axial member; (d) global buckling in flexural member; (e) distortional buckling in flexural members; (f) local buckling.

Two approaches are introduced in this dissertation to model the cyclic response of cold-formed steel axial and flexural members experiencing local, distortional and global buckling deformations: a *nonlinear spring* model with concentrated nonlinear *axial load-displacement* (*P-δ*) or *moment-rotation* (*M-θ*) behavior, and a *nonlinear beam-column* with distributed nonlinear section *axial load-strain* (*P-ε*) or *moment-curvature M-κ* behavior. Model parameters are derived as functions of the hysteretic energy dissipated, unbraced length, and member elastic buckling properties. These models are then used together with a nonlinear spring model for screw-fastened connections to illustrate the capabilities of simulation framework.

Single screw-fastened CFS connections subjected to cyclic shear deformations fail due to fastener tilting; bearing; tearing; screw shearing, screw pull out, screw shear+tension fracture; or a combination of two or more of this limits (see Fig. 1.3). Energy dissipation occurs as the hole elongates due to bearing stresses and/or tearing of the connected pieces material around the hole. A *nonlinear spring* model is used to simulate the behavior of the CFS single screw-fastened connections.

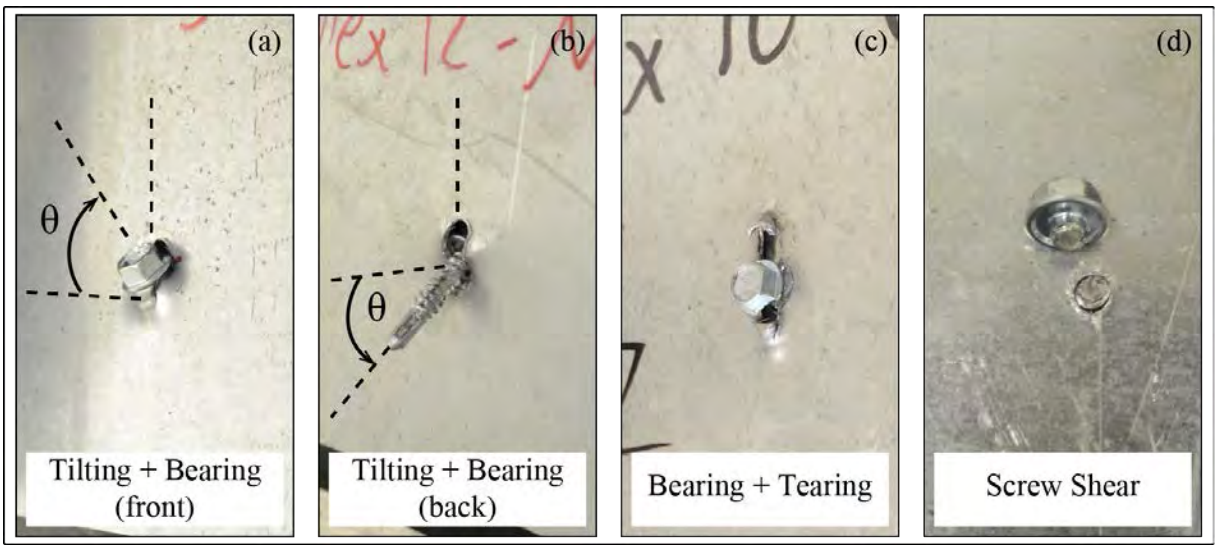

Fig. 1.3. Failure modes in single fastened cold-formed steel connection: (a,b) tilting + bearing hear; (c) bearing + tearing; (d) screw shear.

The research progression starts with Chapter 2 studying the energy dissipation in thin plates subjected to axial and flexural cyclic loading. The study provides insight on the cyclic behavior of thin-walled cross-section elements, such as webs and stiffened elements. The effects of slenderness, imperfections, and loaded end boundary conditions on the cyclic response and energy dissipation are explored through nonlinear finite element modeling in ABAQUS [23].

Chapter 3 describes a framework to model cyclic behavior in thin-walled cold-formed steel axial and flexural members. The approach for CFS members described in Chapter 3 is specialized in Chapter 4 to model the axial cyclic behavior in steel columns including local buckling. The library *asymPinching* is implemented for OpenSees [24] or MATLAB [25] that allows for the approximate simulation of local buckling in cyclic frame-type analyses. In Chapter 5, An ABAQUS user element (UEL) is provided for simulating CFS screw-fastened connections and illustrated in simulating CFS sheathed shear wall simulations. This research concludes in Chapter 6 demonstrating the potential of the nonlinear *asymPinching* model for CFS members in the analysis of CFS shear walls that are validated against experimental responses of wood-sheathed shear walls used in the CFS-NEES building [19,20] tested at the University of North Texas [12,13]. Summaries of literature pertinent to the research presented in this dissertation are summarized in the corresponding chapters as needed.

Additional information that supplements the work in this research is supplied in the appendices. Appendix A describes the background and reasoning for developing the displacement-controlled loading protocol used in the cyclic response simulations. The MATLAB version code for the *asymPinching* is provided in Appendix B. The results of user element (UEL) verification examples for screw-fastened simulations in ABAQUS are summarized in Appendix B. And the code implementing the user element in FORTRAN is provided in Appendix D.

Chapter 2: Cyclic Behavior and Energy Dissipation in Cold-Formed Steel Thin-Walled Members

In this chapter, cyclic behavior and energy dissipation in thin steel plates are studied through nonlinear finite element modeling to explore answers to the research questions: 1) *What are the energy dissipation mechanisms in cold-formed steel members?* and 2) *How do damage and inelastic strains accumulate during cyclic loading?*. The results from this study provide insights into the cyclic behavior of thin-walled cross-section elements (e.g., webs and stiffened elements) subjected to stresses from axial and flexural loading.

Thin-walled cold-formed steel members subjected to compressive stresses experience buckling deformations that will reduce their stiffness and affect the post-peak behavior. As the applied compressive stresses increase, these buckling deformations appear and their effects translate to the axial load-deformation curve by changes in stiffness and peak-strength values. For example, Fig. 2.2 compares the response of two axially loaded studs with fixed ends subjected on the top to a displacement δ. This figure shows that the more slender member (λ_ℓ =2.04) shows larger buckling deformations that translate into smaller pre-peak stiffness (segment *a*-*b* vs. segment *d*-*e*) and peak strength compared to the less slender stud, λ_ℓ =1.14, [$\lambda_\ell = (P_y/P_{cr\ell})^{0.5}$, $P_y=AF_y$, F_y=yield stress, A=cross-section area, $P_{cr\ell}$=local buckling load]. Depending on the elastic buckling properties and yield stress, these buckling deformations will be reversible (i.e., elastic) or will include permanent plastic strains. As the member reaches its maximum strength, inelastic deformations spread across the mid-height cross-section so that the response beyond this point softens with a gradually decreasing negative stiffness and inelasticity spreading along the member (see *b*, *e*, *c*, and *f* in Fig. 2.2). Whether the post peak strength decreases more or less gradually depends on the properties (slenderness) of the member as illustrated in Fig. 2.2. The drop in strength from peak strength (20% drop) is steeper for the less slender member (point *b* to *c*) compared to the more slender member (point *e* to *f*).

Similar behavior can be observed in thin-walled members subjected to cyclic loading. Buckling deformations appear as compressive stresses are applied and inelastic strains accumulate around the buckled cross-section. When the loading direction reverses, more inelastic strains accumulate at the buckled cross-sections which translate into strength and stiffness reduction in the subsequent cycles as shown in Fig. 2.3. The amount of inelastic strains

that accumulate, or more precisely the damage accumulated along the member length, translates into hysteretic energy dissipated.

The hysteretic energy dissipated can be equated to the work done by the applied loads/moments using the concept of energy balance in a structural member [27]. The energy input by external loading in a member (see, Fig. 2.1) can be equated to the sum of the kinetic energy $E_{kinetic}$, energy dissipated by additional damping or friction $E_{damping}$, and the energy dissipated by deformation of the components E_{deform}, as shown in Eq. 2.1. If additional damping is not provided and friction is neglected the corresponding term $E_{damping}$ can be dropped from Eq. 2.1. Since in the research discussed herein members are loaded in a quasi-static manner, the kinetic energy term $E_{kinetic}$ is also neglected. The remaining energy term E_{deform} can be separated in two components, the recoverable elastic strain energy E_{strain} and the hysteretic energy dissipated $E_{hysteretic}$. The input energy is equal to the work done by the external loads/moments applied to the structure (W_{ext}), which is calculated as the area enclosed by the load-deformation response, see Fig. 2.1. The hysteretic energy dissipated is approximated by equating it to the input energy, and thus it becomes the area enclosed by the load-deformation response. This approach is adopted throughout this dissertation to calculate the energy dissipated within a CFS member during cyclic loading.

$$E_{input} = E_{kinetic} + E_{damping} + E_{deform} \qquad 2.1$$

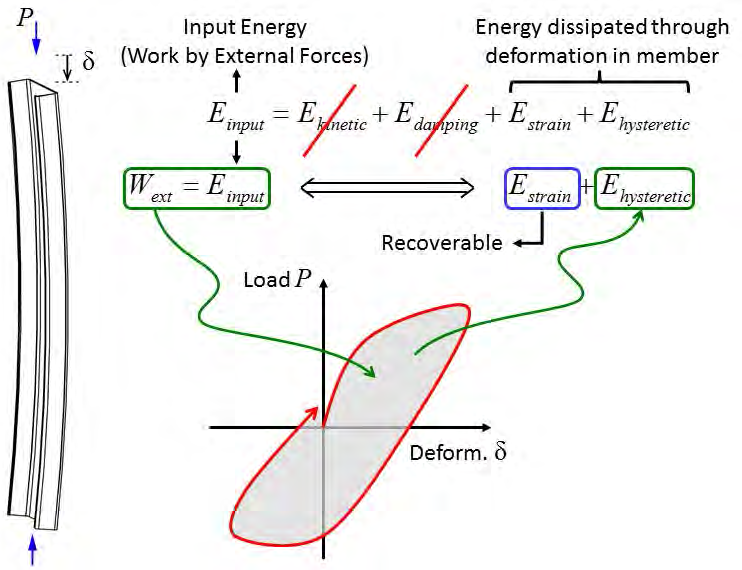

Fig. 2.1. Energy dissipated within the member is equated to the work done by external loads.

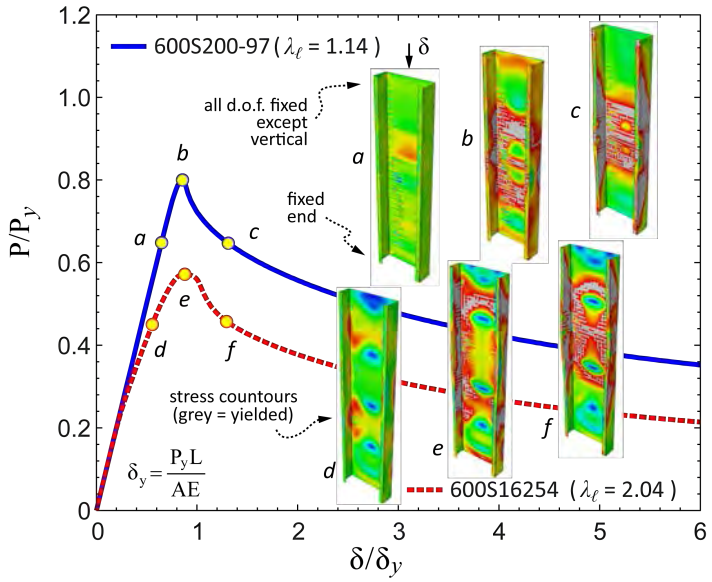

Fig. 2.2. Monotonic axial load-deformation (P-δ) response where the more slender member experiences larger buckling deformations which translate in smaller pre-peak stiffness (segment a-b vs. segment d-e) and peak strength.

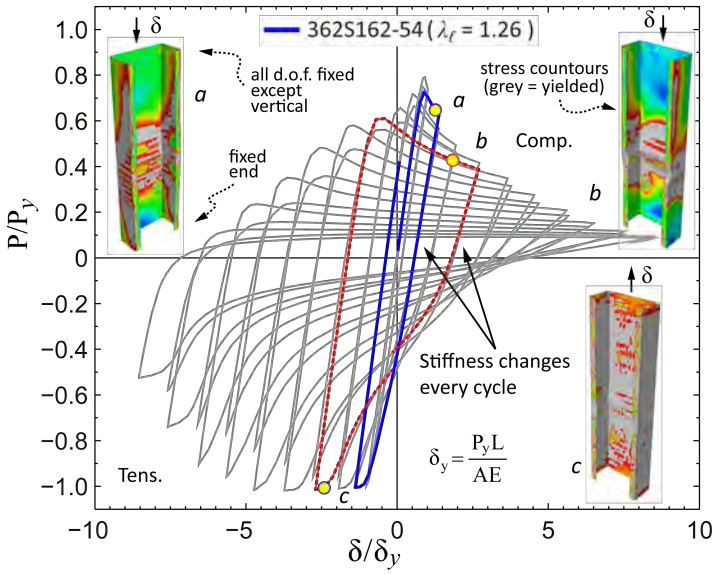

Fig. 2.3. Cyclic load deformation response. Inelasticity accumulates around the mid-span due to buckling deformations and yielding in tension.

The amount of energy dissipation can vary depending on the elastic buckling properties of the thin-walled members but also on the boundary conditions at the end of the members. The following two sections describe an analytical study of the cyclic behavior of thin steel plates subjected to stresses from axial and flexural loading. The study explores initial answers to the questions formulated at the beginning of this chapter and provided insight into how energy

dissipates and how damage accumulates in CFS cross-section elements (e.g., webs and stiffened elements) during cyclic loading.

2.1 Cyclic behavior and energy dissipation in thin steel plates

Cyclic behavior and energy dissipation in thin steel plates subjected to in-plane axial and flexural loading was studied through finite element analyses in ABAQUS [23]. The models are implemented using S9R5 thin shell elements for two sets of plates summarized in Table 2.1. The S9R5 shell element is a nine node, doubly-curved, reduced integration, quadratic element with five degrees of freedom per node, flexible shear strain definition, and numerically imposed Kirchhoff constraints (classical plate theory with no transverse shear deformation) [23]. Two widths (h) to thickness (t) ratios were selected with values matching the flat web width and thickness of common CFS channels. Plate lengths were selected as multiples of the buckled half-wavelength L_{cr}.

Two boundary condition cases for the loaded edges are considered to simulate pinned and fixed end conditions as shown in Fig. 2.4. In the pinned end condition, the translational degrees of freedom at the loaded edges are constrained to move as a rigid body while rotations at each node are unconstrained. For the fixed end condition, all degrees of freedom at the loaded edges are constrained to move as a rigid body. The out of plane displacement (*2 direction*) around all edges is restrained while free to move in the 1 and 3 directions, and free to rotate about direction 3. Initial geometric imperfections are imposed based on the lowest elastic buckling mode (see Fig. 2.6a and 2.6c) with magnitudes d_0/t=0.17 and d_0/t=0.54 (d_0=imperfection magnitude). These magnitudes respectively correspond to occurrence probabilities $P(d<d_0)$=0.25 and $P(d<d_0)$=0.75 that the actual imperfection, d, will be less than d_0 [28,29]. The geometry and boundary conditions are summarized in Fig. 2.4.

The elastic modulus of elasticity was assumed as E=203.4GPa and Poisson's ratio ν=0.3. Material nonlinearity was implemented using two true stress-strain (σ-ε) curves (Fig. 2.5) and isotropic hardening behavior. The stress-strain curves correspond to actual measured stress-strain curves from cold-formed steel tension coupon tests of the selected thicknesses. The plates are loaded from both ends by imposing a displacement or rotation history using the cyclic loading protocol for cold-formed steel members described in Appendix A. The protocol is symmetric with steps of increasing amplitude and two cycles per step. Each step's amplitude is 40% larger

than the previous (i.e., δ_i=1.4δ_{i-1} and θ_i=1.4 θ_{i-1}). The protocol is anchored at the fourth step to the elastic displacement δ_e=(0.673)^2$P_{cr}L/AE$ for uniform axial loading where P_{cr} is the elastic plate buckling load and A=th the plate cross section area (see Table 2.1). For the in-plane bending case (i.e., stress gradient) the protocol is anchored at the fourth step to the elastic rotation θ_e=(0.673)^2$M_{cr}L/2EI$ where M_{cr} is the elastic plate buckling moment and I= $ht^3/12$, is the plate cross-section moment of inertia. Energy dissipated, equated herein to external work done by the axial force in the direction of the applied displacement/rotation (or strain energy), will be compared between models for every cycle, and total length, half-wave length, plate slenderness effects will be discussed.

Table 2.1. Cold-formed steel thin plate analysis matrix.

Model[(a)]	t (mm)	h (mm)	L_{cr} (mm)	L	F_y (MPa)	P_{cr}[(b)] (kN)	M_{cr}[(b)] (kN-mm)
P60-33-i##-A	0.879	147	147	1, 2, 3, ... 10 times L_{cr},	334	3.24	-
P36-54-i##-A	1.367	85	85	305 and 2740mm	398	20.95	-
P120-97-i##-F	2.583	292	168	1, 2, 3, ... 10 times L_{cr},	422	-	13005
P100-33-i##-F	0.879	248	188	1625 and 3048mm	410	-	514

(a) i## = imperfection magnitude (i25:d_0=*0.17t;* i75: d_0=*0.54t*) [28], A = Axial, F = Flexural.
(b) Plate buckling load/moment

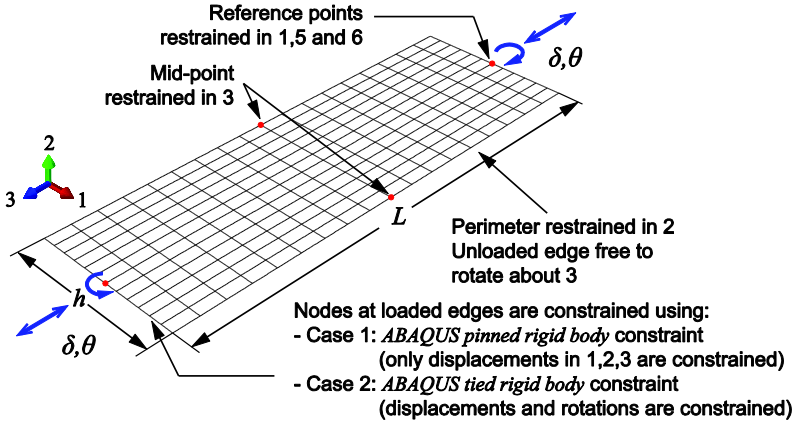

Fig. 2.4. Plate model geometry and boundary conditions.

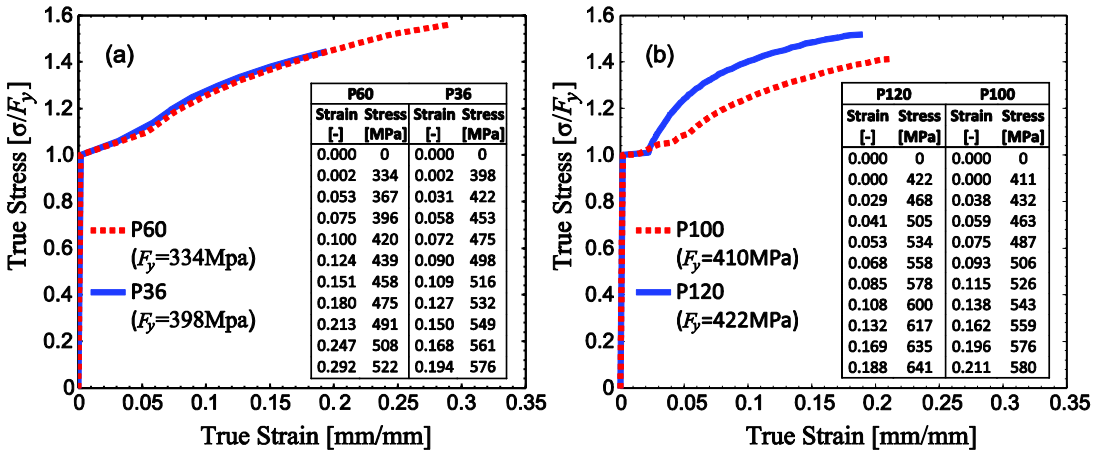

P60		P36	
Strain [-]	Stress [MPa]	Strain [-]	Stress [MPa]
0.000	0	0.000	0
0.002	334	0.002	398
0.053	367	0.031	422
0.075	396	0.058	453
0.100	420	0.072	475
0.124	439	0.090	498
0.151	458	0.109	516
0.180	475	0.127	532
0.213	491	0.150	549
0.247	508	0.168	561
0.292	522	0.194	576

P120		P100	
Strain [-]	Stress [MPa]	Strain [-]	Stress [MPa]
0.000	0	0.000	0
0.000	422	0.000	411
0.029	468	0.038	432
0.041	505	0.059	463
0.053	534	0.075	487
0.068	558	0.093	506
0.085	578	0.115	526
0.108	600	0.138	543
0.132	617	0.162	559
0.169	635	0.196	576
0.188	641	0.211	580

Fig. 2.5. True stress-strain curves assumed for plate models (a) in compression; and (b) in bending.

2.1.1 Cyclic axial behavior in thin plates

The axial cyclic responses obtained show elastic behavior for all cycles before reaching the peak compression load. At the peak compression load, energy dissipation starts as plastic strains concentrate at one or more locations leading to full cross-section and plate collapse (i.e., no load carrying capacity either in compression or tension). Damage accumulated in these zones that are approximately one half-wave (L_{cr}) long for all the plates analyzed irrespective of the plate length and generally happened at the mid-length (see, Fig. 2.6b). Only in four plates, corresponding to the longer plates with ratio h/t=62.12, fixed ends (case 2 in Fig. 2.4), and symmetric imposed imperfection patterns, the damaged zones happened closer to the loaded ends as shown in Fig. 2.6d. Energy dissipation occurs through plastic deformation at the damaged zones.

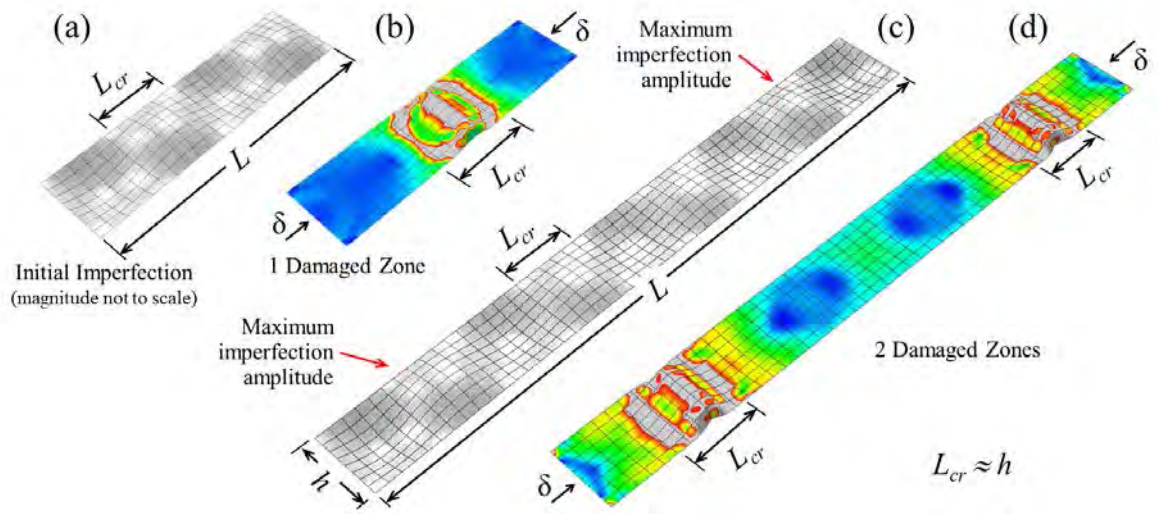

Fig. 2.6. Initial imperfection shape and damaged zone relationship in plates subjected to cyclic axial load.

Cumulative energy dissipation is compared in Fig. 2.7 for all lengths and for the two imperfection magnitudes considered. The energy dissipated was normalized to $P_y\delta_{cr}$ ($P_y=AF_y$, $\delta_{cr}=P_yL_{cr}/AE$, $A=th$) and plotted as a function of the cumulative post-peak applied displacement divided by the half-wave length $\Sigma(\delta/L_{cr})$. It can be seen that all the curves are grouped and therefore energy dissipation is independent of the plate length and is confined to a damaged zone that extends approximately one half-wave length L_{cr}. In the four long plates (L=849mm and 2743mm) that exhibited two damaged zones close to the loaded edges as shown in Fig. 2.6d, the amount of energy dissipation was about twice as much the plates that exhibited only one damaged zone (see Fig. 2.7b). Thus, the amount of energy dissipated is proportional to the number of damaged zones developed in the plate (i.e., zones with concentration of plastic strains). The presence of two damaged zones is related to the initial geometric imperfection field imposed to the plates. The imperfection field imposed to the long plates (i.e., lowest buckling mode) presents maximum amplitudes towards the loaded edges encouraging larger strains at that locations. The magnitude of the imperfection (i.e., d_0/t=0.17 and d_0/t=0.54) has no effect on the amount of energy dissipated or location of the damage zone. The effect from the different boundary conditions is almost negligible for both plate groups because damaged accumulated at least one half-wave length away from the loaded edges.

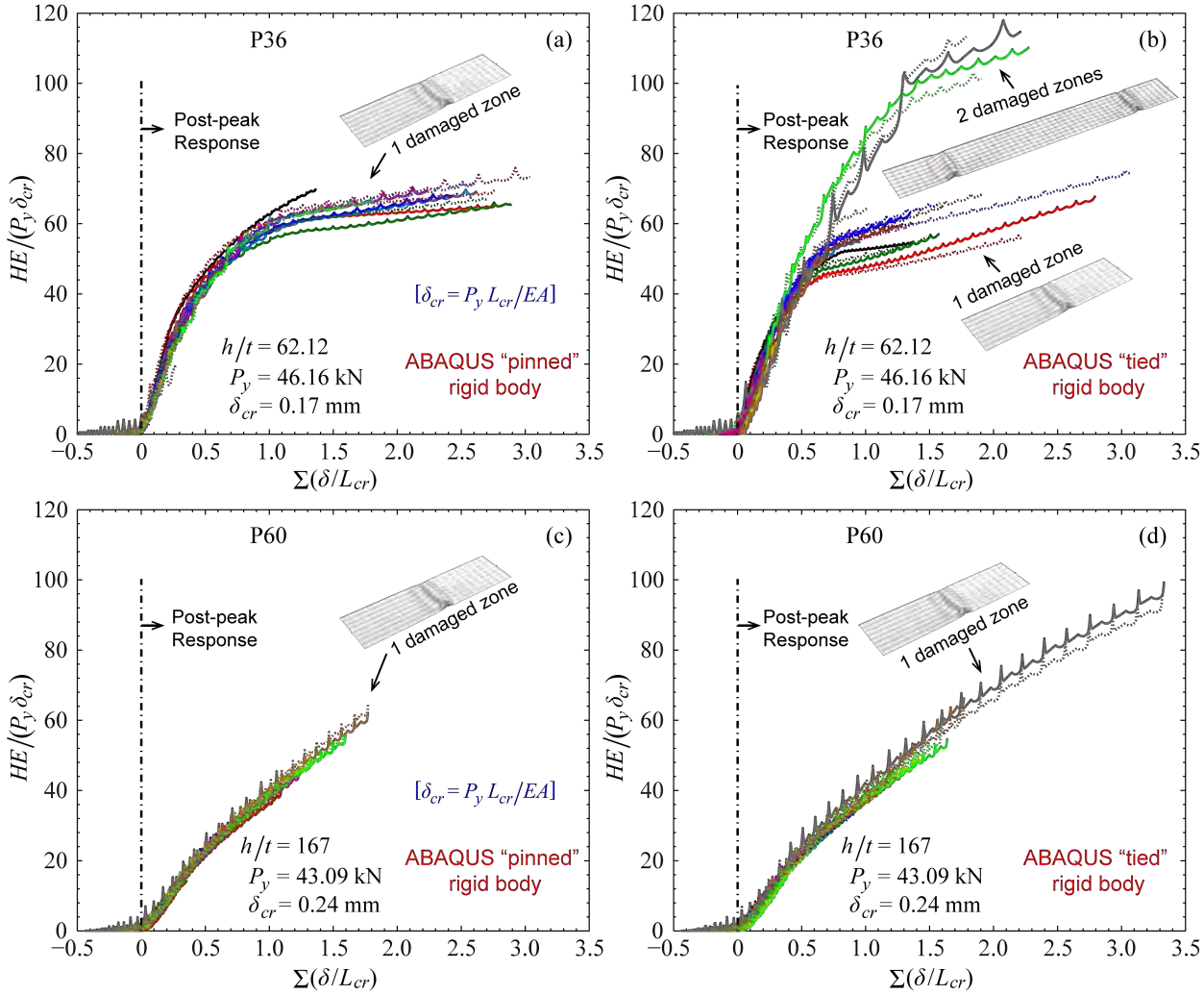

Fig. 2.7. Cumulative hysteretic energy (*HE*) dissipated in cyclic axially loaded thin plates of various lengths: (a) width *h*=85mm pinned ends; (b) width *h*=85mm tied ends; (c) width *h*=147mm pinned ends; (d) width *h*=147mm tied ends (see Table 2.1).

2.1.2 Cyclic flexural behavior in thin plates

The flexural responses obtained were mostly elastic in all cycles before reaching the peak moment. After peak moment, buckling inelastic deformations appear due to compressive stresses and energy dissipates as plastic strains extend at more than one location along the plates. Inelastic strains appear first on the side of the plate that is in compression right after peak moment and when the load direction reverses, inelastic strains may appear right at the opposite side (Fig. 2.8b) or at some other location due to redistribution of stresses (Fig. 2.8e). Damage accumulates in these zones that can extend a length less or equal to the buckled half-wavelength (L_{cr}) irrespective of the plate length. All plates in series P100 showed two damaged zones (Fig.

2.8c) while plates in series P120 showed one (Fig. 2.8b), two (Fig. 2.8c) and three damage zones (Fig. 2.8e) as the length of the plate increased as shown in Fig. 2.9. Energy dissipation occurs through plastic deformation at the damaged zones.

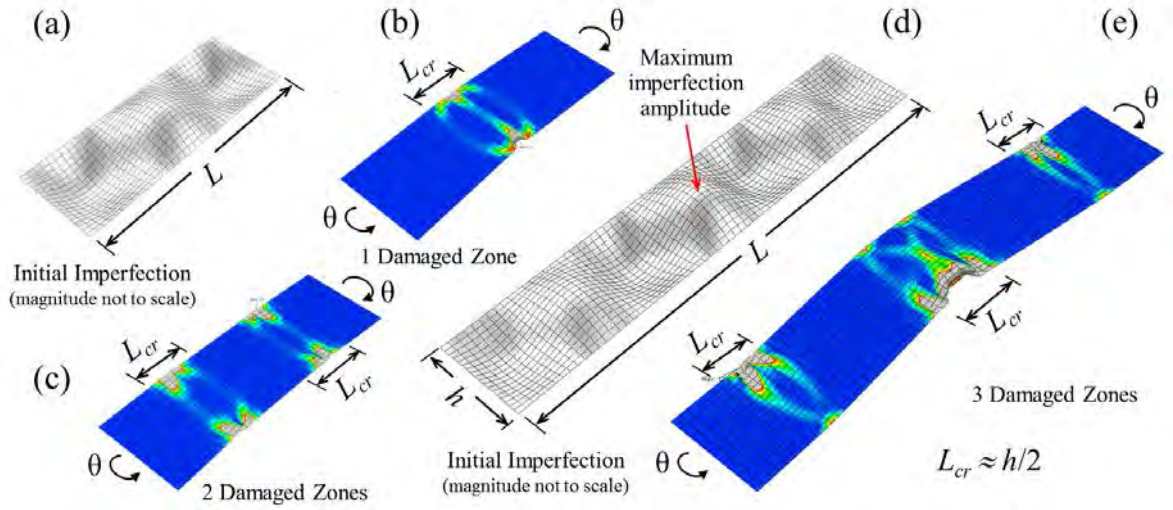

Fig. 2.8. Initial imperfection shape and damaged zone relationship in plates subjected to cyclic flexure.

Cumulative energy dissipation is compared in Fig. 2.9 for all lengths and for the two imperfection magnitudes considered. The energy dissipated was normalized to $M_y\theta_{ycr}$ ($M_y=SF_y$, $\theta_{ycr}=M_yL_{cr}/2EI$, $I=th^3/12$, $S=2I/h$) and plotted as a function of the cumulative post-peak applied rotation divided by the rotation θ_{ycr} $\Sigma(\theta/\theta_{ycr})$. The rotation θ_{ycr} at the end of a plate of length L_{cr} due to a moment M_y. In Fig. 2.9a is shown that all the curves in series P100 are grouped together and that the number of damaged zones (two) is the same for all the plates. Thus, energy dissipation is independent of the plate length and is confined to the two damaged zones that extend each approximately a half-wave length L_{cr}. As the number of damaged zones increases due to stress redistribution, more sections of the plate accumulate inelastic strains and thus the amount of energy dissipated increases. The cumulative energy dissipated is proportional to the number of damaged zones where plates exhibiting two damaged zones dissipated about twice the energy of those in which only one damaged zone occurred.

There is not an observed relationship as to what triggers the formation of more than one damaged zone on the analyzed plates. The plates are subjected to uniform bending right before peak moment, and theoretically maximum compressive stresses are the same along the farthest fiber. Thus, the likelihood that a damaged zone appears is the same for any cross-section along the plate and it only increases if the magnitude of the imperfection at such cross-section is bigger

than in adjacent cross-sections. Once inelasticity starts accumulating at one of the damaged zones other damaged zones are less likely to appear on the same side (see Fig. 2.8e) unless plastic strains have spread across the cross-section full depth. The magnitude of the imperfection (i.e., d_0/t=0.17 and d_0/t=0.54) had no effect on the amount of energy dissipated or location of the damage zone.

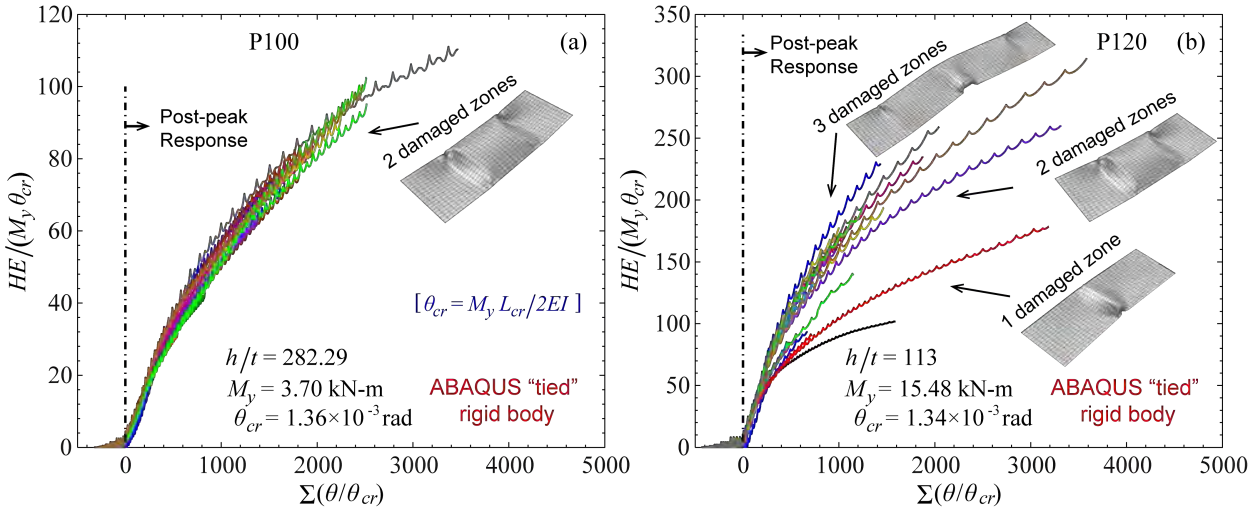

Fig. 2.9. Cumulative hysteretic energy (*HE*) dissipated in thin plates of various lengths subjected to cyclic bending load: (a) width *h*=248mm tied ends; (b) width *h*=292mm tied ends (see Table 2.1).

2.2 Remarks on the cyclic behavior of thin steel plates and cold-formed steel members

The previous sections showed that energy dissipation is independent of the plate length and that it occurs through accumulation of plastic deformations at localized damaged zones. Also they showed that damaged zones are confined to areas of approximately one half-wave long and that multiple damaged zones may occur either because of the initial imperfection's shape or stress redistribution (e.g., case of flexural stresses). These results provide insights into the cyclic behavior and energy dissipation in thin-walled cross-section elements, such as webs and stiffened elements. For example, the behavior illustrated in Fig. 2.8e is similar to the behavior exhibited by the top flange of the cold-formed steel member experiencing lateral-torsional buckling in Fig. 1.2d. Likewise, the web buckling deformations in Fig. 1.2d can be compared to the behavior shown in Fig. 2.8b. The next chapter introduces a framework for modeling cyclic behavior and energy dissipation including thin-walled behavior in CFS framing members.

Chapter 3: Nonlinear Beam-Column Models for Cold-Formed Steel Members

This chapter presents the development of a modeling approach for cold-formed steel axial and flexural members under cyclic loading including local, distortional and global buckling. Two approaches to model the response are introduced, a *nonlinear spring* model with concentrated nonlinear P-δ (Fig. 3.1b) or M-θ (Fig. 3.4b) behavior, and a *nonlinear beam-column* with distributed nonlinearity using load-strain P-ε (Fig. 3.1c) or moment-curvature M-κ (Fig. 3.4c) to model cross-section behavior. The underlying hysteretic model for members behavior consist of, a *backbone curve*, *unloading-reloading paths* that account for pinching, and a *damage model* for strength and stiffness degradation. This formulation is based on the hysteretic model *Pinching4* [21] as implemented in OpenSees [24].

3.1 Axial hysteretic modeling of CFS members

In this section, the results from calibration of axial responses from tested CFS members described in [54] are used to formulate the nonlinear *spring* and *beam-column* models depicted in Fig. 3.1. The two models are formulated to simulate the cyclic response of CFS axial members spanning between two nodes as in the case of frame elements in common analysis tools. Parameters for the underlying hysteretic model for local, distortional and global buckling axial members are summarized in Table 3.1 and 3.2, [54].

3.1.1 Spring model - concentrated nonlinearity

The spring modeling approach uses axially rigid beam elements connected to a P-δ *nonlinear spring* where all the nonlinear behavior concentrates. The spring is located at one end of the modeled member. Fig. 3.1b illustrates this concept where the CFS axial member subjected to uniform axial force in Fig. 3.1a is modeled using a *nonlinear spring* at the top end. Parameters defining the nonlinear spring behavior are obtained by direct calibration of *Pinching4* to match experimental load-deformation responses and energy dissipation as described in [54]. Using nonlinear springs is a computationally inexpensive approach but requires adjusting the calibrated model parameters depending on possible different member lengths and loading conditions. For example, a member subjected to non-uniform axial load can be modeled using multiple springs

along the length where the backbone displacement coordinates are scaled accordingly to the distance between springs.

3.1.2 Nonlinear beam-column model – distributed nonlinearity

In this modeling approach, a *nonlinear beam-column element* with distributed nonlinearity is formulated using a load-deflection *P-ε* formulation to model the cross-section behavior (Fig. 3.1c). This approach allows modeling of damage spreading due to buckling deformations along the member length as observed in [77], and lets modeling different axial loading conditions using the same set of parameters that define the cross-section behavior. The parameters to define the load-strain behavior of the cross-section can be derived from the values obtained for the nonlinear spring model. The applied displacement δ_i from Table 3.1 is converted to axial strain ε_i by dividing by the member length, thus $\varepsilon_i = \delta_i / L$. This defines the axial load-strain backbone *P-ε* at any cross section of the CFS axial member assuming a uniform strain distribution along the member. Thus, as described, this approach assumes that damaged and inelastic strains are averaged along the member length. This assumption does not directly reflect the results observed in Chapter 2 and [77] where inelastic strains concentrate in localized damaged zones; however, energy dissipation and the load-deflection response *P-δ* are still captured as illustrated in the next subsection. Parameters to model strength and stiffness degradation are defined in Table 3.2 and do not differ from those of the nonlinear spring model.

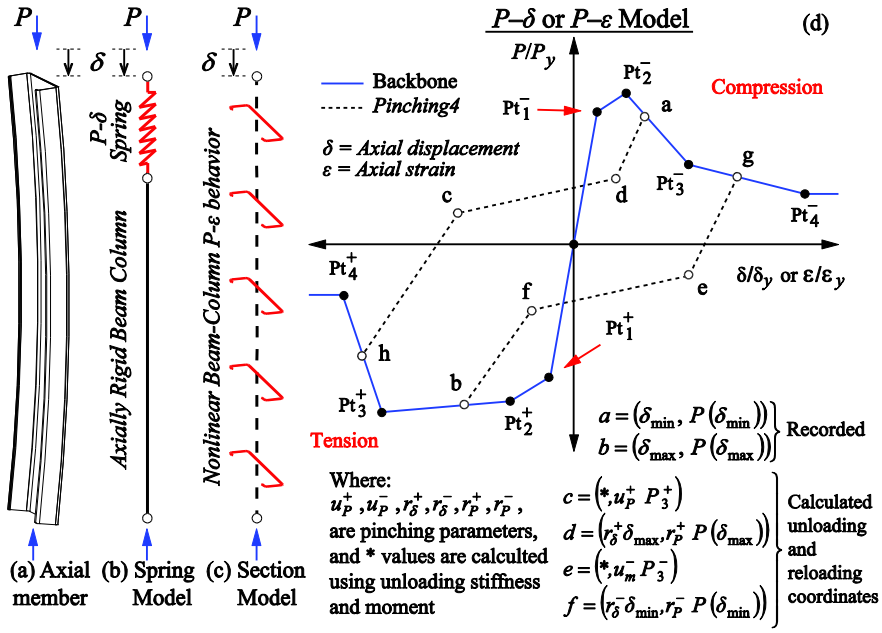

Fig. 3.1. a) Axial member; b) spring model; c) nonlinear beam-column model; d) hysteretic model.

3.1.3 Simulating CFS members axial cyclic response

This section illustrates the application of the hysteretic model to simulate the axial response of CFS members. The two models, *nonlinear springs* and the *nonlinear beam-column* element with distributed nonlinearity illustrated in Fig. 3.1 are used to simulate the experimental response of the axial members described in [77]. The *nonlinear spring* model is implemented in OpenSees using an axially rigid beam element connected to a *zeroLength* element located at the loading point (see Fig. 3.2b). For these models, one spring will suffice and values from Table 3.1 and 3.2 are used directly without further adjustment that would be required for example if additional springs were to be placed along the member length *L*. The *nonlinear beam-column* model is implemented in OpenSees using a *dispBeamColumn* element connected between the two end nodes (see Fig. 3.2b). The Gauss-Lobatto quadrature rule with seventh integration points, two at the element ends, is used for numerical integration within the element. Axial load-strain section behavior is implemented using values in Table 3.1 and 3.2.

Comparison between the two models shows that they both produce similar results as far as modeling the load-deformation cyclic response P-δ of the tests in [77] as illustrated in Fig. 3.2a. Moreover the root mean-squared deviation between the predicted load responses to the tests is between 8% and 14% as shown in Fig. 3.3a. Likewise, both methods show very similar energy dissipation cycle by cycle (Fig. 3.2c) and the total energy dissipated is almost identical yet smaller than the tests (Fig. 3.3b). One main disadvantage of using spring models attached to axially rigid beam elements arises when modeling elements in which non-uniform axial loads may arise, like the case of a shear wall chord-stud where the fasteners may subject the member to a non-uniform axial loads. In such cases proper scaling, as previously described, of the backbone displacement coordinates is required to avoid any displacement incompatibilities. Adjusting the backbone to accommodate other than uniform axial loads using hysteretic springs can be troublesome, however this inconvenience can be avoided by using the distributed nonlinearity approach. Using a beam-column element with distributed nonlinearity P-ε does not require adjusting the backbone curve displacements to accommodate non-uniform axial loads or other combined loading cases (axial +moment).

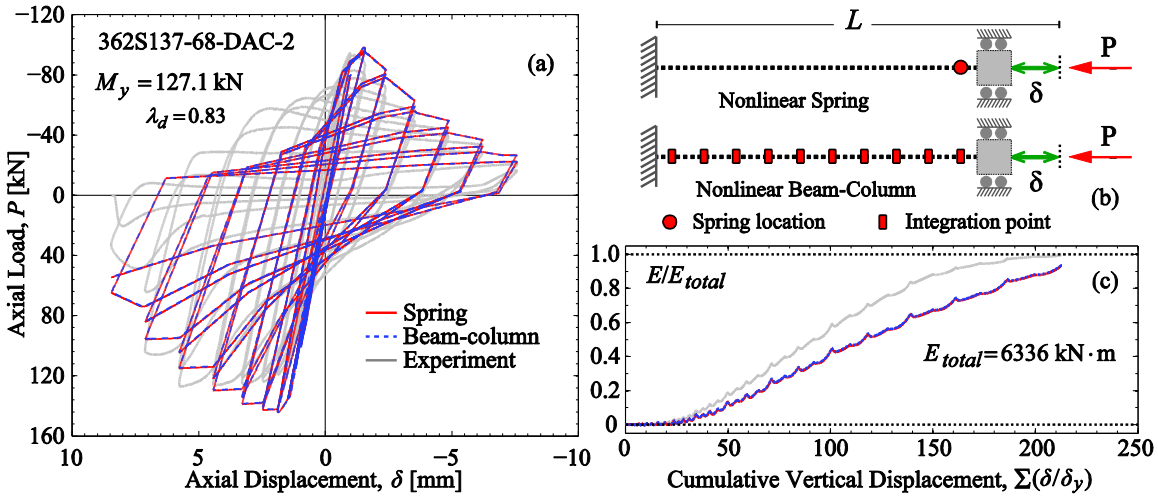

Fig. 3.2. a) Simulated and experimental response; b) Spring and beam-column models; c) Energy dissipated.

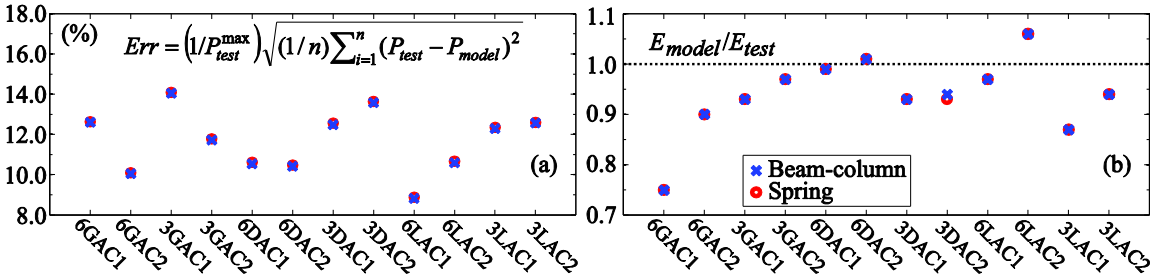

Fig. 3.3. Model to tests load a) and energy b) dissipation ratio for all test in [77] (see member labels in Table 3.1).

Table 3.1. Backbone definition points for axial specimens.

	Specimen	P_v (kN)	k_e [(a)] (kN/mm)	δ_v [(b)] (mm)	δ_1/δ_v	δ_2/δ_v	δ_3/δ_v	δ_4/δ_v	P_1/P_v	P_2/P_v	P_3/P_v	P_4/P_v	k_1/k_e	k_2/k_e ×10^{-3}	k_3/k_e ×10^{-3}	k_4/k_e ×10^{-3}
1	600S137-97-GAM-1	245	56.13	4.36	0.463	0.562	1.394	5.600	0.433	0.482	0.210	0.096	935	490	-326	-27
2	600S137-97-GAM-2	249	56.23	4.42	0.452	0.664	1.815	5.600	0.373	0.414	0.205	0.107	826	195	-182	-26
3	362S137-68-GAM-1	123	28.04	4.40	0.440	0.618	1.642	5.600	0.414	0.460	0.233	0.124	942	258	-222	-28
4	362S137-68-GAM-2	122	28.08	4.35	0.419	0.535	1.528	5.600	0.391	0.435	0.181	0.083	933	374	-256	-24
5	600S137-68-DAM-1	177	138.86	1.28	0.837	1.427	3.779	6.000	0.493	0.548	0.377	0.286	589	93	-72	-41
6	600S137-68-DAM-2	177	138.36	1.28	0.758	1.278	3.438	6.000	0.495	0.549	0.379	0.284	652	106	-79	-37
7	362S137-68-DAM-1	124	106.13	1.17	1.144	1.523	3.045	6.000	0.735	0.816	0.556	0.417	642	215	-171	-47
8	362S137-68-DAM-2	123	105.68	1.17	0.935	1.293	3.100	6.000	0.724	0.804	0.549	0.411	774	225	-141	-48
9	600S162-33-LAM-1	72	143.49	0.50	0.526	0.816	2.913	6.000	0.385	0.427	0.259	0.188	731	147	-80	-23
10	600S162-33-LAM-2	72	143.56	0.50	0.608	1.110	2.234	6.000	0.416	0.462	0.298	0.203	684	92	-146	-25
11	362S162-54-LAM-1	113	181.80	0.62	1.017	1.309	2.877	6.000	0.699	0.777	0.478	0.333	688	266	-190	-47
12	362S162-54-LAM-2	113	181.92	0.62	1.108	1.434	2.791	6.000	0.681	0.756	0.489	0.331	614	232	-197	-49
	Tension															
14	362S162-54-LAMT-1	113	181.46	0.62	0.976	1.669	7.232	-	0.823	0.953	0.967	-	847	213	3	-
15	362S162-54-LAMT-2	114	182.79	0.62	1.126	2.880	16.168	25.633	0.870	0.957	0.997	0.450	779	102	3	-58
16	**Tension Adjusted**	**114**	**182.79**	**0.62**	**1.128**	**1.488**	**6.000**	**8.000**	**1.044**	**1.134**	**1.172**	**0.872**	**926**	**250**	**9**	**-150**

(a) $k_e = A_a E/L$ (E=203.4GPa); (b) $\delta_v = P_v/k_e$

Table 3.2. *Pinching4* model parameters for axial specimens.

Specimen[a]	Damage Parameters						Pinching Parameters						
	Strength [b]		Stiffness [b]				Compression			Tension			Backbone
	β_2	β_4	β_2	β_4	γ_E	E_M[c]	r_{D-}	r_{F-}	u_{F-}	r_{D+}	r_{F+}	u_{F+}	Used [d]
600S137-97-GAC-1	0.70	0.98	0.69	0.20	1.88	8541	0.40	0.92	0.50	0.55	0.25	-0.10	1, 16
600S137-97-GAC-2	0.58	0.60	0.73	0.22	2.62	8761	0.40	0.92	0.50	0.75	0.25	-0.10	1, 16
362S137-68-GAC-1	0.69	0.71	0.90	0.33	3.39	4417	0.40	0.92	0.50	0.35	0.25	-0.03	4, 16
362S137-68-GAC-2	0.66	0.70	0.70	0.22	2.25	4450	0.48	0.92	0.50	0.50	0.25	-0.03	4, 16
600S137-68-DAC-1	0.71	1.04	0.68	0.30	4.78	1868	0.66	0.92	0.50	0.80	0.30	-0.10	6, 16
600S137-68-DAC-2	0.68	0.82	0.72	0.27	4.86	1863	0.66	0.92	0.50	0.80	0.26	-0.10	6, 16
362S137-68-DAC-1	0.68	1.04	0.70	0.52	5.05	1260	0.65	0.92	0.50	0.45	0.62	-0.03	8, 16
362S137-68-DAC-2	0.67	1.09	0.67	0.40	4.95	1270	0.60	0.92	0.50	0.53	0.62	-0.03	8, 16
600S162-33-LAC-1	0.71	0.55	0.68	0.33	8.68	294	0.48	0.92	0.50	0.80	0.30	-0.10	10, 16
600S162-33-LAC-2	0.78	0.73	0.73	0.33	8.47	293	0.48	0.92	0.50	0.80	0.30	-0.10	10, 16
362S162-54-LAC-1	0.55	0.49	0.66	0.43	6.63	579	0.48	0.92	0.50	0.53	0.62	-0.03	11, 16
362S162-54-LAC-2	0.56	0.46	0.62	0.32	6.49	581	0.49	0.92	0.50	0.53	0.62	-0.03	11, 16

(a) SSMA profiles [46]; AC= axial cyclic test; G, D and L are = Global, Distortional, and Local buckling [22].
(b) Fit using positive and negative excursions; (c) Energy in units of kN-mm; (d) Backbone curve from Table 3.1

Table 3.3. Statistics for *Pinching4* parameters.

	Damage Parameters						Pinching Parameters					
	Strength		Stiffness				Compression			Tension		
	β_2	β_4	β_2	β_4	γ_E	E_M	r_{D-}	r_{F-}	u_{F-}	r_{D+}	r_{F+}	u_{F+}
μ	0.66	0.77	0.71	0.32	5.00	2848	0.52	0.92	0.50	0.62	0.39	-0.07
cov	0.10	0.29	0.09	0.29	0.45	1.07	0.20	0.00	0.00	0.26	0.45	-0.56

μ = mean value; cov = coefficient of variation.

3.2 Flexural hysteretic modeling of CFS members [1]

In this section, the results from calibration of flexural response from tested CFS members described in [54] are used to formulate the nonlinear *spring* and *beam-column* models depicted in Fig. 3.4. The two models are formulated to simulate the cyclic response of CFS flexural members spanning between two nodes as in the case of frame elements in common analysis tools. Parameters for the underlying hysteretic model for local, distortional and global buckling axial members are summarized in Table 3.4 to 3.5, [54].

3.2.1 Spring model - concentrated nonlinearity

The spring modeling approach uses rigid beam elements connected to *M-θ nonlinear springs* where all the nonlinear behavior concentrates. Springs are located at preselected locations along the modeled member length and their number and distribution would depend on the loading conditions. Fig. 3.4b illustrates this concept where the CFS member under constant moment in Fig. 3.4a is modeled using a *nonlinear spring* at the mid-span. Parameters defining the nonlinear spring behavior are obtained by direct calibration of *Pinching4* to match experimental moment rotation responses and energy dissipation as described in [54]. Using nonlinear springs is a computationally inexpensive approach but requires adjusting the hysteretic model parameters depending on possible different loading conditions.

3.2.2 Nonlinear beam-column model – distributed nonlinearity

In this modeling approach, a *nonlinear beam-column element* with distributed nonlinearity is formulated using a moment curvature *M-κ* formulation to model the cross-section behavior (Fig. 3.4c). This approach allows modeling damage spreading due to buckling deformations along the member length as observed in [54], and lets modeling different loading conditions using the same set of parameters that define the cross-section behavior. The parameters to define the moment-curvature behavior of the cross-section can be derived from the values obtained for the nonlinear spring model. Backbone rotations, $\theta_i=\delta_i/a$, from [54] are converted to backbone curvature values κ_i using Eqs. 3.1-3.2 (see Fig. 3.4c),

---

[1] This section is part of a paper presented at the *7th European Conference on Steel and Composites Structures* in Napoli, Italy 2014, with the title "**Cyclic Flexural Hysteretic Models for Cold-Formed Steel Seismic Simulation**".

$$\kappa_1 = \theta_1 \left(\frac{6}{3L_u + 2a} \right) \tag{3.1}$$

$$\kappa_i = \left(\frac{2}{L_u} \right) \left(\theta_i - \frac{aM_i}{3M_1 / \kappa_1} \right), \quad i = 2...4 \tag{3.2}$$

These expressions define the moment-curvature backbone M-κ at any cross section of the CFS flexural member. Parameters to model strength and stiffness degradation are defined in Table 3.5 and do not differ from those of the nonlinear spring model.

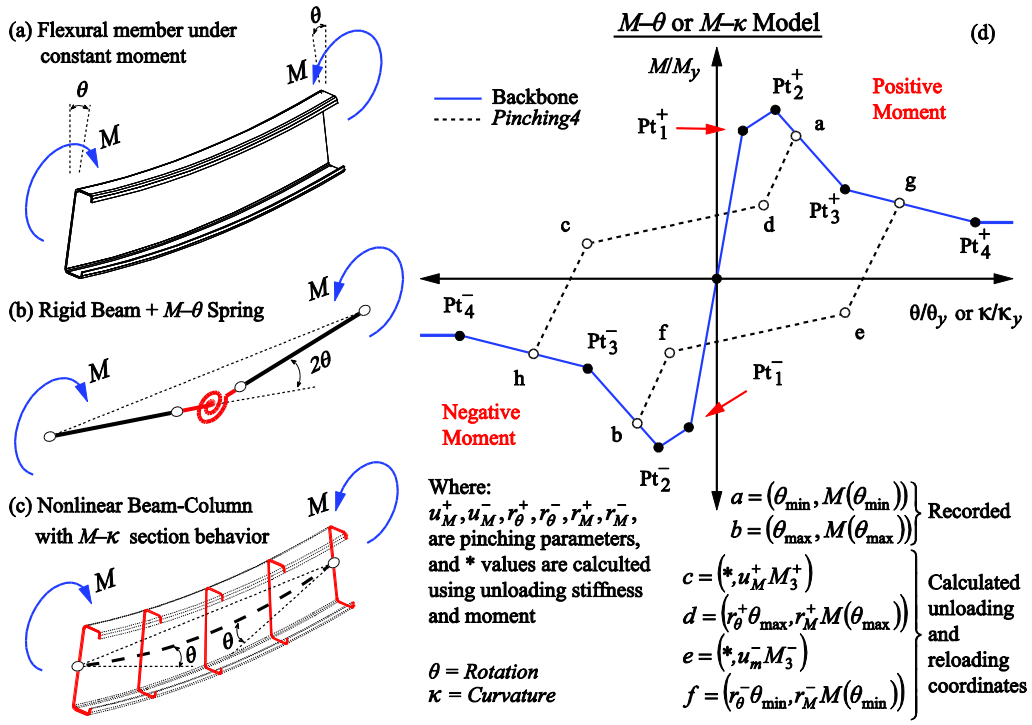

Fig. 3.4. a) Flexural member; b) spring model; c) nonlinear beam-column model; d) hysteretic model.

3.2.3 Simulating CFS members flexural cyclic response

This section illustrates the application of the hysteretic model to simulate the flexural response of CFS members. The two models, *nonlinear springs* and the *nonlinear beam-column* element with distributed nonlinearity illustrated in Fig. 3.4 are used to simulate the experimental response of the flexural members described in [54]. The *nonlinear spring* model is implemented in OpenSees using rigid beam elements connected to *zeroLength* elements located at the loading points (see Fig. 3.5b). For these models, two springs will suffice and values from Table 3.4 and 3.5 are used directly without further adjustment that would be required for example if additional springs were to be placed along the unbraced length L_u. The *nonlinear beam-column* model is implemented in OpenSees using *dispBeamColumn* elements, one for each shear span of length a,

and one for the unbraced length L_u (see Fig. 3.5b). The Gauss-Lobatto quadrature rule with seventh integration points, two at the element ends, is used for numerical integration within each element. Moment-curvature behavior is implemented using values in Table 3.4 and 3.5 and Eqs. (3.1-3.2).

Comparison between the two models shows that both produce similar results as far as modeling the load-deformation cyclic response P-δ of the tests in [54] as illustrated in Fig. 3.5a. Moreover the root mean-squared deviation between the predicted load responses to the tests is between 5% and 12% as shown in Fig. 3.6a. Likewise, both methods show very similar energy dissipation cycle by cycle (Fig. 3.5c) and the total energy dissipated is almost identical yet smaller than the tests (Fig. 3.6b). Evident differences on the deflections and rotations along the member arise from the nature of each model as illustrated in Fig. 3.5b for rotations and vertical deflections. Spring models with rigid bars have the disadvantage of displacement and rotations incompatibility depending on the spring arrangement and would require adjustments of spring definition parameters when modeling different type of loading. A solution commonly used in analysis of frames under lateral loads consists of using elastic-beam elements combined with springs that model the nonlinear behavior at the plastic hinge locations; however this approach requires to define a priori the springs location, could lead to numerical instability problems and makes it difficult to express stiffness degradation as a fraction of the elastic stiffness [78]. In this regard, using a beam-column element with distributed nonlinearity M-κ is an efficient approach that does not require additional adjustment of parameters in Table 3.4 and 3.5, and lends itself to further generalization and use with other loading configurations such as those producing moment gradients.

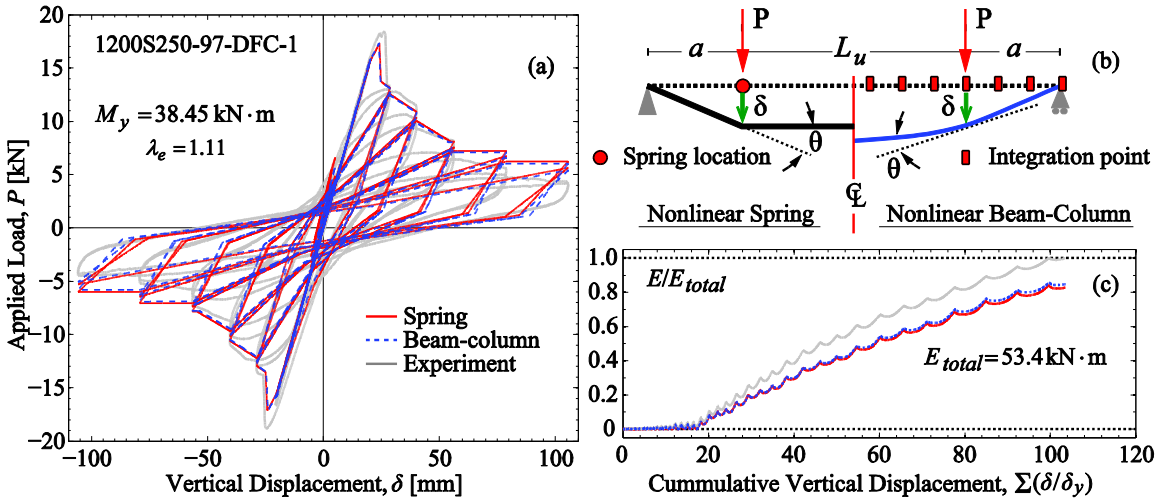

Fig. 3.5. a) Simulated and experimental response; b) Spring and beam-column models; c) Energy dissipated.

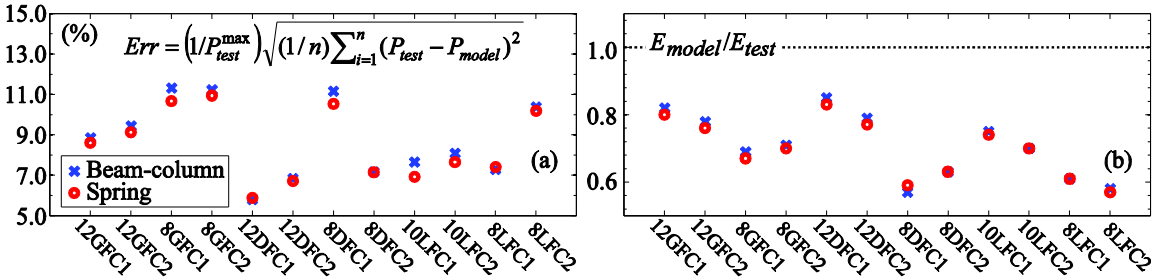

Fig. 3.6. Model to tests load a) and energy b) dissipation ratio for all test in [54] (see member labels in Table 3.4).

Table 3.4. Backbone definition points for flexural specimens.

	Specimen [a]	M_y (kN-mm)	k_e [b] (MN-mm/rad)	θ_y [c] (rad×10^{-3})	θ_1/θ_y	θ_2/θ_y	θ_3/θ_y	θ_4/θ_y	M_1/M_y	M_2/M_y	M_3/M_y	M_4/M_y
1	1200S162-97-GFM-1	32668	1193.1	27.38	0.328	0.443	0.631	2.000	0.314	0.349	0.237	0.193
2	1200S162-97-GFM-2	31850	1192.2	26.72	0.325	0.515	0.761	2.000	0.317	0.352	0.236	0.185
3	800S162-97-GFM-1	17711	429.6	41.22	0.332	0.495	0.625	1.880	0.326	0.363	0.258	0.252
4	800S162-97-GFM-2	18182	432.1	42.08	0.347	0.511	0.808	2.000	0.337	0.374	0.253	0.211
5	1200S250-97-DFM-1	36673	2073.8	17.68	0.725	0.879	0.905	2.000	0.656	0.729	0.577	0.387
6	1200S250-97-DFM-2	37977	2069.5	18.35	0.732	0.883	0.925	2.000	0.680	0.755	0.538	0.361
7	800S250-68-DFM-1	14007	546.1	25.65	0.881	1.018	1.089	2.000	0.830	0.923	0.571	0.408
8	800S250-68-DFM-2	14148	550.7	25.69	0.892	1.023	1.109	2.000	0.821	0.912	0.538	0.440
9	1000S200-43-LFM-1	11983	525.2	22.81	0.532	0.685	0.737	2.000	0.497	0.552	0.307	0.230
10	1000S200-43-LFM-2	12045	526.2	22.89	0.524	0.675	0.738	2.000	0.483	0.536	0.279	0.176
11	800S200-33-LFM-1	5575	243.8	22.87	0.550	0.698	0.752	2.000	0.526	0.585	0.283	0.193
12	800S200-33-LFM-2	5632	244.6	23.02	0.549	0.684	0.751	2.000	0.510	0.567	0.274	0.218

(a) SSMA profiles [46]; FM= flexural monotonic test; G, D and L are = Global, Distortional, and Local buckling [22].
(b) $k_e = 6EI/(3L_u+2a)$, E=203.4GPa, L=4876.8mm, a = 832mm for GFM, a = 1543mm for DFM and LFM
(c) $\theta_y = M_y/k_e$

Table 3.5. *Pinching4* model parameters for flexural specimens.

Specimen [a]	Damage Parameters						Pinching Parameters						Backbone Used [d]
	Strength [b]		Stiffness [b]				Positive Moment			Negative Moment			
	β_2	β_4	β_2	β_4	γ_E	E_M [c]	$r_{\theta-}$	r_{M-}	u_{M-}	$r_{\theta-}$	r_{M-}	u_{M-}	
1200S162-97-GFC-1	0.067	0.000	1.012	0.320	11.32	374.0	0.175	0.291	-0.176	0.205	0.324	-0.208	2
1200S162-97-GFC-2	0.250	0.347	1.113	0.382	6.51	381.3	0.226	0.334	-0.174	0.234	0.348	-0.208	2

800S162-97-GFC-1	0.237	0.318	1.184	0.459	7.71	360.2	0.218	0.333	-0.177	0.223	0.333	-0.190	4
800S162-97-GFC-2	0.304	0.806	1.077	0.394	8.51	372.3	0.207	0.324	-0.177	0.261	0.362	-0.211	4
1200S250-97-DFC-1	0.581	1.096	0.953	0.665	10.45	577.0	0.190	0.339	-0.203	0.196	0.382	-0.193	5
1200S250-97-DFC-2	0.510	0.694	1.041	0.722	10.83	562.4	0.104	0.265	-0.209	0.226	0.418	-0.168	5
800S250-68-DFC-1	0.398	0.000	0.491	0.735	7.16	353.7	0.224	0.359	-0.145	0.225	0.358	-0.195	7
800S250-68-DFC-2	0.519	0.572	0.916	1.613	5.74	351.1	0.149	0.288	-0.162	0.242	0.383	-0.193	7
1000S200-43-LFC-1	0.481	0.416	0.748	0.479	9.21	158.1	0.090	0.280	-0.188	0.213	0.411	-0.170	10
1000S200-43-LFC-2	0.486	0.736	0.351	0.307	17.86	141.1	0.074	0.213	-0.164	0.221	0.403	-0.178	9
800S200-33-LFC-1	0.703	0.495	0.584	0.406	11.95	69.8	0.107	0.302	-0.140	0.226	0.449	-0.185	11
800S200-33-LFC-2	0.212	0.000	0.349	0.018	14.68	69.9	0.108	0.286	-0.162	0.280	0.475	-0.114	11

(a) SSMA profiles [46]; FC= flexural cyclic test; G, D and L are = Global, Distortional, and Local buckling [22].
(b) Fit using positive and negative values; (c) Energy in units of kN-mm; (d) Backbone curve from Table 3.4.

Table 3.6. Statistics for *Pinching4* parameters.

	Damage Parameters						**Pinching Parameters**					
	Strength		**Stiffness**				**Compression**			**Tension**		
	β_2	β_4	β_2	β_4	γ_E	E_M	r_{D-}	r_{F-}	u_{F-}	r_{D+}	r_{F+}	u_{F+}
μ	0.40	0.46	0.82	0.54	10.16	314	0.16	0.30	-0.17	0.23	0.39	-0.18
cov	0.46	0.76	0.37	0.72	0.35	0.54	0.37	0.13	-0.12	0.10	0.12	-0.14

μ = mean value; cov = coefficient of variation.

3.3 Conclusions

The modeling approach described allows modeling CFS member cyclic behavior in systems and different loading scenarios as illustrated later in Chapter 6. Some shortcomings arise with the modeling approach using nonlinear beam-columns with hysteretic behavior modeled at the cross-section level as described in this chapter. The first one is related to the axial load-bending interaction in the case where both axial loads and bending moments are applied at member ends. This type of interaction is not included for the behavior at the cross-section level formulated here and would not be addressed in this dissertation. However, the approach remains relevant to model the behavior of several components that are subjected to mainly axial loads or bending moments in a light-framed steel building like the one shown in Fig. 1.1.

The second shortcoming is related to the underlying cross-section behavior model (*Pinching4*). For axial members, the modeled unloading-reloading behavior from tension to compression does not reflect the observed behavior from the experiments where the amount strength or stiffness degrades in compression excursions is independent from that in tension excursions. Because damage accumulation in *Pinching4* is defined using the same sets of parameters for both loading directions, damage accumulated during compression excursions is used to reduce the strength envelope for the subsequent excursions in tension (and vice versa). This results in underestimation or overestimation of the strength or stiffness degradation depending on the loading direction. In the next chapter these two issues are addressed by

modifying *Pinching4* to include damage accumulation independent of the loading directions and redefining the unloading-reloading path from tension to compression for axial members.

Chapter 4: Nonlinear Beam-Column Model for Thin-Walled Steel Columns Including Local Buckling [2]

Steel columns subjected to dynamic loading such as those resulting from earthquake, wind, and other hazards, can experience cyclic local buckling deformations. During cyclic loading, buckling deformations reverse and combine with yielding in tension at the highly stressed locations compromising the member's strength and stiffness and affect their ductility. Local buckling deformations develop under compression and stretch during tension, and are more pronounced, as well as their effects, in thinner cross-sections (e.g., thin-walled cold-formed steel).

The framework described in Chapter 6 for modeling the axial cyclic behavior in CFS members is generalized in this chapter for thin-walled steel columns including local buckling. The nonlinear-beam column approach previously described is combined with a hysteretic cross-section behavior model that describes the behavior observed in the experimental responses described in [77]. Generalized expressions for backbones, strength degradation, stiffness degradation and unloading-reloading parameters are presented as a function of the member cross-section slenderness λ_ℓ and the hysteretic energy dissipated. The model parameters are derived using *P-δ* responses obtained from finite element analysis of thin-walled cold-formed steel members conducted in ABAQUS [23]. Parameters are calibrated so that the model matched the simulated axial load-displacement (*P-δ*) monotonic and cyclic responses of each column in the finite element analysis set.

4.1 Simulated axial monotonic and cyclic responses database

Twenty two thin-walled C-shaped columns were modeled using ABAQUS [23] to study the monotonic and cyclic behavior of axial members exhibiting local buckling deformations. The cross-sections were selected from the SSMA catalog [46] such that the capacity in compression is governed by local buckling as predicted using the AISI-S100-07 Direct Strength Method [22]. The cross-sections properties and length were selected to cover a range of local cross-section

---

[2] Parts of this chapter are part of a paper accepted and presented at the *2015 SSRC Annual Stability Conference* with the title "**OpenSees Simulation of Steel Column Axial Cyclic Response Including Local Buckling**" [85].

slenderness $\lambda_\ell = (P_y/P_{cr\ell})^{0.5}$ from 0.69 to 3.39 ($P_y=AF_y$, A=cross-section area; F_y=yield stress and $P_{cr\ell}$=local buckling load calculated using for example CUFSM [48]). The analyses were setup to simulate similar boundary conditions and loading as those described in [77] for testing CFS axial members. Table 4.1 summarizes the selected cross-sections and their elastic buckling properties.

The column models are implemented using S9R5 thin-shell elements that allow double-curvature within one element, a feature that facilitates definition of initially curved geometries with smaller mesh size (as compared to using S4 or S4R elements). The length of each column was set such that at least five buckling half-waves could develop in compression. The half-wavelength $L_{cr\ell}$ was calculated using the finite strip eigen-buckling analysis software CUFSM [48]. The aspect ratio (length/width) for each element was about 4:1 with the long side aligned along the length of the column. End boundary conditions were modeled as fixed ends with one end allowed to move along the axial direction 3, see Fig. 4.1a. Loading was applied at the free end by imposing a displacement history derived using the displacement-controlled testing protocol for cold-formed steel members described in Appendix A.

Initial geometric imperfections are simulated using the 1D spectral approach described by Zeinoddini et al. [28]. In this approach the imperfection field imposed is formed using a linear combination of five buckling mode shapes where the amplitude of each mode along the length is given by a one-dimensional power spectrum. The 1D spectrum accounts for the frequency content and variability of the distribution of each mode along the length. The mode shapes used to generate the imperfection field where calculated using CUFSM [48] and are illustrated in Fig. 4.1b.

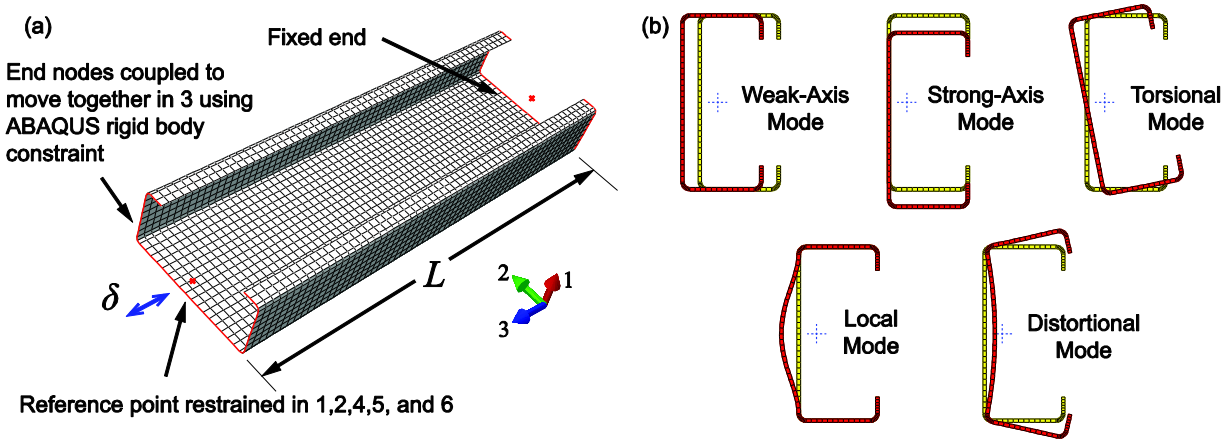

Fig. 4.1. Column model geometry with warping fixed-fixed ends boundary conditions (a), and buckling modes used with the 1D spectral approach to construct the imperfection field imposed to the model (b).

Table 4.1. Column model elastic buckling properties and compressive capacity.

Specimen	L (mm)	$L_{cr\ell}$	F_y (MPa)	P_y (kN)	$P_{cr\ell}$ (kN)	λ_ℓ	P_n (kN)
250S162-68	260	52	417	119	244	0.694	117
250S162-54	269	54	417	96	122	0.881	87
350S162-68	316	63	417	138	149	0.957	119
362S162-68	328	66	417	141	141	0.989	118
400S162-68	366	73	417	148	122	1.091	117
600S200-97	551	110	417	287	216	1.139	218
350S162-54	323	65	417	111	74	1.215	82
362S137-54	335	67	417	102	64	1.245	73
362S162-54	335	67	417	113	71	1.255	81
362S162-54	305	67	417	113	71	1.257	81
362S200-54	335	67	417	128	78	1.271	92
400S137-54	373	75	417	108	56	1.372	72
550S162-68	516	103	417	177	78	1.488	111
600S162-68	567	113	417	186	69	1.617	110
550S162-54	524	105	417	142	39	1.878	76
600S162-54	574	115	417	149	35	2.039	75
600S250-54	574	115	417	180	40	2.093	90
800S200-68	767	153	417	244	51	2.146	117
800S250-68	767	153	417	263	54	2.180	126
800S200-54	775	155	417	195	26	2.705	79
800S250-54	775	155	417	210	27	2.751	85
1000S250-54	976	195	417	241	20	3.387	82

$\lambda_\ell = (P_y/P_{cr\ell})^{0.5}$.

The steel modulus of elasticity is assumed as E=203GPa and Poisson's ratio ν=0.3. Steel plasticity is implemented using the Armstrong-Frederick plasticity model [79] (combined nonlinear isotropic-kinematic hardening with one backstress, α, in ABAQUS) as given by Eq. 4.1-4.2. Isotropic hardening parameters Q_∞ and b and kinematic hardening parameters C_1 and γ_1 were calibrated using true strain-stress curves obtained from steel coupon tests. The steel

plasticity model parameters are kept the same for all columns in the simulation database and are summarized in Table 4.2.

$$\bar{\sigma} = \sigma_y + Q_\infty (1 - e^{-b\bar{\varepsilon}_p}) \tag{4.1}$$

$$\dot{\alpha} = \frac{C_1}{\bar{\sigma}} (\sigma - \alpha) \dot{\bar{\varepsilon}}_p - \gamma_1 \alpha \dot{\bar{\varepsilon}}_p \tag{4.2}$$

Material damage is also simulated to capture the strength and stiffness reduction from tearing and fracture caused by cold-bending and stretching during cyclic loading. The onset of damage and propagation until tearing/fracture of the material is modeled in ABAQUS using the DAMAGE INITIATION and DAMAGE EVOLUTION commands. Damage initiation is implemented using the Bao-Wierzbicki fracture criteria for metal sheets [80,81] to define the fracture locus. This model defines the equivalent strain to fracture $\bar{\varepsilon}_f$ for different average stress triaxiality values $\rho = \sigma_m/\bar{\sigma}$ (σ_m= hydrostatic stress and $\bar{\sigma}$ = von-misses stress) as given by Eq. 4.3,

$$\bar{\varepsilon}_f = \begin{cases} \infty & ,\rho \le -1/3 \\ A/(1+3\rho) & ,-1/3 \le \rho \le 0 \\ A + 9(B-A)\rho^2 & ,0 \le \rho \le 1/3 \\ B/3\rho & ,\rho > 1/3 \end{cases} \tag{4.3}$$

where $A = B(3/4)^{1/2n}$ is the equivalent fracture strain in pure shear, B is the equivalent strain to fracture in uniaxial tension, and n is the hardening exponent if the true stress-strain curve is approximated by the power law $\bar{\sigma} = K\bar{\varepsilon}^n$ (K is a constant). The fracture locus parameters were calibrated using the same stress-strain curves used to calibrate the steel plasticity model following the procedure described in [81]. The values obtained are listed in Table 4.2. The plasticity model and fracture locus were validated by comparing cyclic responses obtained from ABAQUS for two of the local buckling specimens in [77] (362S164-54-LAC# specimens) to the corresponding experimental curves.

Table 4.2. Steel material properties for ABAQUS simulations

σ_y [MPa]	C_1 [MPa]	γ_1 -	Q_∞ [MPa]	b -	A -	B -
416.6	114.7	3.012	295.9	3.468	0.146	0.269

Axial load-displacement (P-δ) monotonic and cyclic responses were obtained for each model in the database. The responses were characterized to obtain the amount of strength degradation, stiffness degradation, hysteretic energy dissipated, and pinching following the

procedures described in [54]. These results are used in the next section to include local buckling in modeling steel column cyclic behavior.

4.2 Axial thin-walled cross-section hysteretic model - asymPinching

This section introduces the asymmetric pinching hysteretic model (herein referred as *asymPinching*) for modeling the axial cyclic behavior in thin-walled steel columns. The model includes a *backbone curve*, a *damage model* with independent definitions for tension and compression excursions, and *unloading-reloading paths* with a tension-to-compression unloading-reloading path definition that reflects the actual behavior observed [77] (see Fig. 4.2). The model follows the same format of the original *Pinching4* model introduced by Lowes et al. [21] with redefined variables to make damage accumulation independent for negative and positive excursions. The generalized expressions for each parameter (as a function of the cross-section local slenderness λ_ℓ) are described next.

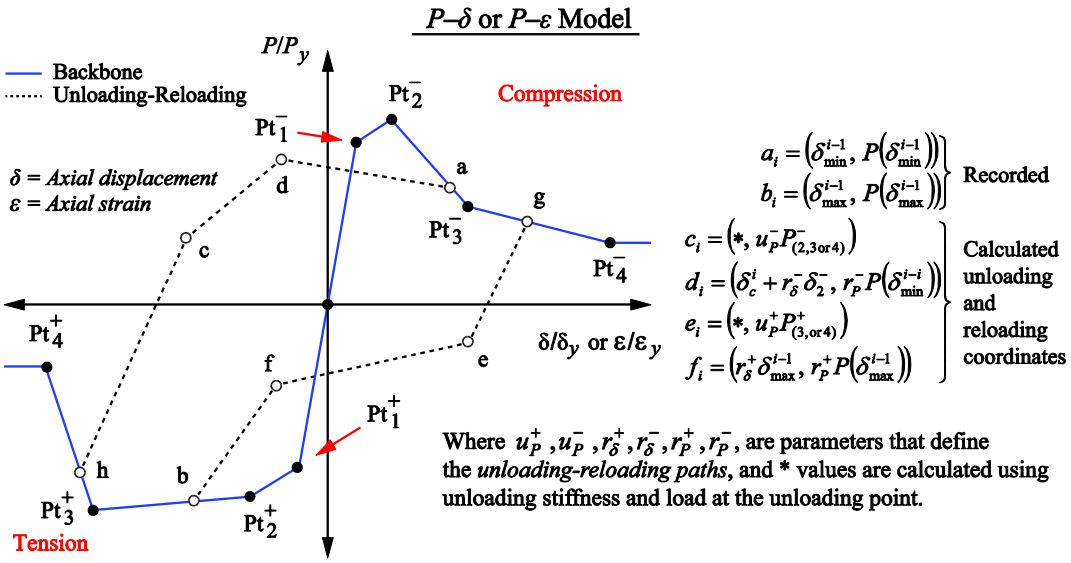

Fig. 4.2. Cross-section hysteretic behavior model for axial members.

4.2.1 Backbone curve

The compression backbone coordinate pairs (δ_i, P_i) [or (ε_i, P_i)] were derived as described in [54] from the monotonic responses. The load values P_i are set as a function of the local slenderness λ_ℓ where the peak load P_2 is set equal to the DSM strength expression in AISI-S100-12 [22]. All values of P_i are limited to a maximum of P_y with the case where all P_i/P_y = 1.0 corresponding to a column with a very stocky cross-section (i.e. compact cross-section). To

determine the displacement δ_1 (strain ε_1) that marks the end of the elastic range in compression (point 1 in Fig. 4.2), it is necessary to calculate the initial stiffness k_1 expressed as a fraction (that depends on λ_ℓ) of the elastic stiffness $k_e=AE/L$ as shown in Fig. 4.3. The expressions for the initial stiffness k_1 and the compressive load P_1 suggests that the cross-section is considered fully effective for $\lambda_\ell \leq 0.689$, and considered slender if $\lambda_\ell > 1.23$. The expressions for the four coordinate pairs (δ_i, P_i) [or (ε_i, P_i)] that define the compression backbone are summarized in Table 4.3 and illustrated in Fig. 4.4.

The tension backbone coordinate pairs (δ_i, P_i) [or (ε_i, P_i)] are set as a function of the yield load P_y and the corresponding elastic yield displacement δ_y (or strain ε_y). Because the *asymPinching* model includes independent damage accumulation for each loading direction, it was not necessary to overestimate the loads P_i in the backbone as described in [54]. The load P_2 was set equal to P_y and some hardening is allowed to account for material hardening that may occur after the cross-section yields by setting the load $P_3 = 1.039P_y$. The tension backbone coordinates are listed in Table 4.4.

Table 4.3. Compression backbone general expressions for local buckling.

Load	Displacement/Strain
$\frac{P_1}{P_y} = \begin{cases} 1.0 & ,\lambda_\ell \leq 0.689 \\ 0.760\lambda_\ell^{-0.737} & ,\lambda_\ell > 0.689 \end{cases}$	$\frac{\delta_1}{\delta_y} = \frac{\varepsilon_1}{\varepsilon_y} = \begin{cases} 1.0 & ,\lambda_\ell \leq 0.689 \\ P_1/k_1 & ,\lambda_\ell > 0.689 \end{cases}$
$\frac{P_2}{P_y} = \begin{cases} 1.0 & ,\lambda_\ell \leq 0.776 \\ \left[1 - 0.15\lambda_\ell^{-2(0.4)}\right]\lambda_\ell^{-2(0.4)} & ,\lambda_\ell > 0.776 \end{cases}$	$\frac{\delta_2}{\delta_y} = \frac{\varepsilon_2}{\varepsilon_y} = \begin{cases} 1.0 & ,\lambda_\ell \leq 0.814 \\ 0.774\left(\lambda_\ell - 0.776\right)^{-0.078} & ,\lambda_\ell > 0.814 \end{cases}$
$\frac{P_3}{P_y} = \begin{cases} 1.0 & ,\lambda_\ell \leq 0.523 \\ 0.552\lambda_\ell^{-0.915} & ,\lambda_\ell > 0.523 \end{cases}$	$\frac{\delta_3}{\delta_y} = \frac{\varepsilon_3}{\varepsilon_y} = \begin{cases} 2.0 & ,\lambda_\ell \leq 0.623 \\ 1.339 + 0.345\lambda_\ell^{-1.371} & ,\lambda_\ell > 0.623 \end{cases}$
$\frac{P_4}{P_y} = \begin{cases} 1.0 & ,\lambda_\ell \leq 0.379 \\ 0.338\lambda_\ell^{-1.119} & ,\lambda_\ell > 0.379 \end{cases}$	$\frac{\delta_4}{\delta_y} = \frac{\varepsilon_4}{\varepsilon_y} = \begin{cases} 6.0 & ,\lambda_\ell \leq 0.857 \\ 5.048 + 0.491\lambda_\ell^{-4.287} & ,\lambda_\ell > 0.857 \end{cases}$
	$\frac{k_1}{k_e} = \begin{cases} 1.0 & ,\lambda_\ell \leq 1.23 \\ 1.075\lambda_\ell^{-0.349} & ,\lambda_\ell > 1.23 \end{cases}$

Table 4.4. Tension backbone general expressions for local buckling.

Load	Displacement/Strain
$P_1/P_y = 0.910$	$\delta_1/\delta_y = \varepsilon_1/\varepsilon_y = 0.910$
$P_2/P_y = 1.000$	$\delta_2/\delta_y = \varepsilon_2/\varepsilon_y = 1.270$
$P_3/P_y = 1.039$	$\delta_3/\delta_y = \varepsilon_3/\varepsilon_y = 8.000$
$P_4/P_y = 0.739$	$\delta_4/\delta_y = \varepsilon_4/\varepsilon_y = 10.00$

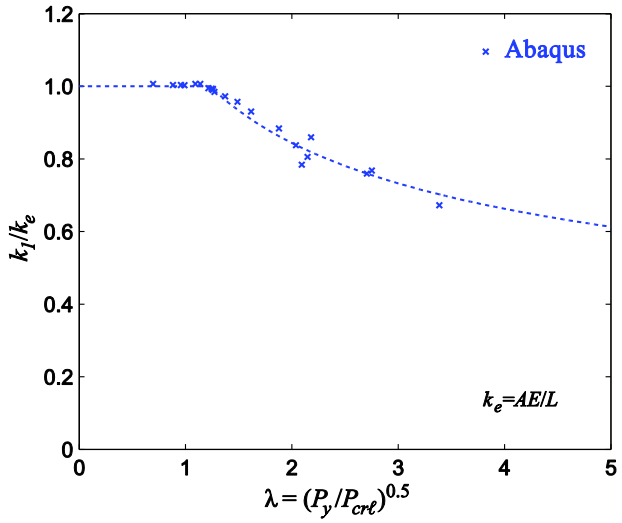

Fig. 4.3. Initial member stiffness as a function of local slenderness.

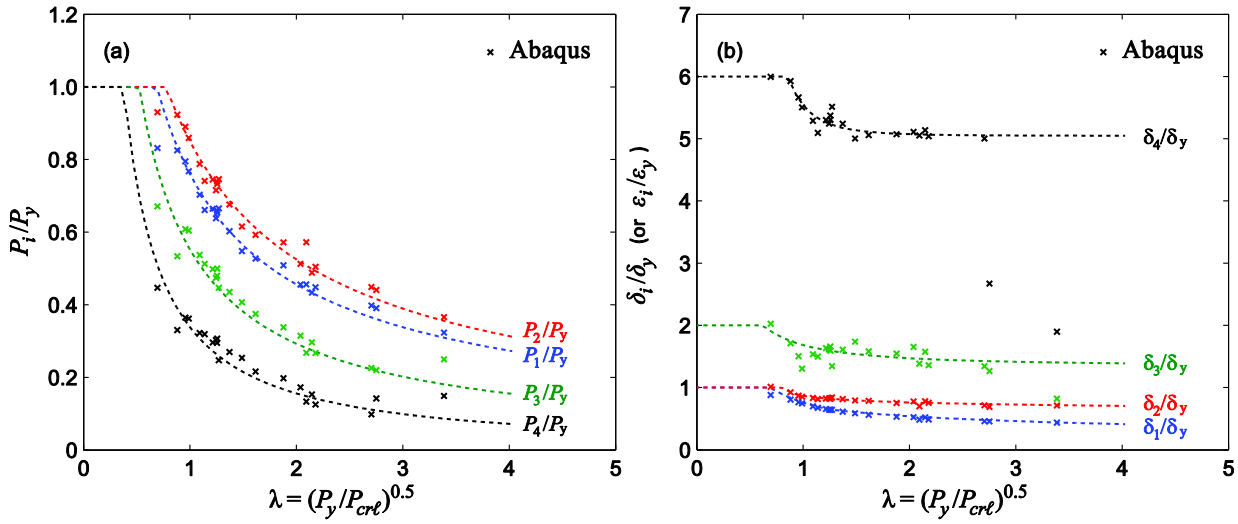

Fig. 4.4. Compression backbone general expressions for local buckling.

4.2.2 Cyclic strength and stiffness degradation

Cyclic strength and stiffness degradation is simulated as a function of the *cumulative hysteretic energy dissipated* in each excursion E_i and the *total energy dissipation capacity* E_T (see section 4.2.3). As more hysteretic energy is dissipated, the ratio E_i/E_T approaches unity where further deterioration is not expected. The functional form for strength and stiffness degradation is given by Eq. 4.4 where the coefficients β_i are calibrated as described further below in this section.

As discussed in [54], cyclic strength and stiffness degradation differ substantially between compression and tension excursions. In *Pinching4*, deterioration of the strength envelope (and stiffness) is defined using the same β_i values for tension and compression. Further, damage accumulated during compression excursions is used to reduce the strength envelope (or stiffness) in subsequent excursions in tension (and vice versa). If damage accumulated from the previous excursion is used in the current (but opposite in direction) excursion, then strength degradation (and stiffness degradation) will be underestimated and overestimated during the compression and tension excursions respectively. In the improved *asymPinching* model, the degradation parameters β_i are defined independently for tension and compression to overcome this shortcoming. Thus, the accumulated damage during compression excursions is not used to reduce the strength envelope (or stiffness) in the subsequent excursions in tension (and vice versa). In CFS axial members, strength degradation develops independently in both loading directions, where loads in tension can reach the yield load P_y despite having experienced deterioration of the compression strength from buckling deformations unless fracture has been initiated. This is the case for example in a member subjected to one sided compression cyclic loading followed by one large tension excursion, where loads close to P_y should be expected. Strains and stresses in tension loading tend to distribute evenly across the member cross-section and compared to compression loading when buckling occurs.

$$\eta_i = \beta_2 \left(E_i / E_T \right)^{\beta_4} \leq 1.0 \tag{4.4}$$

$$f_{\max,i} / f_{\max,o} = 1 - \eta_{is} \geq 0 \tag{4.5}$$

$$k_i / k_1 = 1 - \eta_{ik} \geq 0 \tag{4.6}$$

Strength degradation is characterized as the positive difference in strength between the monotonic backbone force ($f_{max,o}$) and the cyclic force envelope ($f_{max,i}$). Fig. 4.5 shows how strength degrades as a function of the cumulative hysteretic energy E_i where lighter color curves indicate larger slenderness values. It can be seen that strength degradation is cross-section slenderness and member length independent (see Fig. 4.5). Because of this independence, two separate expression for η_{is} are set with constant parameters β_{is} to describe how strength deteriorates as a function of the energy dissipated. Note that there is some residual strength after the energy dissipation capacity is exhausted (i.e., E_i/E_T =1.0). The parameters for strength degradation are listed in Table 4.5.

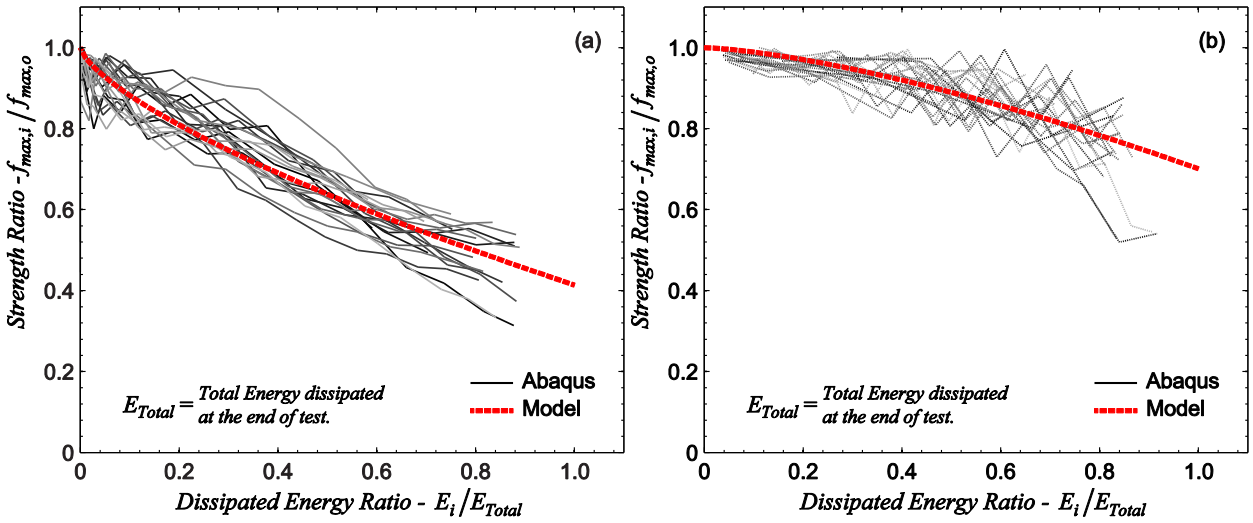

Fig. 4.5. Strength degradation in compression (a) and tension (b) are member length and cross-section slenderness independent

Stiffness degradation is characterized as the ratio between the unloading stiffness in every excursion k_i and the initial stiffness k_1. Fig. 4.6 shows how unloading stiffness degrades as a function of the cumulative hysteretic energy E_i. From the figure it is noted how stiffness in compression degrades faster as the slenderness increases indicated by the lighter colors, while in tension degradation is independent of the member length and cross-section slenderness. In addition, stiffness appears to reduce to zero as the cumulative energy dissipated E_i reaches the maximum value E_T. Therefore, expressions for the parameters β_{is} as a function of the cross-section slenderness were derived for the case of stiffness degradation in compression and are shown in Fig. 4.7. In tension an expression for η_{ik} with constant parameters β_{2s} and β_{4s} is set to describe how stiffness degrades as a function of the energy dissipated. The parameters to define stiffness degradation are listed in Table 4.5.

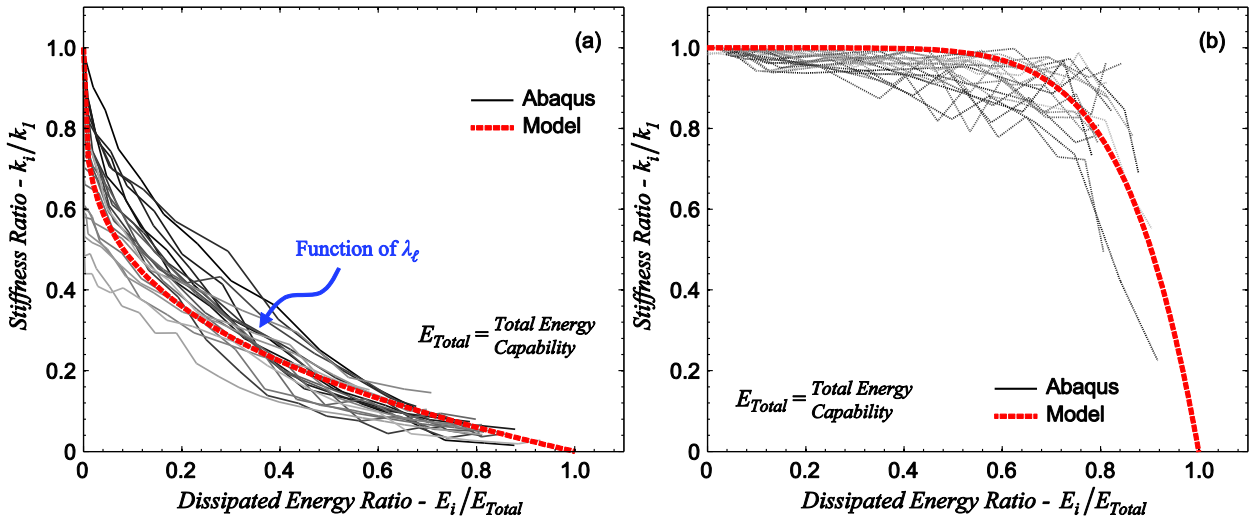

Fig. 4.6. Stiffness degradation in compression (a) is a function of the cross-section slenderness λ_ℓ, while in tension (b) it is member length and slenderness independent.

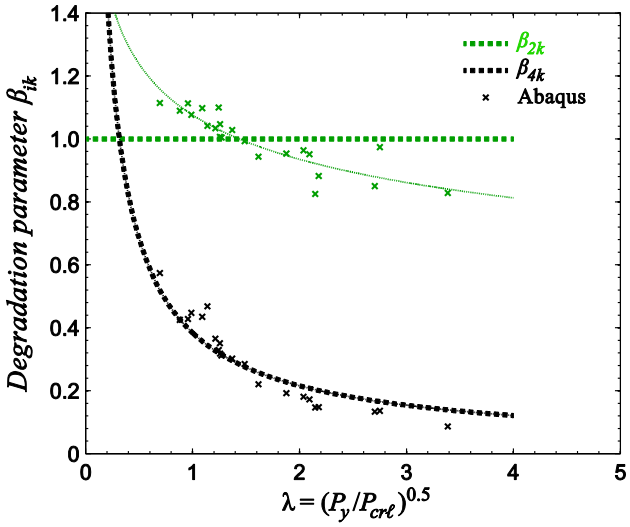

Fig. 4.7. Stiffness degradation parameters as a function of the cross-section slenderness.

Table 4.5. Strength and stiffness degradation parameters.

Loading Direction	Strength Degradation	Stiffness Degradation
Compression	$\beta_{2s} = 0.586,$	$\beta_{2k} = 1.0,$
	$\beta_{4s} = 0.697$	$\beta_{2k} = 0.384\lambda_\ell^{-0.832}$
Tension	$\beta_{2s} = 0.299,$	$\beta_{2k} = 1.0,$
	$\beta_{4s} = 1.438$	$\beta_{4k} = 6.797$

4.2.3 Total energy E_T

It was shown previously that stiffness and strength degrade as a function of the *cumulative hysteretic energy dissipated* in each excursion E_i and the *total energy dissipation capacity* E_T. The total energy dissipation capacity E_T is the maximum value of cumulative hysteretic energy the element is allowed to dissipate. A general expression to calculate E_T for any given member represents a challenge as this value cannot be tied easily to the member strength and properties in a mechanics based manner. However, a heuristic procedure based on the hysteretic energy dissipated per excursion was developed to obtain an expression for E_T given the member cross-section slenderness λ_ℓ.

The procedure to obtain E_T starts by calculating the *hysteretic energy dissipated* per excursion $E_{e,i}$ normalized to an area defined by the maximum load in the corresponding loading direction and the range of deformations of the current excursion (see inset in Fig. 4.8a). If this normalized energy dissipated per excursion ($NHE_{pe,i}$) is plotted versus the cumulative normalized axial deformation ($\sum\delta/\delta_y$), the plot will look like the one shown in Fig. 4.8a. It can be seen that $NHE_{pe,i}$ increases up to a maximum value and then decreases towards zero as cumulative normalized deformation increases. This is a typical behavior observed in all the cyclic responses from the simulation database as shown in Fig. 4.9 and also observed in the experiments described in [77]. Note that the normalized energy dissipated per excursion $NHE_{pe,i}$ decreases with the cross-section slenderness. This is indicated in Fig. 4.9 where slenderness increases from the lighter to darker colors curves.

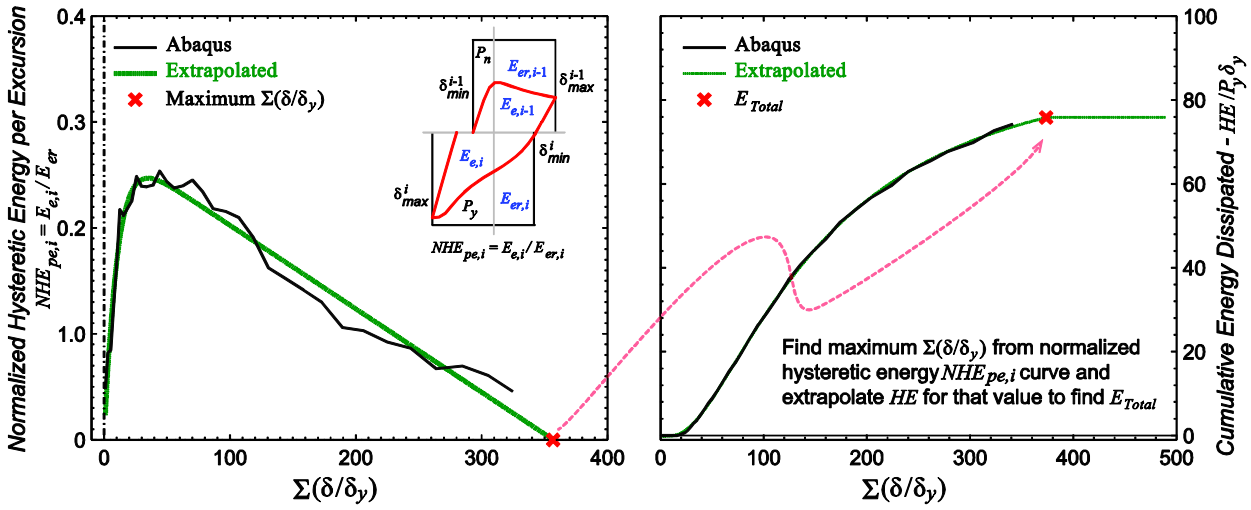

Fig. 4.8. The total energy dissipation capacity E_T is obtained as the cumulative energy dissipated corresponding to a cumulative normalized deformation CDF_0. The cumulative deformation CDF_0 is the value where the normalized hysteretic energy per excursion $NHE_{pe,i}$ vanishes.

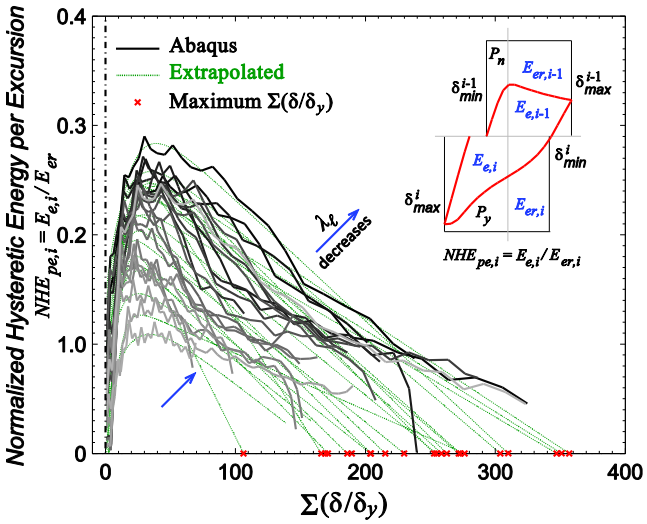

Fig. 4.9. Normalized hysteretic energy dissipated per excursion $NHE_{pe,i}$.

The rationale for estimating E_T therefore is: there should be a cumulative normalized deformation CDF_0 for which $NHE_{pe,i}$ is equal to zero and beyond that point the member is unable to dissipate more energy (see Fig. 4.8). The value for E_T is determined as the cumulative hysteretic energy E_i corresponding to the cumulative normalized axial deformation CDF_0. Values for E_T were estimated for all members in the simulation database and used to obtain the expression in Eq. 4.7 (see Fig. 4.10). Note that E_T increases rapidly to infinite as slenderness λ_ℓ becomes smaller. It is assumed that for the members with a fully effective cross-section (i.e., $\lambda_\ell \leq 0.689$), the slenderness effects on the total energy dissipation capacity are negligible and E_T depends only on the material properties, member length and cross-section area. Thus a maximum limit for the total energy dissipation capacity is proposed at $E_T \leq 113.2 P_y \delta_y$ for all members with fully effective cross-section. This limit is set somewhat arbitrarily and the proposed value requires experimental validation not addressed in this dissertation.

$$\frac{E_T}{P_y \delta_y} = \begin{cases} 113.2 & , \lambda_\ell \leq 0.689 \\ 64.991 \lambda_\ell^{-1.489} & , \lambda_\ell > 0.689 \end{cases} \qquad 4.7$$

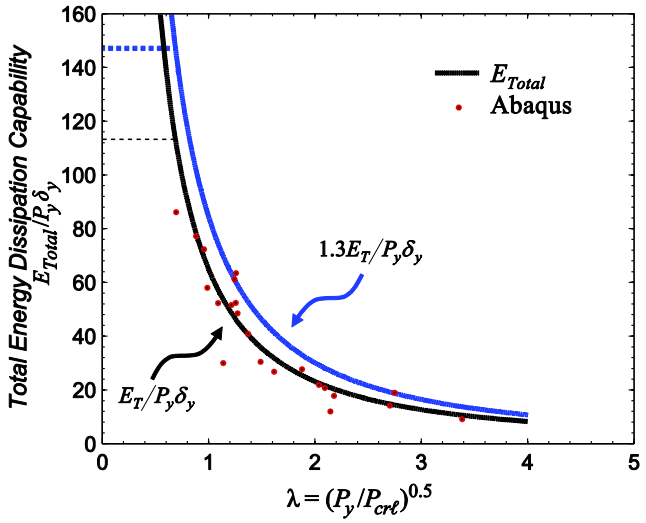

Fig. 4.10. Total energy dissipation capability as a function of the cross-section slenderness.

4.2.4 Unloading-reloading paths

The tension-to-compression reloading path was redefined such that the slopes of segments *h*-*c*, *c*-*d* are positives and decrease in that order (i.e., $k_{hc} > k_{cd}$) to reflect the unloading and reloading up to the peak compressive force in the current excursion. The slope of segment *d*-*a* was set negative to represent the subsequent softening observed in the experimental responses. The points in the tension-compression unloading-reloading path are defined by three parameters u_{P-}, r_{P-} and $r_{\delta-}$. The parameter u_{P-} is the ratio (u_{P-}<1.0) of the load at the point at which reloading in compression starts (point *c* in Fig. 4.2) to the current excursion degraded envelope load P_3 (if $\delta_{min} < \delta_{2+}$), P_4 (if $\delta_{min} < \delta_{3+}$) or P_5 (if $\delta_{min} < \delta_{4+}$). The parameter r_{P-} is the ratio (r_{P-} ≥1.0) of the maximum compression load in the current excursion (point *d*) to the load $P(\delta_{min})$ corresponding to the minimum historic displacement at point *a* (see Fig. 4.2). The load at point *d* is restricted to the maximum load of the current degraded backbone envelope. The displacement at point *d* is defined as the displacement at point *c* plus a fraction $r_{\delta-}$ of the displacement at the peak compression load of the non-degraded backbone envelope ($r_{\delta-}$ ≤1.0).

The compression-to-tension unloading-reloading path is defined using the original definitions from *Pinching4* model. Parameter $r_{\delta+}$ is the ratio of the deformation at which reloading starts (point *f* in Fig. 4.2) to the maximum historic deformation δ_{max}. Parameter r_{P+} is the ratio of the load at the point at which reloading starts (points *f*) to the load corresponding to the maximum historic displacement $P(\delta_{max})$. Parameter u_{P+} is the ratio of the load developed

after unloading (point *e* in Fig. 4.2) to the load coordinate at point 3 of the degraded backbone P_{3+}. Unloading-reloading parameters were obtained as described in [54] for each of the responses in the simulation database and are shown in Fig. 4.11. The figure shows no trend of any of the six parameters with slenderness as well as a lot of scatter. A second calibration exercise was performed to obtain values that worked for all responses in the simulation database resulting in the values summarized in Table 4.9. During the calibration exercise it was necessary to increase 30% the value for the total energy dissipation capacity to be able to match the simulated responses in ABAQUS. Thus, the new design expression for the total energy dissipation capacity is to $1.3E_T$ with E_T as given in Eq. 4.7. Appendix B includes the source code implementing the tension-to-compression unloading-reloading path for the *asymPinching* model.

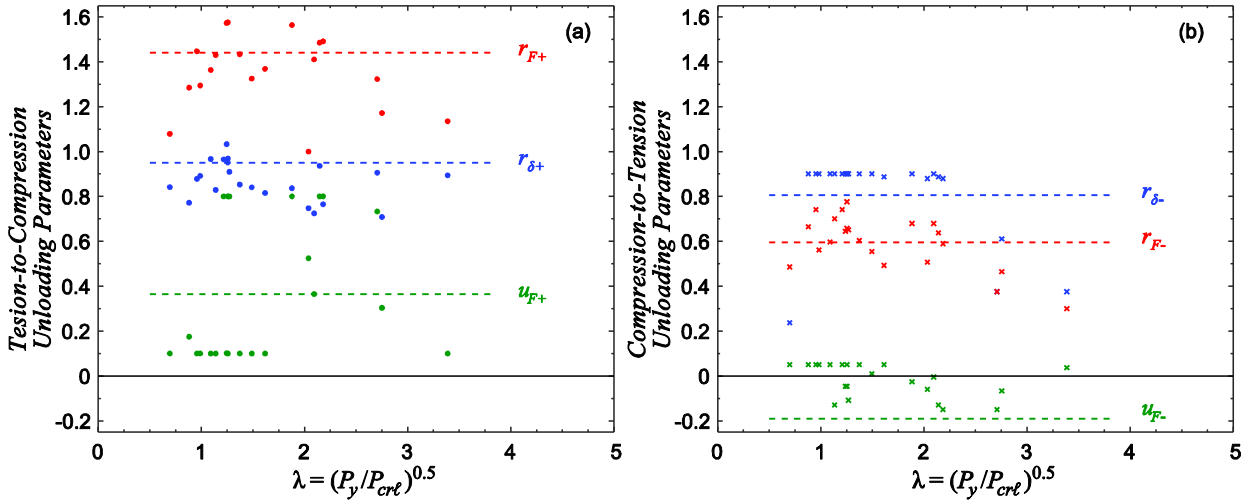

Fig. 4.11. Unloading-reloading path parameters for (a) tension-to-compression and (b) compression-to-tension.

Table 4.6. Unloading-reloading parameters for *asymPinching*.

Parameter	$r_{\delta+}$	r_{P+}	u_{P+}	$r_{\delta-}$	r_{P-}	u_{P-}
Mean	0.652	1.372	0.527	0.418	0.457	-0.022
COV	0.211	0.104	0.236	0.132	0.081	1.702
Adopted	*0.950*	*1.440*	*0.364*	*0.806*	*0.596*	*-0.019*

4.3 Modeling hysteretic behavior including local buckling using Pinching4

The approach presented in the preceding section introduced new definitions for the tension-to-compression unloading-reloading path, and introduced independence in the damage

definition for tension and compression excursions. Even though the *asymPinching* model overcomes the difficulties described in [54] and Chapter 3 when using *Pinching4* to model the cyclic behavior in CFS axial members, the model still requires further validation and code stability checks for different loading cases and boundary conditions. Conversely the *Pinching4* model has been used in several cases for different type of loadings since first introduced that probe the stability of the model and code. For this reason in this section, degradation and pinching parameters are provided to use with *Pinching4* to model cyclic behavior of steel columns including local buckling.

4.3.1 Backbone curve

The backbone curve definitions in compression are defined using the same expressions given in Table 4.3. However, the backbone in tension needs to be modified to overcome the damage underestimation and overestimation issues associated with *Pinching4* when modeling CFS members axial cyclic behavior. The tension backbone coordinates in Table 4.7 are proposed herein for used with *Pinching4*. This backbone in tension is defined based on the tension side of the cyclic envelopes obtained from the simulation database.

Table 4.7. Tension backbone for steel column modeling using *Pinching4*.

Load	Displacement/Strain
$P_1/P_y = 1.044$	$\delta_1/\delta_y = \varepsilon_1/\varepsilon_y = 1.044$
$P_2/P_y = 1.134$	$\delta_2/\delta_y = \varepsilon_2/\varepsilon_y = 1.404$
$P_3/P_y = 1.172$	$\delta_3/\delta_y = \varepsilon_3/\varepsilon_y = 8.0$
$P_4/P_y = 0.872$	$\delta_4/\delta_y = \varepsilon_4/\varepsilon_y = 10.0$

4.3.2 Cyclic strength and stiffness degradation

Cyclic strength and stiffness degradation parameters for *Pinching4* were derived in the same fashion as previously described for the *asymPinching* model. Degradation is defined as a function of the *cumulative hysteretic energy dissipated* in each excursion E_i and the *total energy dissipation capacity*, where E_T is defined by Eq. 4.7. Unlike the *asymPinching* model, and as pointed out in [54], strength and stiffness degradation in *Pinching4* is defined using the same set of parameters for both loading directions. These parameters are calibrated using the average of the strength and stiffness degradation in both excursions.

Strength and stiffness degradation as a function of the energy dissipated is compared Fig. 4.12 to the expressions (blue dashed-lines) proposed herein to model deterioration in *Pinching4* (see Eq. 4.4-4.6). Damage parameters β_{2s} and β_{4s} are set constant as strength degradation is member length and cross-section slenderness independent in both tension and compression. Stiffness degradation parameters β_{2k} and β_{4k} on the other hand are defined as a function of the cross-section slenderness λ_ℓ as shown in Fig. 4.13. The strength and stiffness degradation parameters are derived after taking the average of the degradation curve in compression and the respective curve in tension. The expressions for strength and stiffness degradation parameters β_2 and β_4 are summarized in Table 4.8.

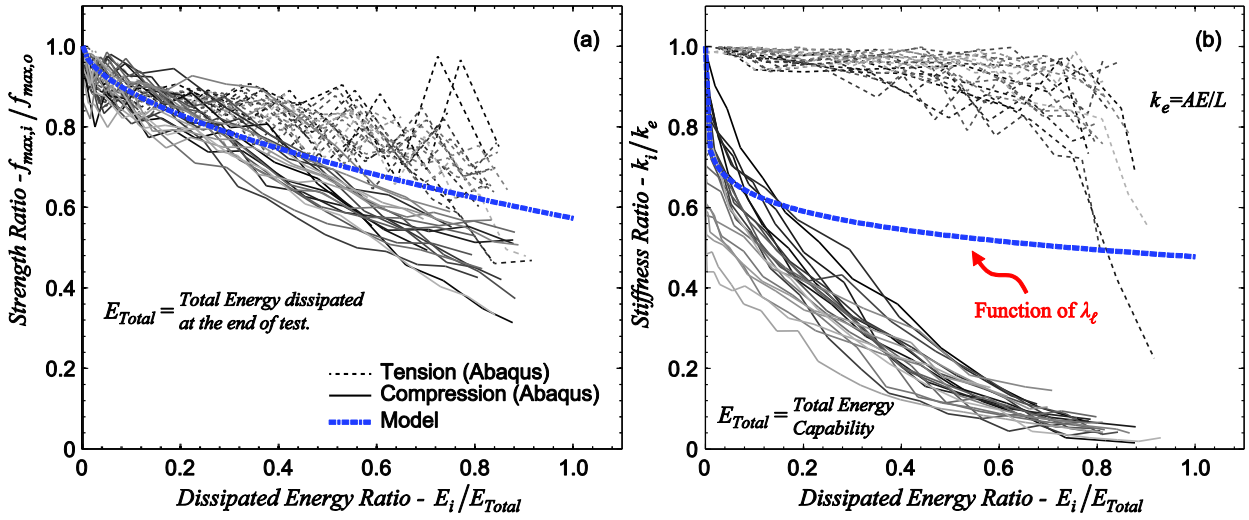

Fig. 4.12. Strength degradation (a) is member length and cross-section slenderness independent, while stiffness degradation (b) is a function of the member cross-section slenderness. Damage parameters are defined using the average damage in tension and compression (blue dashed-lines).

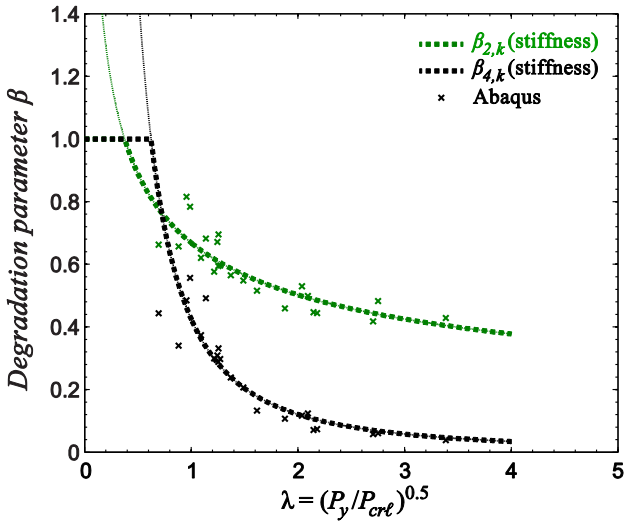

Fig. 4.13. Stiffness degradation parameters for *Pinching4* as a function of the cross-section slenderness.

Table 4.8. Strength and stiffness degradation parameters for *Pinching4*.

Strength Degradation	Stiffness Degradation
$\beta_{2,s} = 0.427$ $\beta_{4,s} = 0.569$	$\beta_{2,k} = \begin{cases} 1.0 & ,\lambda_\ell \le 0.377 \\ 0.669\lambda_\ell^{-0.412} & ,\lambda_\ell > 0.377 \end{cases}$ $\beta_{4,k} = \begin{cases} 1.0 & ,\lambda_\ell \le 0.624 \\ 0.425\lambda_\ell^{-1.814} & ,\lambda_\ell > 0.624 \end{cases}$

4.3.3 Unloading-reloading paths

The six parameters, u_{P+}, u_{P-}, $r_{\delta+}$, $r_{\delta-}$, r_{P+} and r_{P-} that define the unloading-reloading paths in *Pinching4* are shown in Fig. 4.14. The parameters $r_{\delta-}$ and $r_{\delta+}$ are the ratio of the deformation at which reloading starts (points *d* and *f* in Fig. 3.1d) to the maximum/minimum historic deformation, δ_{min} and δ_{max}. Parameters r_{P-} and r_{P+} are the corresponding ratios of the load at the point at which reloading starts (points *d* and *f*) to the load corresponding to the maximum historic displacement, $f(d_{min})$ and $f(d_{max})$. Parameters u_{P-} and u_{P+} are the ratios of the load developed after unloading (point *c* and *e* in Fig. 3.1d) to the load coordinate of backbone point 3, P_{3-} and P_{3+}. Note that the definitions of these parameters apply for both loading directions, however values for tension-to-compression different than compression-to-tension unloading-reloading can be specified. The values in Fig. 4.14 show that u_{P+}, u_{P-}, $r_{\delta+}$, $r_{\delta-}$, r_{P+} and r_{P-} are similar for all members in the simulation database and therefore and average value was adopted (see Table 4.9).

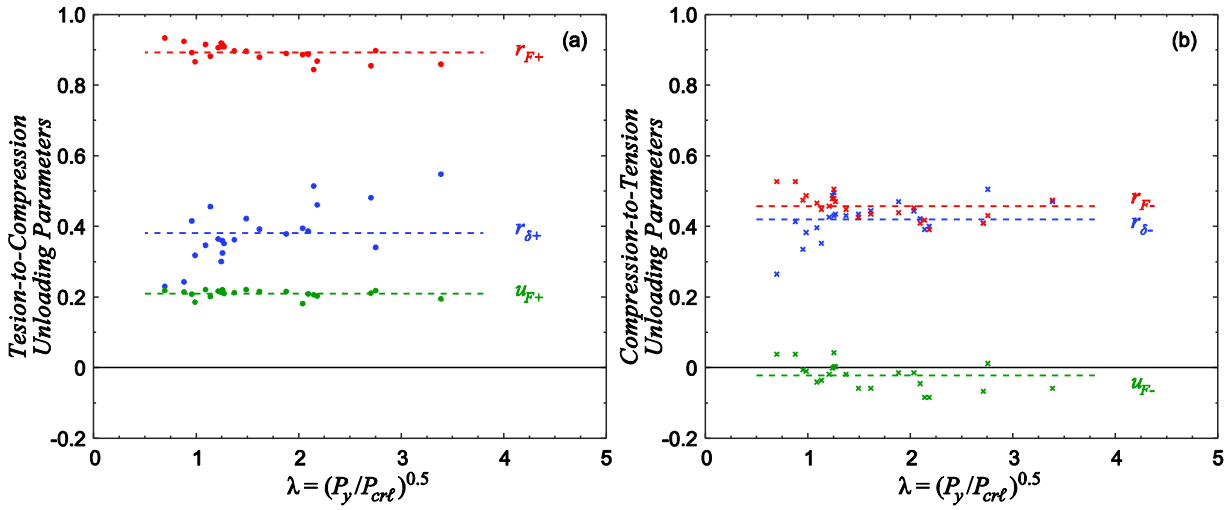

Fig. 4.14. *Pinching4* unloading-reloading path parameters for (a) tension-to-compression and (b) compression-to-tension.

Table 4.9. Unloading-reloading parameters for *Pinching4*.

Parameter	$r_{\delta+}$	r_{P+}	u_{P+}	$r_{\delta-}$	r_{P-}	u_{P-}
Mean	0.381	0.892	0.210	0.419	0.457	-0.022
COV	0.207	0.026	0.052	0.130	0.081	-1.702

4.4 Simulating the axial cyclic response including local buckling using asymPinching

Modeling the cyclic response of the local buckling members in [77] using the *asymPinching* model shows the capabilities of the latter to describe properly the response. The load-deformation *P-δ* response of the four axial members tested and those in the simulation database were calculated using *asymPinching* and previously derived expressions. The response was also calculated using *Pinching4* to evaluate the performance of the proposed model. Comparison of the responses in Fig. 4.15 shows that *asymPinching* captures the response more accurately than *Pinching4* including the unloading-reloading from tension-to-compression as well as the cumulative energy dissipation. The energy dissipated at the end of the simulations when using the *asymPinching* is in average 10% to 20% higher compared to the responses from the database and the experimental response for members 362LAC in [77] (see Fig. 4.16a). Additionally, the root mean-squared deviation between the predicted load responses using *asymPinching* to the ABAQUS simulations and tests is less than 15% and the responses for the 362LAC members (8% and 9%) falls within the trend shown in Fig. 4.16b. The model does not capture well the energy dissipated at the end of the test for the 600LAC members as E_{model}/E_{test} was very small and the root mean-squared deviation fell away from the error trend shown in Fig. 4.16b. The observed errors in energy and load steam mostly from the fact that the unloading-

reloading path is defined with the same parameters for all cycles the member may experience. As noted in [54] these parameters vary every cycle and accounting for this variation should reduce the errors observed.

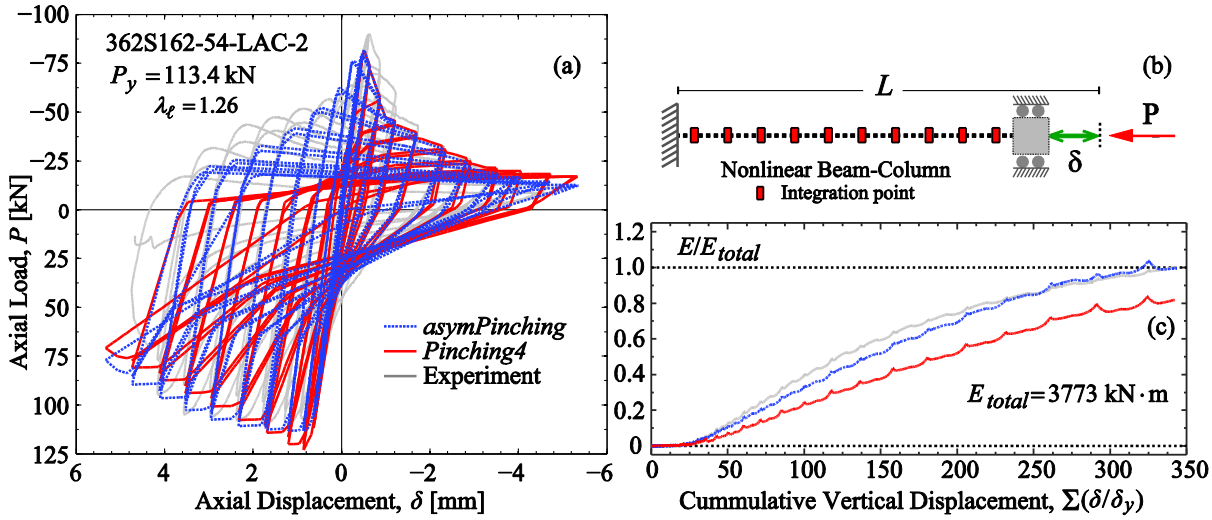

Fig. 4.15. Simulated response using the *asymPinching* model captures better the response (a) and energy dissipated (b) when compared to *Pinching4*.

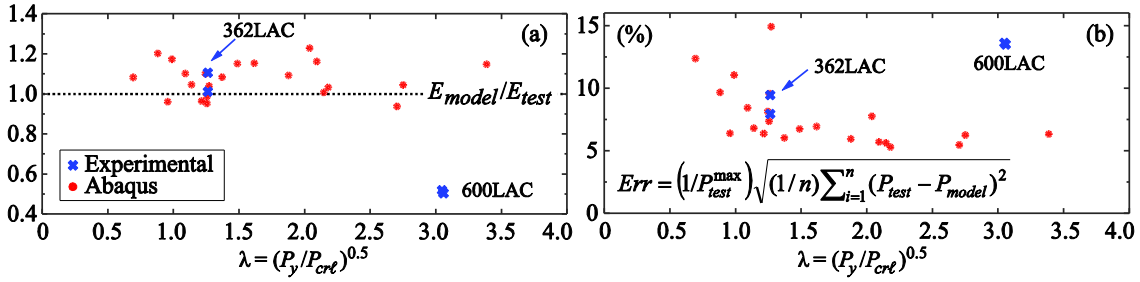

Fig. 4.16. Energy dissipation (a) from the *asymPinching* model is slightly higher than in ABAQUS simulations. The root mean-squared deviation (b) of the predicted load using *asymPinching* to the ABAQUS simulations is between 5% to 15%.

The following observation needs mentioning when using the *dispBeamColumn* (or similar) element from OpenSees in conjunction with the distributed nonlinearity approach to model thin-walled axial members. Since this approach assumes a uniform distribution of the axial strains along the member, the damage and inelastic strains localization behavior observed in the plate study from Chapter 2 and experiments is not captured. This can be visualized from the example in Fig. 4.17 which compares monotonic responses of a uniformly axially loaded member modeled using both the spring and the distributed nonlinearity approach. The curves show the displacement δ applied at the top end versus the axial reaction P at the bottom support.

The two models produce the same *P*-δ response, however from Fig. 4.18 can be seen that localization of inelastic behavior does not occur in the member with distributed nonlinearity since all cross-sections deform the same. On the other hand the spring model inherently concentrates all nonlinear behavior at the bottom end.

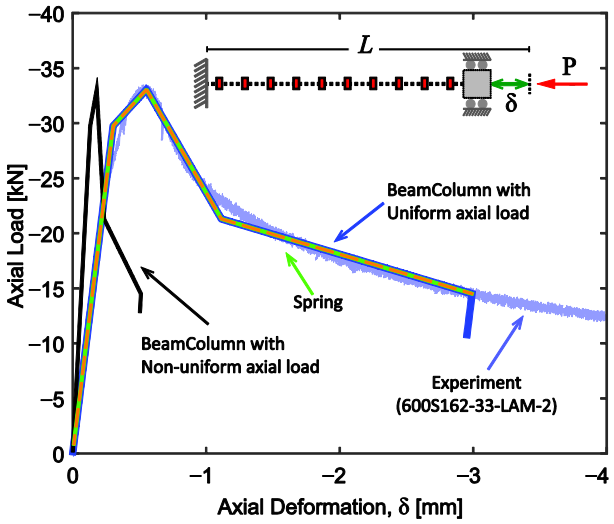

Fig. 4.17. Comparison between spring model and nonlinear beam-column model.

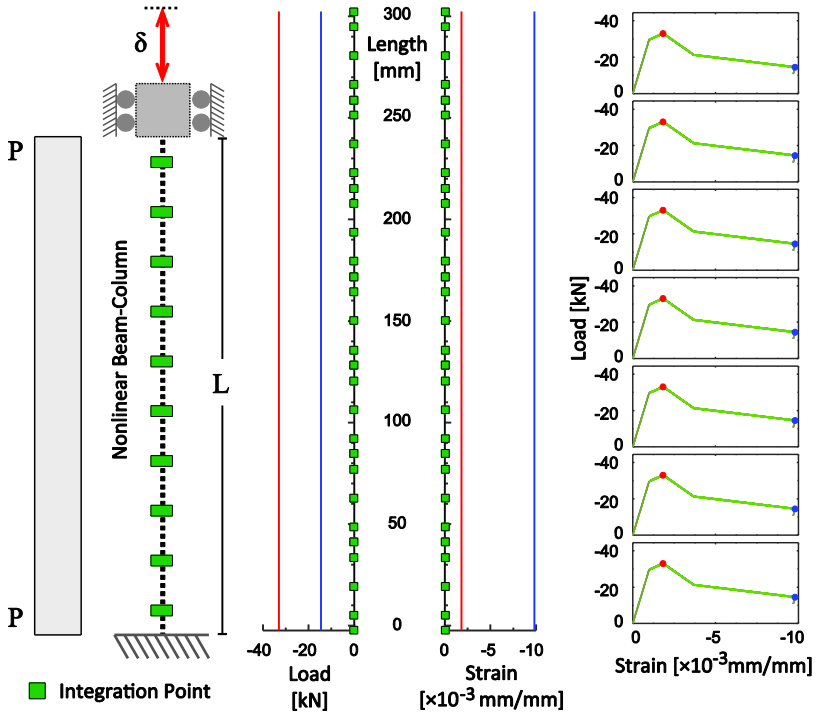

Fig. 4.18. Axial member subjected to uniform load showing all cross-sections deforming the same amount and localization of inelastic strains is not present.

Now comparing the response for same the column but subjected to non-uniform distributed axial load, the *P*-δ responses obtained using both approaches are not the same, see Fig. 4.17. The response from the spring model is exactly the same as for the uniform load case since the parameters defining its behavior are kept the same as the uniform load. This results suggest the displacement backbone coordinates need modification to accommodate this loading case. For the distributed nonlinearity model, the response appears stiffer than the uniform load case, and with displacements at the top end smaller than those from the spring model. Localization is observed for the distributed nonlinearity approach as shown in Fig. 4.19 where cross-sections towards the bottom end are in the inelastic range while towards the top cross-sections unloaded and remained linear elastic.

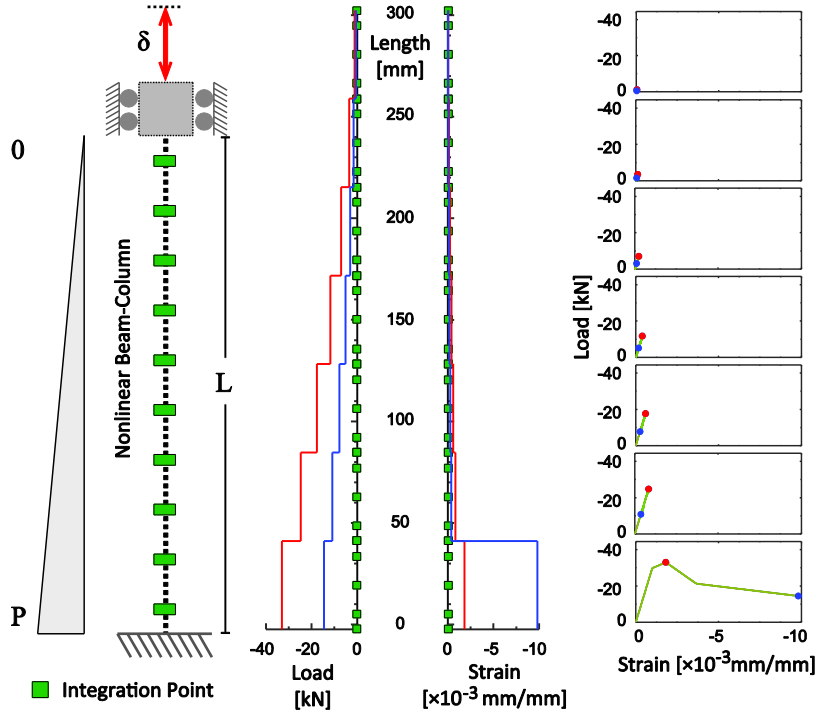

Fig. 4.19. Axial member subjected to non-uniform load showing localization of inelastic behaviour at the bottom end.

One can conclude from the two comparisons that because of the uniform axial strain distribution assumption used in the *dispBeamColumn* (or similar) element, the localization behavior cannot be captured for the case of uniform axial load using the distributed nonlinearity approach. If capturing localization is of interest, then using the spring modeling approach is suggested and the user is required to select a priori the location where all nonlinearity will

concentrate. Selecting the location of the spring can be difficult if the axial load can become non-uniformly distributed along the member at any time during the analysis.

For members subjected to non-uniform distributed axial load, inelastic behavior localization may occur automatically when the most stressed/loaded cross-cross-section starts softening resulting in unloading of the adjacent cross-sections. This type of behavior can be simulated with the *dispBeamColumn* element (or similar) and does not require the user to consider where nonlinear behavior will concentrate before running an analysis. Even tough localization cannot be captured using the distributed nonlinearity approach for the case of uniform axial load, the energy dissipation and the load-deflection response P-δ are still properly captured.

The proposed methodology is established for thin-walled cold-formed steel members, however the *asymPinching* parameters are presented generally as a function of local buckling slenderness λ_ℓ and could be extended to hot-rolled steel members and cross-sections with future validation. Moreover, the methodology presented can be applied to thin-walled cold-formed steel members that experience distortional and global buckling deformations with further finite element validation. In the next chapter the *asymPinching* model is used to explore local buckling effects in the response of sheathed cold-formed steel shear walls and demonstrate how to implement this into structural system analyses.

Chapter 5: Nonlinear Hysteretic Models for Cold-Formed Steel Screw-Fastened Connections Simulation

Typical connections in cold-formed steel buildings include steel-to-steel and steel-to-sheathing (wood/gypsum) connections such as those shown Fig. 5.1. In this chapter a hysteretic model for simulating screw-fastened connections subjected to shear forces (i.e., forces perpendicular to the fastener longitudinal axis) is proposed. The hysteretic model is aimed to capture the cyclic shear force-deformation response and energy dissipation of common for common CFS connections limit states including tilting, bearing, tilting + bearing, and screw shear limit states. Model parameters can be formulated as functions of the fastener type (i.e., screw size, and head type), connecting parts thickness, and boundary conditions around the screw. However, the work presented in this chapter focuses on evaluating and developing an efficient model for finite element analysis that is easy to implement rather than obtaining general expressions for the model parameters themselves.

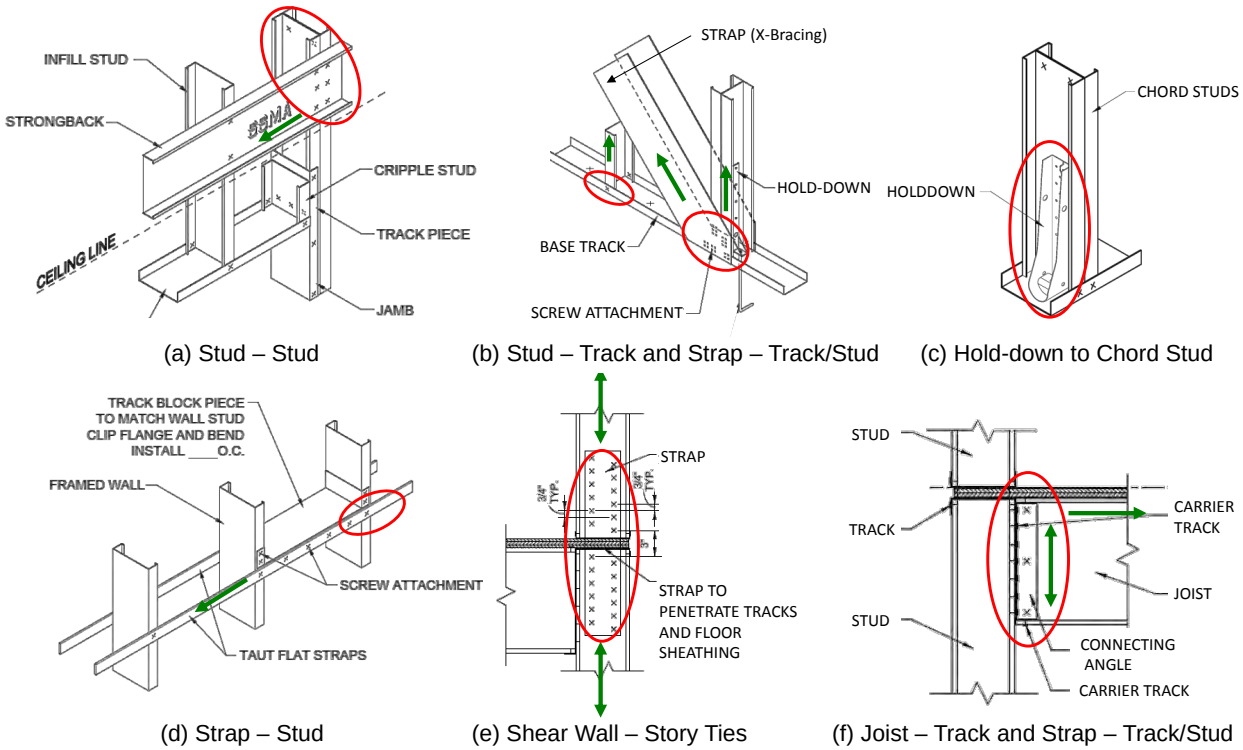

(a) Stud – Stud (b) Stud – Track and Strap – Track/Stud (c) Hold-down to Chord Stud

(d) Strap – Stud (e) Shear Wall – Story Ties (f) Joist – Track and Strap – Track/Stud

Fig. 5.1. Typical screw-fastened cold-formed steel connections.

It has been shown with experiments and simulations that cold-formed steel to sheathing connections dictates the behavior in the commonly used sheathed shear walls used for cold-formed steel buildings [87, 88, 89]. Experimental research [95] was conducted on CFS-sheathing connections to characterize their hysteretic response (see Fig. 5.2). A total of 24 cold-formed steel to sheathing connections were tested varying sheathing materials, steel ply thickness and fastener spacing to study their influences. The test results were fitted to *Pinching4* material model. The fitted material model served as important input for the shear wall numerical studies presented later in the following chapters. In the following section a review of common approaches used to model screw-fastened connections by previous researchers is reviewed as it provides background for the model implementation in ABAQUS discussed towards the end of this chapter.

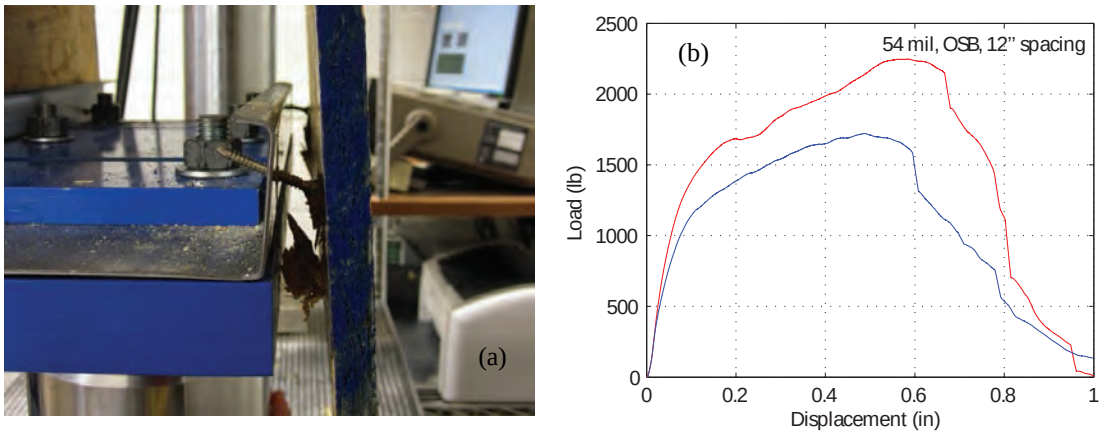

Fig. 5.2. CFS-sheathing connection test (a) and monotonic response (b).

5.1 Reviewing of some numerical models for fastened connections

5.1.1 CASHEW fastened connection based shear wall modeling

CASHEW stands for "Cyclic Analysis of Shear Walls" [90] and it is written for wood framed shear wall analysis. In this software, framing members are modeled as rigid members with pin-ended connections. As a result, the framing system itself without sheathing deforms as a mechanism and provides no lateral stiffness (see Fig. 5.3). It also ignores any out-of-plane deformations in the shear wall. From these assumptions, the equilibrium equation are formulated using the principle of virtual work considering only the contributions to the virtual work from sheathing and connections.

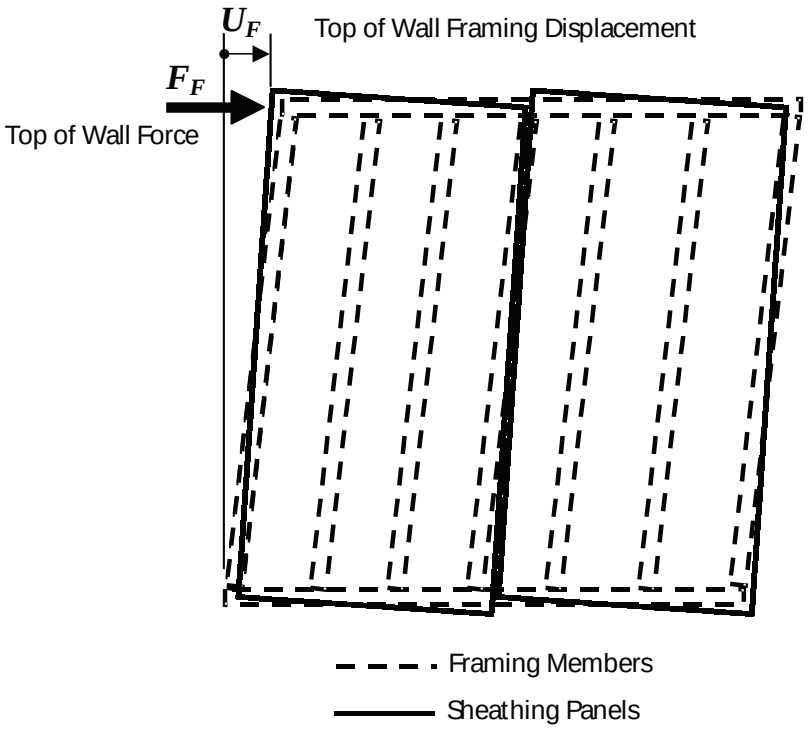

Fig. 5.3. Shear wall deformation in CASHEW

Framing-sheathing connection are defined with the hysteresis model in Fig. 5.4 originally proposed by [91]. The hysteresis model can simulate pinching behavior with strength and stiffness degradation. Connections are modeled as a pair of orthogonal uncoupled springs both assigned with this hysteresis model. The reason behind this modeling approach results from the complexity of connector behavior. The deformation trajectory of a connector under a monotonic analysis of the shear wall was found to be almost unidirectional and a single nonlinear spring was supposed to be suitable for monotonic analysis [90]. However, under cyclic analysis, the connector displacement trajectory was bi-directional making it difficult to differentiate positive and negative connection displacement. To avoid this displacement sign issue, uncoupled spring pair model was adopted in CASHEW.

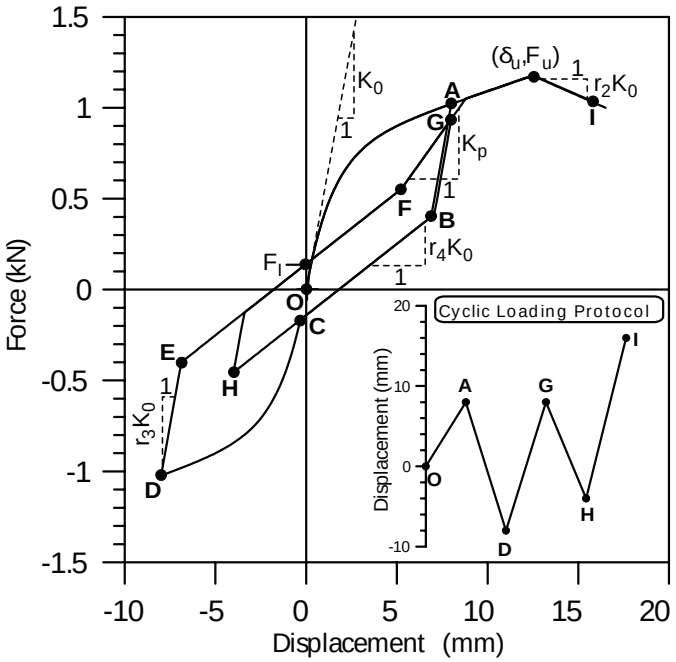

Fig. 5.4. Connection hysteresis model adopted in CASHEW

This uncoupled spring pair model results in an overestimation of connection strength and stiffness. An internal adjustment strategy was adopted inside the program to overcome this obstacle. The strategy reduced the connector spacing, and therefore the number of connections, to match the energy absorbed in a monotonic analysis by the two-spring model with energy in the one-spring model [90]. With this adjustment, connection strength and stiffness overestimation was alleviated but not generally solved.

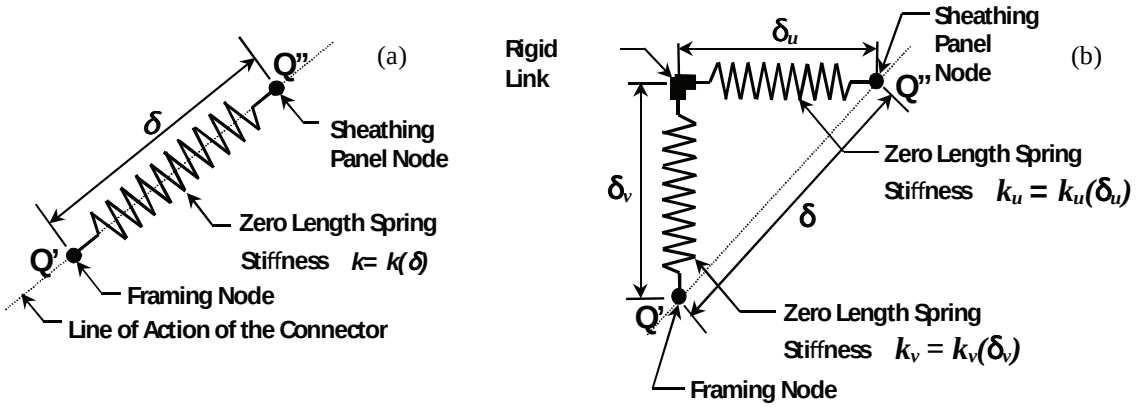

Fig. 5.5. Single spring model (a), and uncoupled spring pair model (b).

CASHEW used displacement control and the Newton-Raphson method to find shear wall load-deformation response. It was found that the shear wall global tangent stiffness can become non-positive definite and the solution strategy would sometimes struggle to converge. To overcome this numerical issue, CASHEW internally added an axial spring at the top of shear wall to ensure that combine global tangent stiffness remained positive definite during analysis [92].

5.1.2 OpenSees fastened connection based shear wall modeling

Models implemented in OpenSees featuring monotonic and cyclic analysis have been well studied [84, 87]. In these OpenSees models the CFS-sheathing connections are modeled using *CoupledZeroLength* elements (Fig. 5.6), which are assigned the hysteretic behavior model *Pinching4*. Two features make the *CoupledZeroLength* element very suitable for modeling CFS-sheathing connections. First, the element is a single shear spring capable of rotating its orientation in the plane of the shear wall. Therefore, the connection strength and stiffness are not overestimated in comparison to the CASHEW uncoupled spring pair model discussed in previous section. Also, *CoupledZeroLength* determines connection positive and negative displacement by element orientation. This ensures that positive and negative displacement can be differentiated for a bidirectional trajectory.

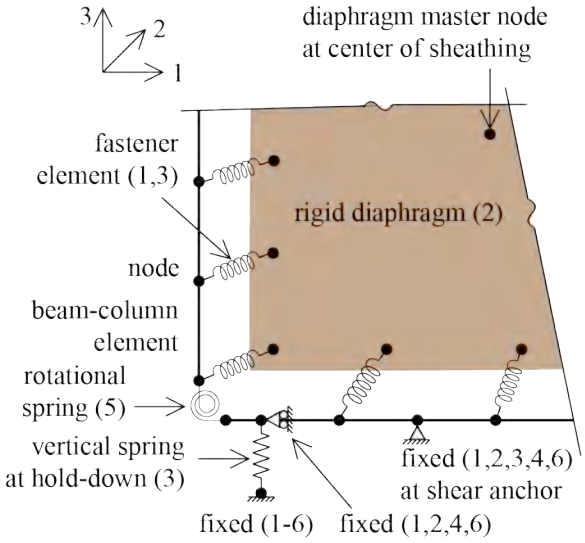

Fig. 5.6. CFS framed shear wall model in OpenSees

5.1.3 Modeling fastened connection in ABAQUS

Modeling sheathed CFS shear walls using high fidelity finite element models (e.g., thin-shell elements models in ABAQUS), in addition to the overall wall behavior, they can also provide additional details of the members and sheathing behavior (e.g., buckling deformations). For this more detailed models the CFS-sheathing connections is modeled using SPRINGA elements (Fig. 5.7). SPRINGA is a 2-node axial spring element in ABAQUS. Two important features make it suitable for modeling CFS-sheathing connections. Unlike conventional spring elements, SPRINGA considers geometric nonlinearity. This means that its line of action can be rotated during analysis instead of being fixed to X, Y or Z directions. This feature avoids overestimation of connection strength and stiffness. Also, some level of material nonlinearity is included in this model, see Fig. 5.7.

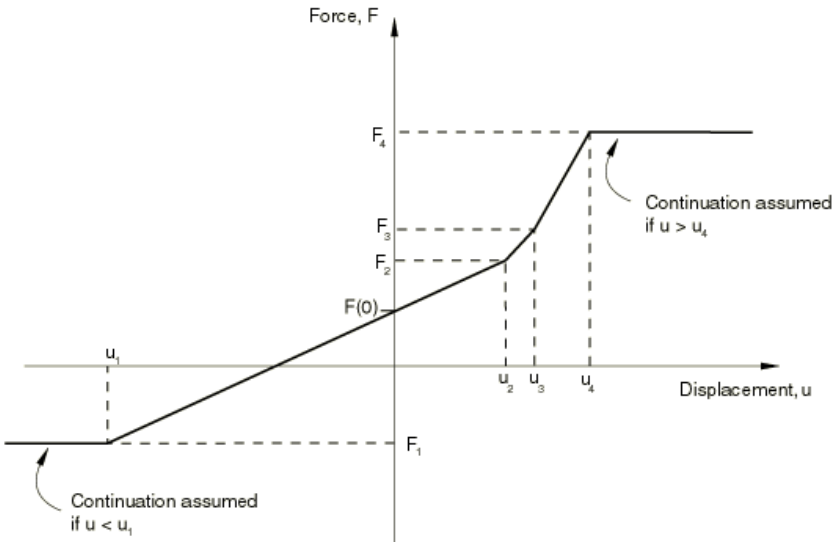

Fig. 5.7. Nonlinear spring force–relative displacement relationship for SPRINGA in ABAQUS

However, shear wall model with CFS-sheathing connections modeled by SPRINGA can only be used for monotonic analysis. Due to software limitations, complete CFS-sheathing connection hysteresis cannot be defined in SPRINGA because the model lacks definitions for cyclic strength and stiffness degradations, as well as definitions for nonlinear inelastic loading reloading paths. To achieve high-fidelity modeling applicable to both monotonic and cyclic analysis, ABAQUS needs an extension that incorporates complete CFS-sheathing connection hysteresis and algorithm resolving this bidirectional trajectory issue. The following sections describes the implementation of a spring model for ABAQUS that overcomes the difficulties

mentioned when using SPRINGA. The model is implemented to simulate the behavior of CFS screw-fastened connection subjected to shearing forces as observed in the experiments [95].

5.2 CSF Connection hysteretic model using ABAQUS user element (UEL)

A user element subroutine (UEL) is not a standalone program that can conduct finite element analysis. It needs to be linked to ABAQUS. Once linked, UEL will be called every time when ABAQUS needs information from the UEL (Fig. 5.8). In each call by ABAQUS, the UEL will be provided with element geometry information (coordinates, displacement and etc.), UEL properties, and solution-dependent variables from the last increment and analysis procedures. By using the information provided by ABAQUS, the UEL calculates and returns to ABAQUS a Jacobian matrix and force residuals contributed by the UEL and the updated solution-dependent variables. Solution-dependent variables are carried in a vector where users can save data to be used in the next increment. It is the only way that element loading history can be retrieved.

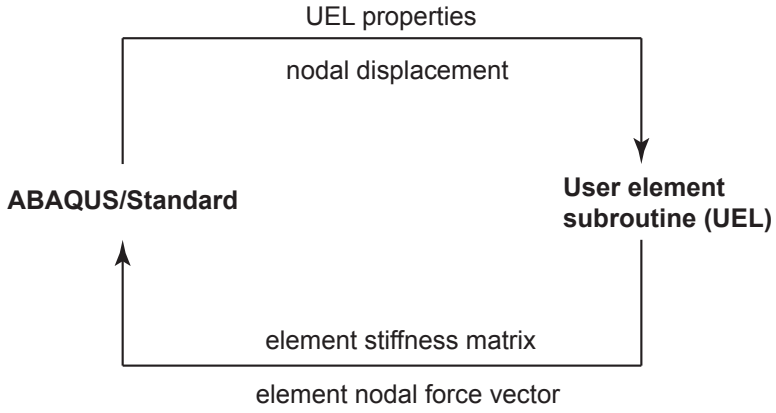

Fig. 5.8. ABAQUS-UEL work flow diagram

In order to model nonlinearity of screw-fastened connections, the Pinching4 model is implemented inside the UEL. The implementation is made possible by three important sections in the UEL (Fig. 5.9). A local subroutine is coded to calculate element deformation and orientation based on geometric information from ABAQUS. Given the element deformation, the *Pinching4* model returns element force and stiffness. With the element force and stiffness, several local subroutines return element nodal force vector and stiffness matrix. Table 5.1 lists the local subroutines responsible for the functions discussed above.

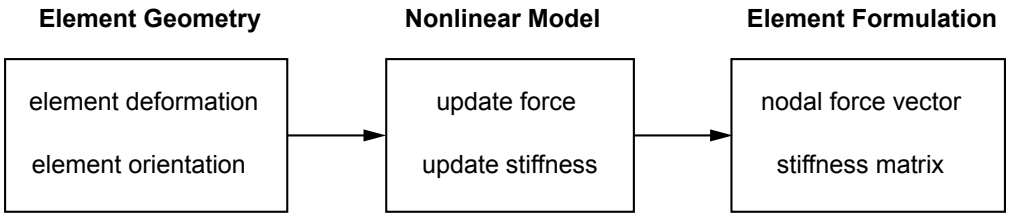

Fig. 5.9. UEL computational work-flow.

Table 5.1. Local subroutines used in the UEL

Subroutine	Output
SGEOM(…)	Return spring deformation, orientation
PINCHING4(…)	Return spring force and stiffness
SAMATRX(…)	Return element stiffness matrix
SNFORCE(…)	Return element nodal force vector
SUEL2PIN(…)	Converts data from soultion-depedent variable vector to Pinching4 local variables
SPIN2UEL(…)	Converts data from Pinching4 local variables to solution-depedent variable vector
SetEnvelop(…)	Sets the initial backbone envelope for the material based upon the input by the user
revertToStart(…)	Initialization process for the material at start
revertToLastCommit(…)	Return back to its last commited state in case the analysis fails
setTrialStrain(…)	Sets a displacement demand of the material based upon its previous stiffness and also the residual force vector return
commitState(…)	Commits the history variables of the material model after the state-check has been done for the material model
getstate(…)	Determines the state of the material based upon the material history and current stress demand
posEnvlpStress(…) negEnvlpStress(…)	Returns positive/negative damaged stress of the material
posEnvlpTangent(…) negEnvlpTangent(…)	Returns positive/negative tangent of the material
Envlp3Stress (…) Envlp4Stress (…)	Determines the stress of the envelope at state 3 or state 4 of the material
Envlp3Tangent (…) Envlp4Tangent (…)	Determines the tangent of the envelope at state 3 or state 4 of the material
updateDmg(…)	Apply stiffness and strength degradations

As shown in Table 5.1, the local subroutine PINCHING4 is where the hysteretic behavior is directly implemented. The C++ source code of the Pinching4 model from OpenSees was translated into FORTRAN with a few modifications made to fit ABAQUS coding style (implicit variable declaration). The implementation uses solution-dependent variables to retrieve loading history and determine the evolutionary load paths and damage rules. For this purpose, all *Pinching4* variables are saved into a solution-dependent variable vector (SVARS) at the end of each increment so that these parameters can be retrieved in the next increment.

Screw-fastened connections are idealized as springs with independent behavior in the positive and negative loading excursions. Four different behaviors are implemented in the UEL as described in the following sections. Any of these behaviors can be selected for simulating screw-fastened connections. The objective is to provide users with flexibility in simulations. All these spring models are intended to only simulate connection shear behavior. Fastener withdrawal behaviors (i.e., pull-out or pull-though) are not considered here and can be a topic for future study. Thus, all of the spring models work in 2-dimensional plane – sheathing or diaphragm plane. Because ABAQUS allows user element to have 3D coordinates but only 2D degrees-of-freedoms, the UEL proposed herein can still be used for 3D analysis in ABAQUS.

5.2.1 Model 1: Uncoupled two-spring model

Uncoupled two-spring model is a model composed of two orthogonal springs aligned in the global X and Y directions as shown in Fig. 5.10. Each spring is assigned with *Pinching4* material of the same properties.

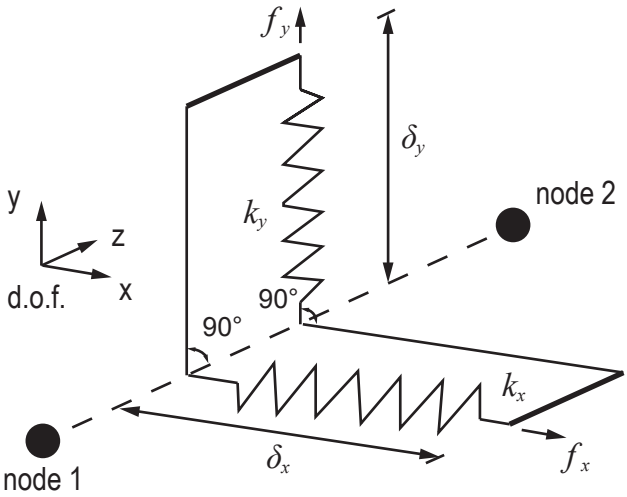

Fig. 5.10. Uncoupled two-spring model for CFS screw-fastened connections

The force resultant of the two springs represents the connection resisting force. The stiffness matrix **K** and nodal force vector **F** are,

$$\mathbf{K} = \begin{bmatrix} k_x & 0 & -k_x & 0 \\ 0 & k_y & 0 & -k_y \\ -k_x & 0 & k_y & 0 \\ 0 & -k_y & 0 & k_y \end{bmatrix} \tag{5.1}$$

$$\mathbf{F} = \begin{Bmatrix} -f_x & -f_y & f_x & f_y \end{Bmatrix}^T \tag{5.2}$$

The advantage of the two-spring model is that it is very “stable”. The spring orientations are fixed in global X and Y directions so that divergence induced by spring changing orientation is not a big concern. The disadvantage is overestimation of connection strength and stiffness.

5.2.2 Model 2: Oriented spring-pair model

Oriented spring pair model is an improved version of uncoupled two-spring model proposed by Judd [93] to alleviate strength and stiffness overestimation. Still, each spring is assigned with the Pinching4 material model of the same properties. Compared to the uncoupled two-spring model, two orthogonal springs are not oriented towards the global X and Y directions. Instead, spring orientations are determined based on the initial spring deformation trajectory. In practice, in the 1st increment, uncoupled two-spring model is used. The spring deformation (δ_{x0}, δ_{y0}) from the 1st increment is then utilized to establish spring orientations for all the following increments.

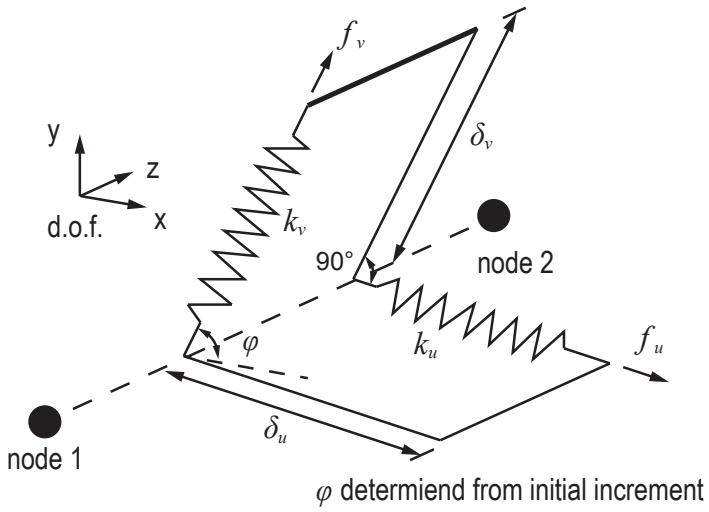

Fig. 5.11. Oriented spring-pair model for CFS screw-fastened connections

With spring orientations established, the element stiffness matrix K and nodal force vector F can be written as

$$\mathbf{K} = \begin{bmatrix} K_{11} & K_{12} & -K_{11} & -K_{12} \\ K_{12} & K_{22} & -K_{12} & -K_{22} \\ -K_{11} & -K_{12} & K_{11} & K_{12} \\ -K_{12} & -K_{22} & K_{12} & K_{22} \end{bmatrix} \tag{5.3}$$

$$K_{11} = K_u \cos^2\varphi + K_v \sin^2\varphi \tag{5.4}$$

$$K_{12} = (K_u - K_v)\sin\varphi\cos\varphi \tag{5.5}$$

$$K_{22} = K_u \sin^2\varphi + K_v \cos^2\varphi \tag{5.6}$$

$$\mathbf{F} = \begin{Bmatrix} F_u\cos\varphi - F_v\sin\varphi \\ F_u\sin\varphi + F_v\cos\varphi \\ -F_u\cos\varphi + F_v\sin\varphi \\ -F_u\sin\varphi - F_v\cos\varphi \end{Bmatrix} \tag{5.7}$$

5.2.3 Model 3: Coupled two-spring model

Coupled two-spring model is a spring model available in OpenSees named *CoupledZeroLength*. It is a pair of orthogonal coupled springs aligned in global X and Y directions where the resultant deformation is calculated following the diagram shown in Fig. 5.12. In contrast to uncoupled two-spring model and oriented spring pair, only a *Pinching4* material model is assigned. Instead of spring deformation in global X and Y directions, the spring deformation resultant is input to the *Pinching4* material model which outputs the spring force resultant. The coupling between X and Y directions are achieved by transforming spring force to X and Y directions as shown in Eq.5.9. However, though with coupling, the spring stiffness matrix is in the uncoupled format as shown in equation 5.8.

$$\mathbf{K} = \begin{bmatrix} k & 0 & -k & 0 \\ 0 & k & 0 & -k \\ -k & 0 & k & 0 \\ 0 & -k & 0 & k \end{bmatrix} \tag{5.8}$$

$$\mathbf{F} = \begin{Bmatrix} -f\cos\varphi \\ -f\sin\varphi \\ f\cos\varphi \\ f\sin\varphi \end{Bmatrix} \tag{5.9}$$

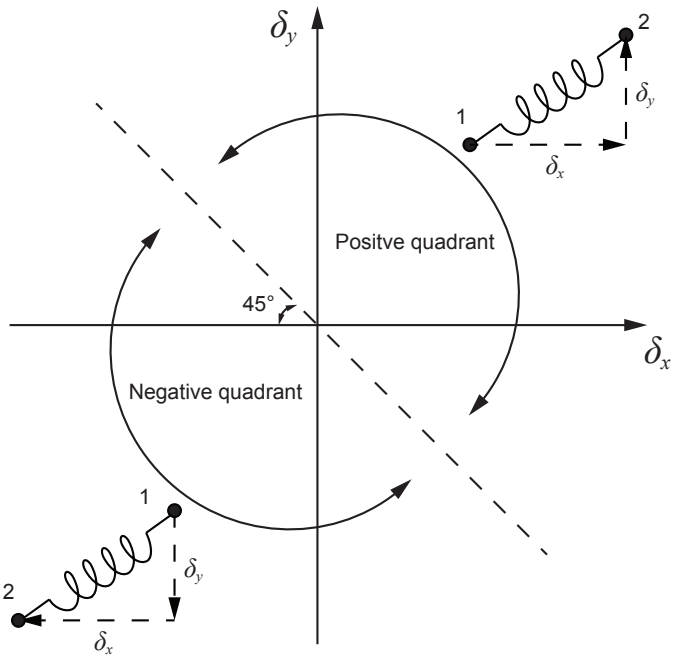

Fig. 5.12. Deformation quadrants of coupled two-spring model.

5.2.4 Model 4: Radial spring model

The radial spring model, shown in Fig. 5.13, is a single spring model capable of updating its orientations in an analysis. Previous research indicated that single spring model is very suitable in simulating connection behavior. However, because single spring model cannot simulate “bi-directional” or cyclic deformation, this model is not applied to cyclic analysis. In order to simulate bi-directional deformation, a radial spring adopts a set of deformation quadrants so that “positive” and “negative” spring deformation can be differentiated. This set of deformation quadrants is an improved version of its counterpart in the coupled two-spring model in 5.2.3. Instead of being divided by X+Y=0 line, deformation quadrants are divided based on spring initial deformation trajectory as depicted in Fig. 5.14. Assuming that spring deformation trajectory does not change over a 90° angle, the quadrant division line is orthogonal to the initial spring deformation trajectory.

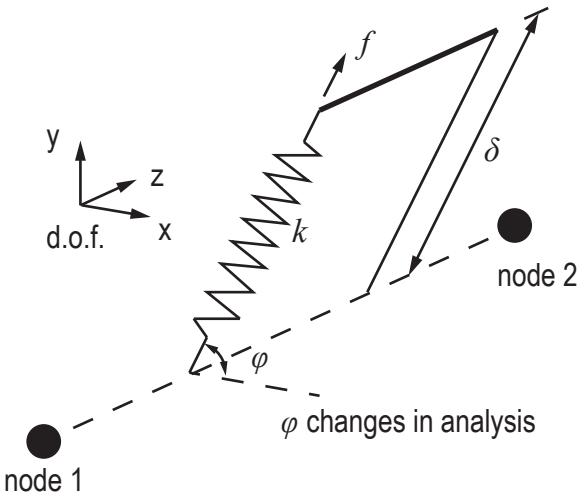

Fig. 5.13. Radial spring model

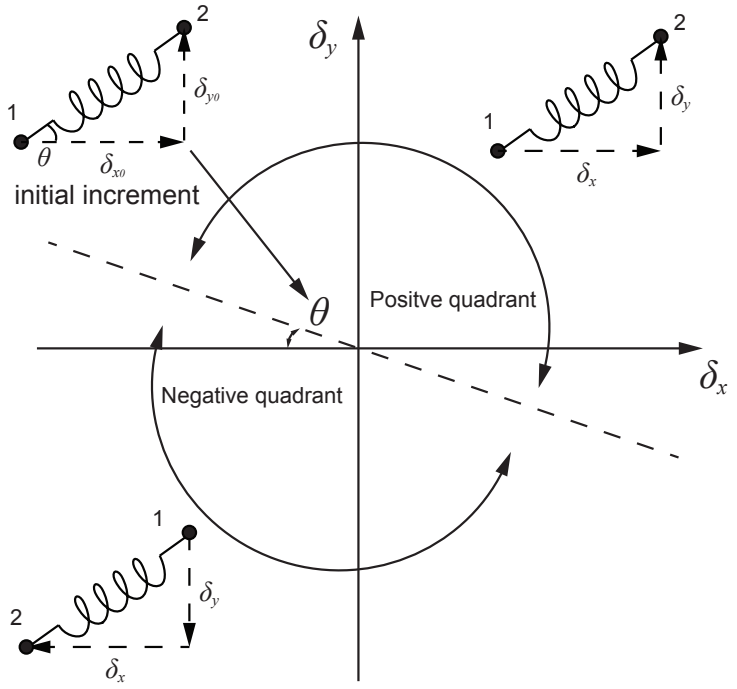

Fig. 5.14. Deformation quadrants of radial spring

Because geometric nonlinearity will be activated in high fidelity shear wall modeling, spring element geometric nonlinearity need to be included. This is accomplished by corotational formulation [94]. Corotational formulation allows the spring element to update its orientation at each increment. The element stiffness matrix **K** and nodal forces are calculated as

$$\mathbf{K} = \mathbf{K}_e + \mathbf{K}_g \qquad 5.10$$

$$\mathbf{K_e} = \begin{bmatrix} k\cos^2\varphi & k\cos\varphi\sin\varphi & -k\cos^2\varphi & -k\cos\varphi\sin\varphi \\ k\cos\varphi\sin\varphi & k\sin^2\varphi & -k\cos\varphi\sin\varphi & -k\sin^2\varphi \\ -k\cos^2\varphi & -k\cos\varphi\sin\varphi & k\cos^2\varphi & k\cos\varphi\sin\varphi \\ -k\cos\varphi\sin\varphi & -k\sin^2\varphi & k\cos\varphi\sin\varphi & k\sin^2\varphi \end{bmatrix} \quad 5.11$$

$$\mathbf{K_g} = \begin{bmatrix} f/l & 0 & -f/l & 0 \\ 0 & f/l & 0 & -f/l \\ -f/l & 0 & f/l & 0 \\ 0 & -f/l & 0 & f/l \end{bmatrix} \quad 5.12$$

$$\mathbf{F} = \begin{Bmatrix} -f\cos\varphi \\ -f\sin\varphi \\ f\cos\varphi \\ f\sin\varphi \end{Bmatrix} \quad 5.13$$

where

k = spring axial stiffness

f = spring axial force

l = spring current length

φ = angle between spring deformation and global X axis

The user element proposed herein is a combination of *Pinching4* nonlinear hysteretic model and spring element formulation. The four spring models previously described have all attached the hysteretic *Pinching4* model. In the next chapter, the Model 4 (radial spring model) is selected to be attached with Pinching4 model for verification.

5.3 Verification of the UEL implementation

To ensure a successful implementation of the connection model in ABAQUS, the proposed ABAQUS user element (UEL) is verified against OpenSees. For this purpose, two sets of parameters are selected for validating backbone, unloading–reloading path, and degradation.

5.3.1 Backbone and unloading–reloading path verification

A screw-fastened steel to OSB connection is modeled to validate the backbone and the pinching path. The connection is modeled using a *zeroLength* element in OpenSees and UEL (*Model 4* - radial spring) in ABAQUS. As shown in Fig. 5.15, the node 1 is restrained at the

degree-of-freedoms UX and UY, while node 2 is restrained only in the direction UY. The prescribed displacement history shown in Fig. 5.16 is applied in the UX direction at node 2.

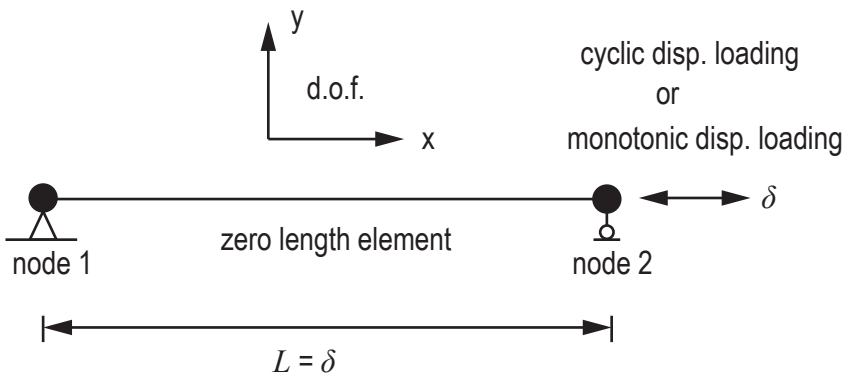

Fig. 5.15. Model using the proposed UEL for backbone and unloading-reloading path verification

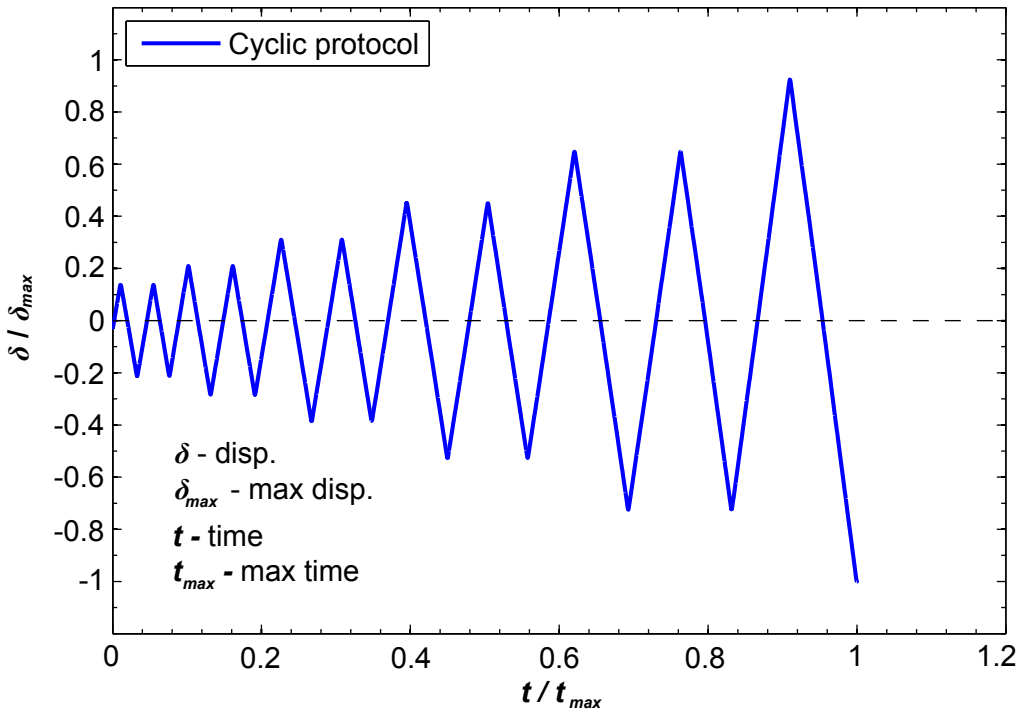

Fig. 5.16. Prescribed displacement history

A total of 6 CFS-sheathing connection tests are simulated respectively in ABAQUS and OpenSees. All *Pinching4* model parameters and loading protocols are taken from steel-to-OSB connection test data conducted by [95]. Backbone and pinching path parameters used in the

verification models are adopted from the work presented by [95] and is listed by convenience in Table 5.2. For this verification, degradation parameters are set to be zero.

Table 5.2. Parameters for backbone and unloading-reloading path verification examples

Model	ePd_1	ePd_2	ePd_3	ePd_4	ePf_1	ePf_2	ePf_3	ePf_4	eNd_1	eNd_2	eNd_3	eNd_4	eNf_1	eNf_2	eNf_3	eNf_4
	(in.)				(kip.)				(in.)				(kip.)			
c33-o6-1	0.018	0.069	0.241	0.540	0.158	0.298	0.371	0.021	-0.024	-0.077	-0.267	-0.494	-0.211	-0.313	-0.427	-0.052
c33-o12-1	0.021	0.050	0.207	0.446	0.142	0.211	0.327	-0.013	-0.019	-0.085	-0.266	-0.447	-0.123	-0.248	-0.324	-0.018
c54-o6-1	0.016	0.064	0.241	0.344	0.160	0.286	0.409	0.022	-0.025	-0.097	-0.223	-0.402	-0.234	-0.374	-0.475	-0.056
c54-o12-1	0.019	0.077	0.230	0.427	0.207	0.381	0.475	0.054	-0.019	-0.114	-0.258	-0.445	-0.204	-0.361	-0.466	-0.065
c97-o6-1	0.011	0.041	0.084	0.229	0.164	0.313	0.359	0.015	-0.012	-0.049	-0.112	-0.234	-0.194	-0.361	-0.380	-0.004
c97-o12-1	0.011	0.036	0.067	0.121	0.218	0.405	0.475	0.049	-0.010	-0.040	-0.088	-0.132	-0.197	-0.432	-0.494	-0.038

Fig. 5.17 and Fig. 5.18 compare the load deformation response and energy dissipation obtained using the UEL in ABAQUS to the *zeroLength* spring model in OpenSees for a 54mils to 7/16 in. OSB connection with a 6 in. screw spacing (c54o6_1 in Table 5.2). It can be seen that the load deformation and energy dissipation responses are identical. Similar results obtained for the other connections listed in Table 5.2 are provided in Appendix XX. The identical backbone and unloading-reloading behaviors obtained using the both models are proof that the UEL backbone and unloading-reloading path behavior are successfully implemented in ABAQUS.

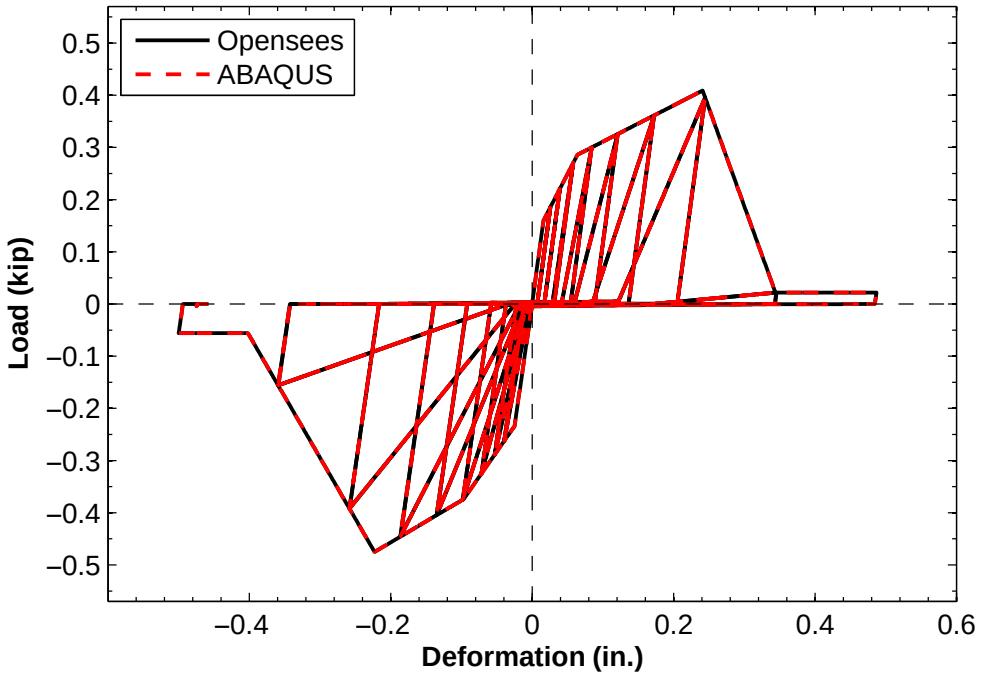

Fig. 5.17. Load-deformation response for test c54o6_1

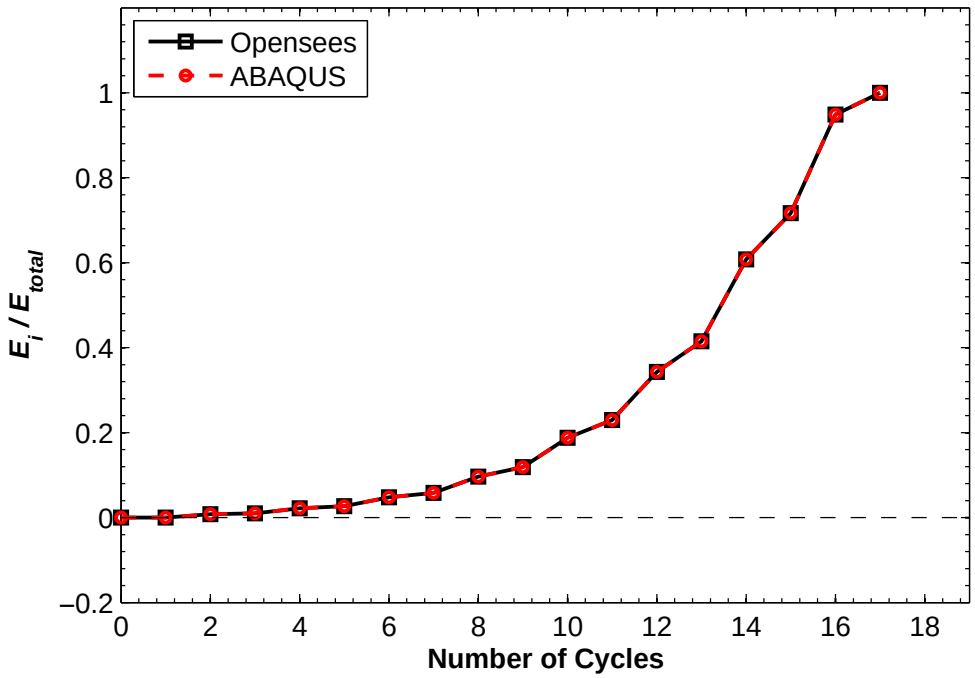

Fig. 5.18. Energy dissipation for test c54o6_1

5.3.2 Cyclic strength and stiffness degradation verification

The model in Fig. 5.15 is provided with parameters to simulate degradation for validation of the UEL implementation. The hysteretic model parameters are listed in Table 5.3 and Table 5.4. The degradation parameters listed in Table 5.4 were defined arbitrarily to test the UEL, however they do not necessarily represent actual CFS screw-fastened connection behavior. Strength degradation, unloading stiffness degradation and reloading degradation are studied independently. Fig. 5.19 to 5.24 show that the load deformation and energy dissipation obtained using the UEL are identical to the ones obtained in OpenSees. Thus, strength and stiffness degradation are successfully implemented in the UEL.

Table 5.3. Backbone coordinates for degradation verification examples.

ePd_1	ePd_2	ePd_3	ePd_4	eNd_1	eNd_2	eNd_3	eNd_4	ePf_1	ePf_2	ePf_3	ePf_4	eNf_1	eNf_2	eNf_3	eNf_4
(in.)				(in.)				(kip)				(in.)			
0.020	0.078	0.246	0.414	-0.020	-0.078	-0.246	-0.414	0.220	0.350	0.460	0.049	-0.220	-0.350	-0.460	-0.049

Table 5.4. Degradation parameters for degradation verification examples

Degradation	γ_1	γ_2	γ_3	γ_4	γ_{lim}
Unloading stiffness	0.250	0.850	0.650	0.120	1000.000
Reloading stiffness	2.740	0.240	1.720	0.980	1000.000
Strength	0.160	1.170	0.530	0.460	1000.000

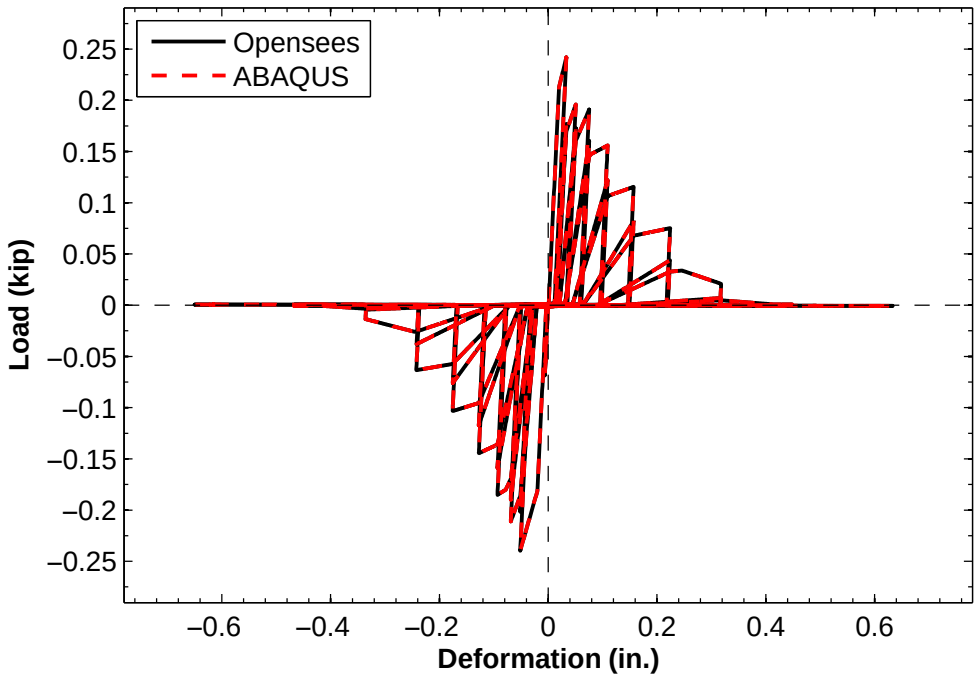

Fig. 5.19. Load-deformation for strength degradation verification case

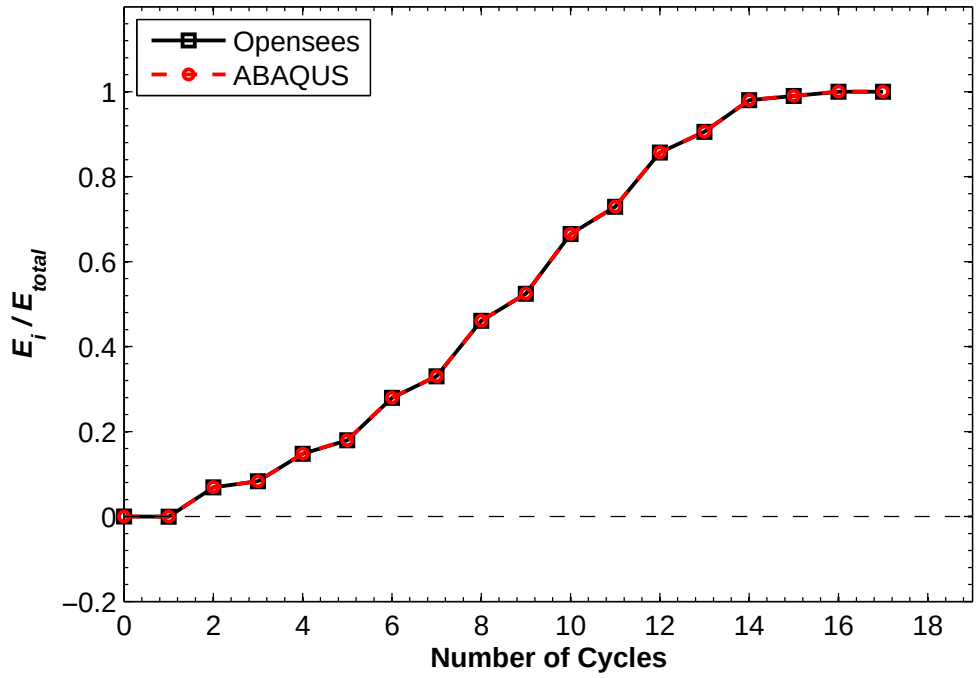

Fig. 5.20. Energy dissipation for strength degradation verification case

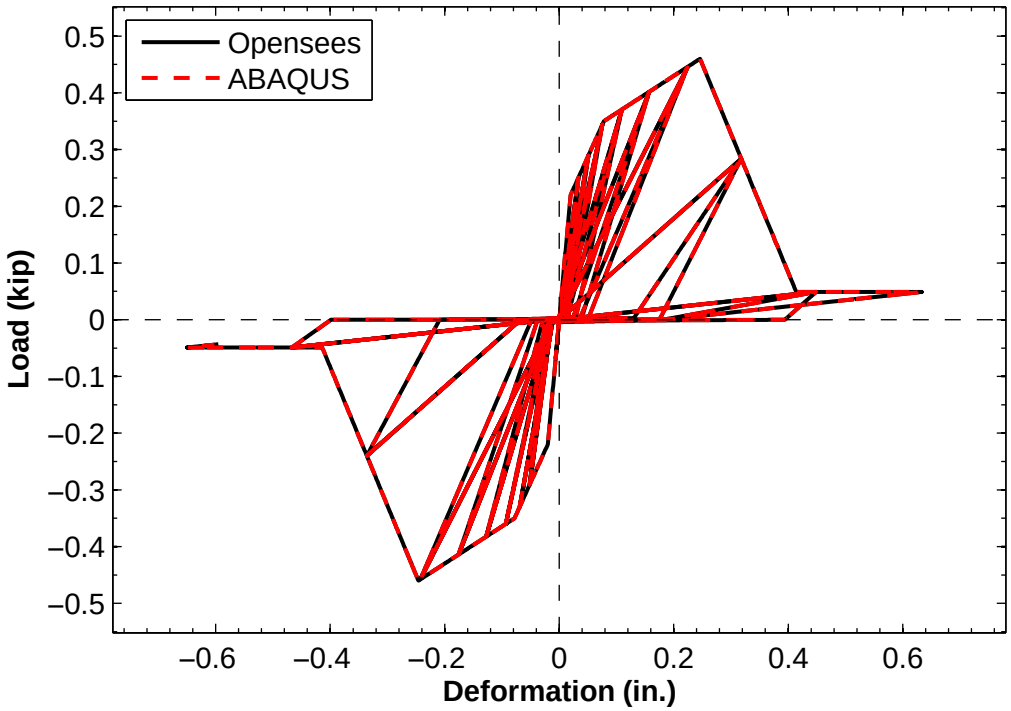

Fig. 5.21. Load-deformation response for unloading stiffness degradation verification case

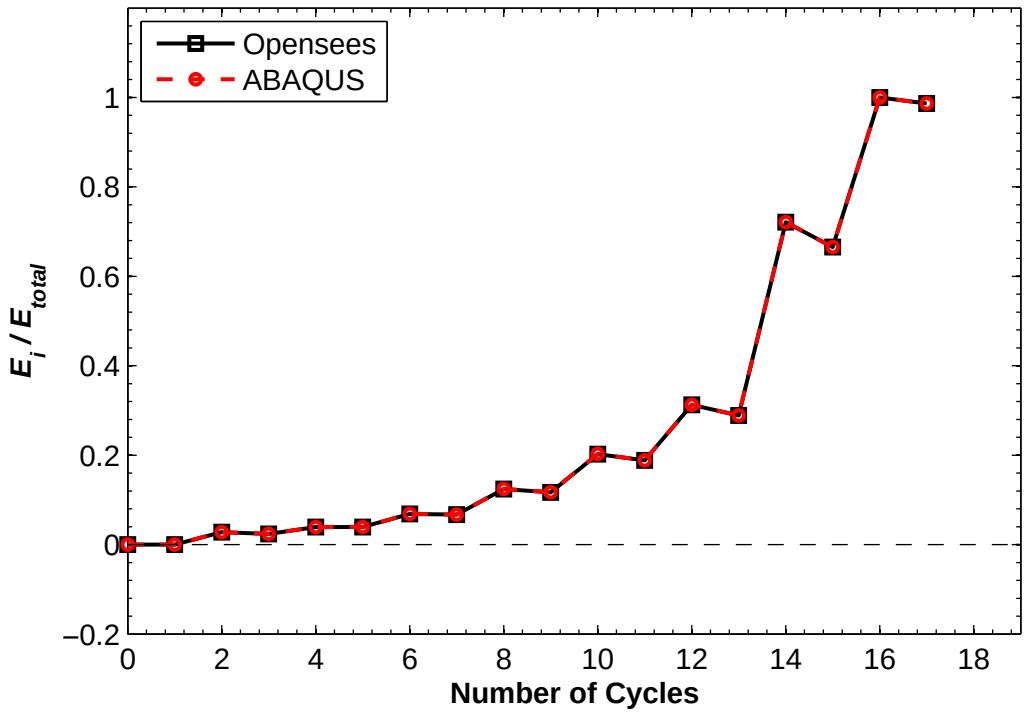

Fig. 5.22. Energy dissipation for unloading stiffness degradation verification case

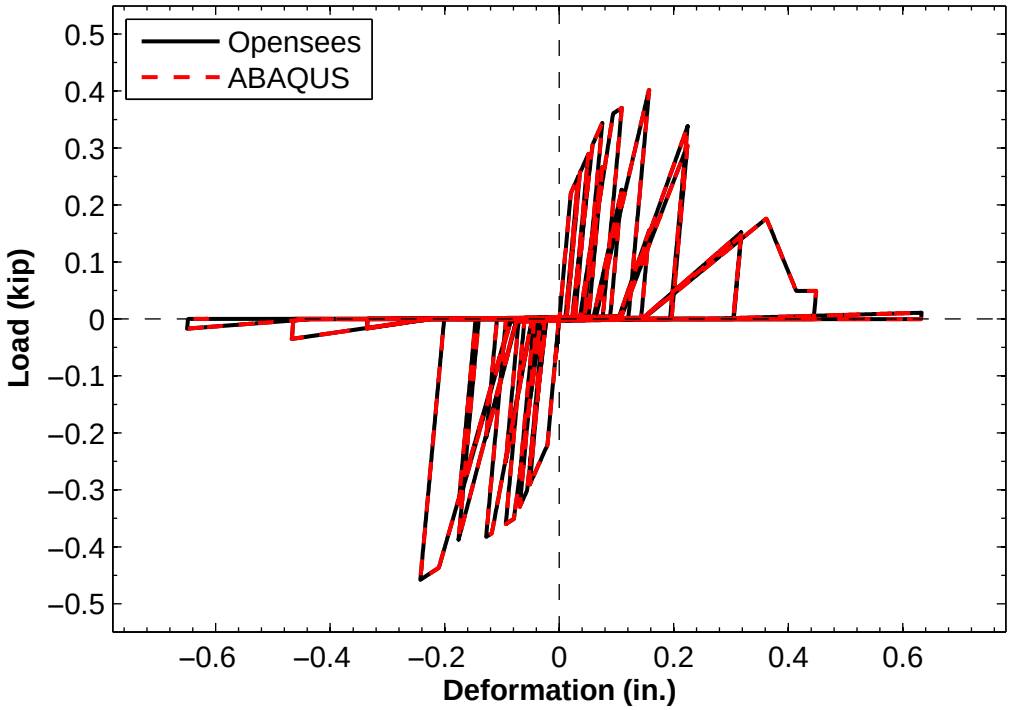

Fig. 5.23. Load deformation response for reloading stiffness degradation verification case

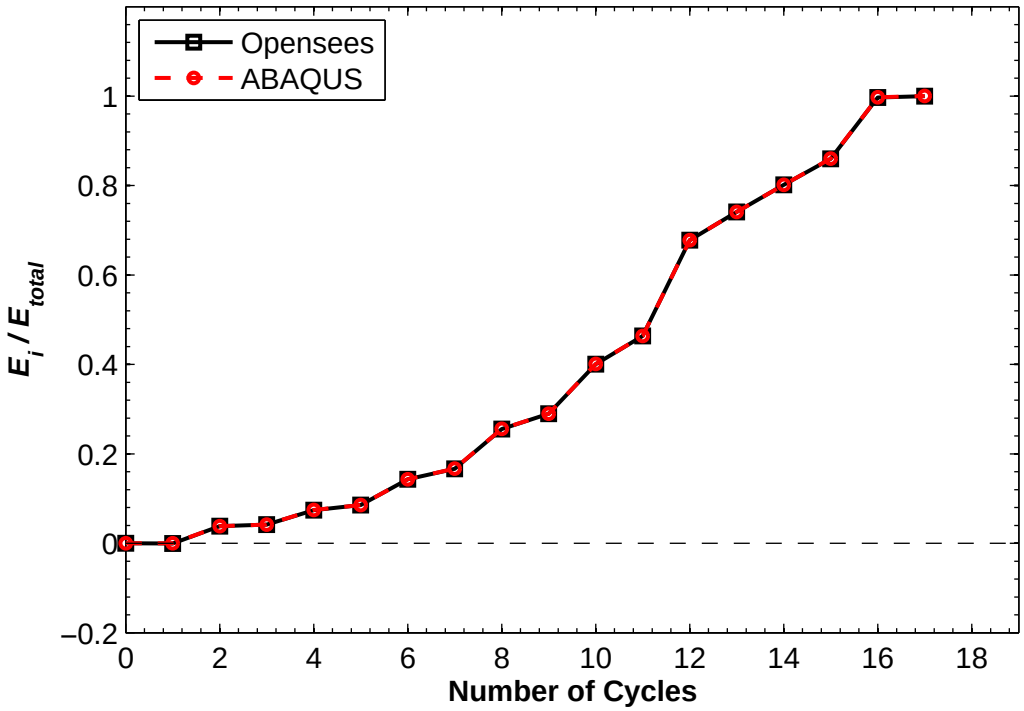

Fig. 5.24. Energy dissipation for reloading stiffness degradation verification case

Chapter 6: Simulation Framework for Cold-Formed Steel Structures

Cold-formed steel structures subjected to extreme loads, like those due to seismic loading, are designed such that lateral loads are resisted by shear wall systems and floor diaphragms. The behavior of these systems is governed by the components individual behavior (e.g., chord studs, floor joists, and sheathing), and their interaction within the system through the connections (e.g. screw-fastened connections). The components and connections can exhibit nonlinear behavior that needs to be considered for performance and analysis based design of CFS framed structures. This chapter introduces a computationally efficient component-based framework for the analysis of cold-formed steel structures that captures the nonlinear behavior in all critical components in detail.

6.1 Simulation framework

The component-based simulation framework is supported by nonlinear models for framing members, screw-fastened connections and other components in light-framed steel structures assembled in finite element models for accurate gravity load analysis, wind analysis, seismic design and other extreme loading conditions. The modeling approach described herein complements the efforts from the CFS-NEES projects to advance analysis and performance based design of cold-formed steel structures described in [15,82] by introducing the nonlinear behavior in the framing members. The framework provides the ability to simulate behavior including limit states related to framing members (e.g., local buckling), single screw-fastened connection limit states and/or sheathing buckling/failure in CFS structures. An outline of the simulation framework for CFS subsystems is illustrated in Fig. 6.1 where the framing members in a sheathed CFS shear wall are modeled using nonlinear-beam columns, and connections between framing members (CFS studs and tracks) and sheathing are modeled using nonlinear hysteretic springs.

The supporting models necessary for the framework are those that govern the behavior of each component, i.e., framing members, sheathing elements, and connections. To model framing elements the approach in Chapter 3 is used to include thin-wall behavior into the analysis of framing members for the three buckling limit states described by AISI-S100-12 [22] (see Fig. 3.1

and 3.4). In Chapter 4 this approach was expanded to provide general expressions and the *asymPinching* model to simulate steel columns including local buckling. A similar approach to the one described in Chapter 4 together with the procedure described in Chapter 3 can be adopted to simulate framing members governed by distortional or global buckling using the *asymPinching* model.

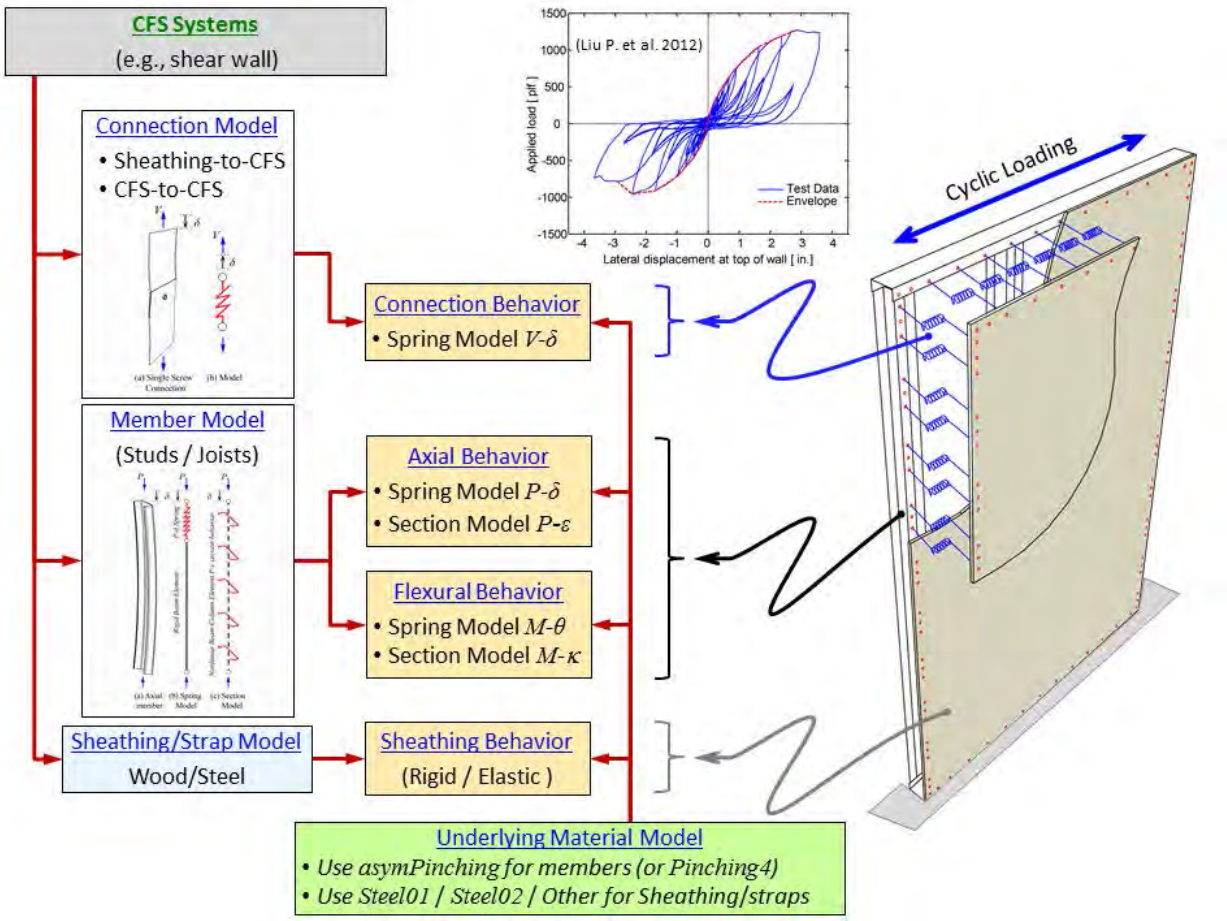

Fig. 6.1. Simulation framework outline for cold-formed steel systems where hysteretic models for members, single screw-fastened connections, and sheathing can be assembled to explore different limit states in CFS shear walls.

Models to simulate the connections between components depend on the type of connection and should provide flexibility to model different types of structural systems. In cold formed steel structures connections between components are usually screw-fastened connections and less commonly welded. Modeling welded connections can be approached in a simplified manner by constraining the appropriate degrees of freedom unless damage of the connection and respective limit states are of interest. In this last case, the proper models need to be provided. In

the case of the most used type of connection in cold-formed steel structures, the screw-fastened connections, a single screw-fastened connection model is suggested. For the proposed framework, single screw-fastened connections are modeled using nonlinear zero length springs with parameters derived from experiments (e.g., [83]). Fig. 6.2 illustrates the spring model with behavior modeled using *Pinching4*. Modeling each fastener involved in a connection can provide the flexibility needed for this type of connection and eases the formulation of a model.

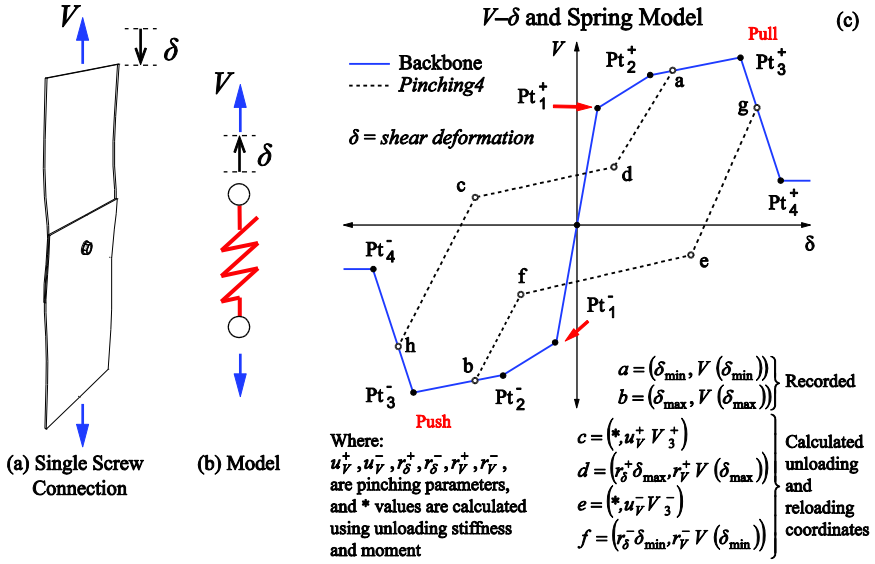

Fig. 6.2. Hysteretic model for single screw-fastened connection.

The next section illustrates the component-based simulation framework applied to the analysis of full scale cold-formed sheathed shear walls and explores the possible limit states pertaining to the framing members. Simulations are compared to responses from full scale tested wood-sheathed shear walls tested at the University of North Texas [12,13].

6.2 Component-based modeling of CFS shear walls [3]

A finite element model for a sheathed CFS shear wall was implemented in OpenSees following the framework depicted in Fig. 6.1. The base model corresponds to a full scale on side wood sheathed CFS shear wall design employed in the CFS-NEES building [19,20] and tested as a single unit at the University of North Texas [12,13]. The wall unit is 2.74m high and 1.22m wide framed using back-to-back 600S162-54 CFS members fastened using two #10 fasteners

[3] This section is a continuation of the work presented in the coauthored conference paper presented at the *2015 SSRC Annual Stability Conference* with the title **"OpenSees Modeling of Wood Sheathed Cold-Formed Steel Framed Shear Walls"** [84].

every 305mm for the chord studs and a single 600S162-54 CFS member 610mm off center between the two chord studs (see Fig. 6.3). Two 600T162-54 CFS tracks at the top and bottom of the wall connect the vertical members together using #10 flat-head fasteners. A wood oriented-strand board (OSB) is fastened to one side of the steel frame using #8 flat-head fasteners spaced every 305mm as shown in Fig. 6.3. A steel strap 38mm wide and 1.438mm thick is used to fasten the OSB to the steel frame at the seam located 305mm from the top of the wall. A ledger 1200T200-97 track that serves to connect the wall to the floor diaphragm is fastened to the vertical members at the top of the wall and on the opposite side of the OSB panel. Vertical wall support is provided by two Simpson Strong-Tie S/HDU6 hold downs connected to the chord studs bottom inward face using #14 hex-head fasteners. Two 15.875mm (5/8in.) bolts connect the bottom track to the bottom of the testing frame.

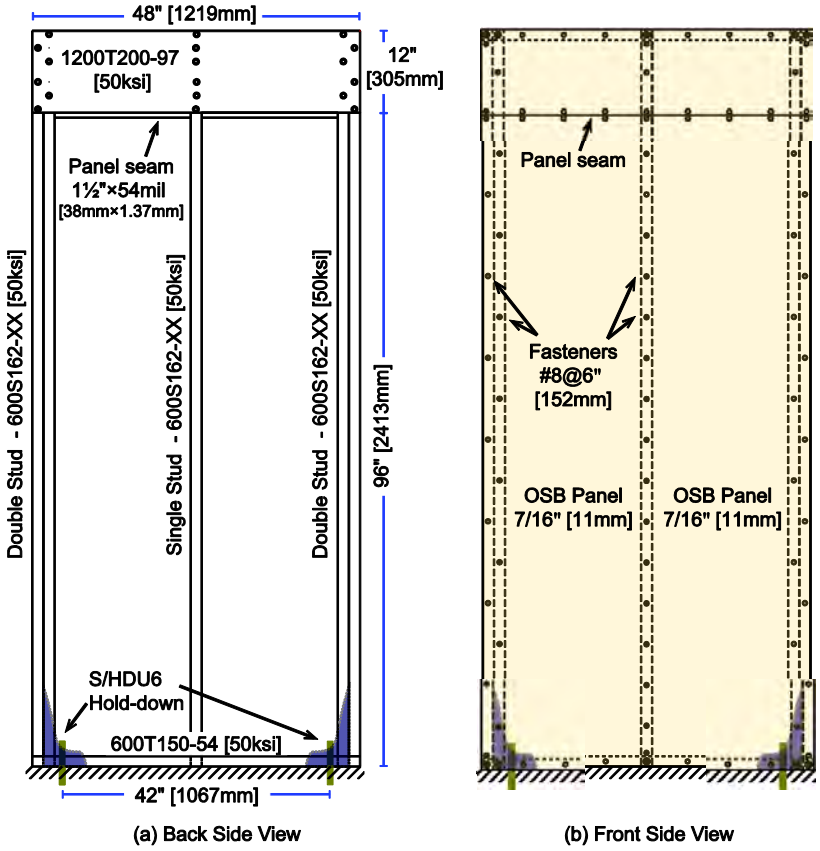

Fig. 6.3. Cold-formed shear wall front and back side detail [12].

6.3 Shear wall numerical model

The base numerical model of the shear wall is implemented herein using OpenSees [24] as illustrated in Fig. 6.4. The model uses *nonlinear beam-columns* elements with cross-section

behavior simulated using *asymPinching* to model the steel framing members, shell elements to model the sheathing panels and zero-length elements with hysteretic behavior using *Pinching4* to model all the screw-fastened connections. In OpenSees the nonlinear beam-columns are implemented using *dispBeamColumn* elements with the Gauss-Lobatto quadrature rule and at least five integration points, two at both ends of the member. A single element is used to model the built-up chord studs at both sides of the wall for simplicity, however the approach is the same if the built-up chord stud needed to be modeled. The fastener connections are implemented using *CoupledZeroLength* elements that allow defining the fastener force-deformation relationship on the plane parallel to the sheathing. The OSB panel is modeled using *ShellMITC4* elements to accommodate any deformations the sheathing can experience. The track-to-vertical framing members connection are modeled for simplicity by constraining the translational degrees of freedom and assuming linear spring with rotational stiffness k =113kN-m/rad based on approximations from measured lateral stiffness of bare frame [12]. Similarly, the translational and rotational degrees of freedom at the ends of the ledger track were constrained to corresponding nodes in the vertical studs. The hold-downs were modeled using elastic *zeroLength* springs with stiffness k=56.7kN/mm in tension while stiffness in compression was set 1000 times larger to simulated the contact with the foundation. Additional springs with large stiffness in compression and close to zero stiffness in tension were provided along the bottom track to simulate contact with the foundation while allowing uplift of the track nodes. Shear anchors were modeled by fixing the horizontal degree of freedom at two of the track nodes next to the hold-downs.

The base model was modified to help illustrate the nonlinear behavior in the vertical framing members and the differences in the failure mechanism due to the development of local buckling on the chord studs. In the modified model the vertical framing members slenderness has been set to a specific value but the rest of the properties (i.e., thickness, area and inertia) have been kept unchanged from the base model. The intention with these modified models is to study the effects of the vertical member slenderness on the response. The influence of the gravity load is included as well as this will trigger the nonlinear behavior in the vertical members and it represents more realistic loading conditions. Table 6.1 and Table 6.2 summarize the modeling scenarios implemented and properties of the framing members used. Properties for single screw-

fastened connection between the OSB panel and steel depicted in Fig. 6.4 are adopted from the work performed by Peterman et al. [83] and are also listed in Table 6.3.

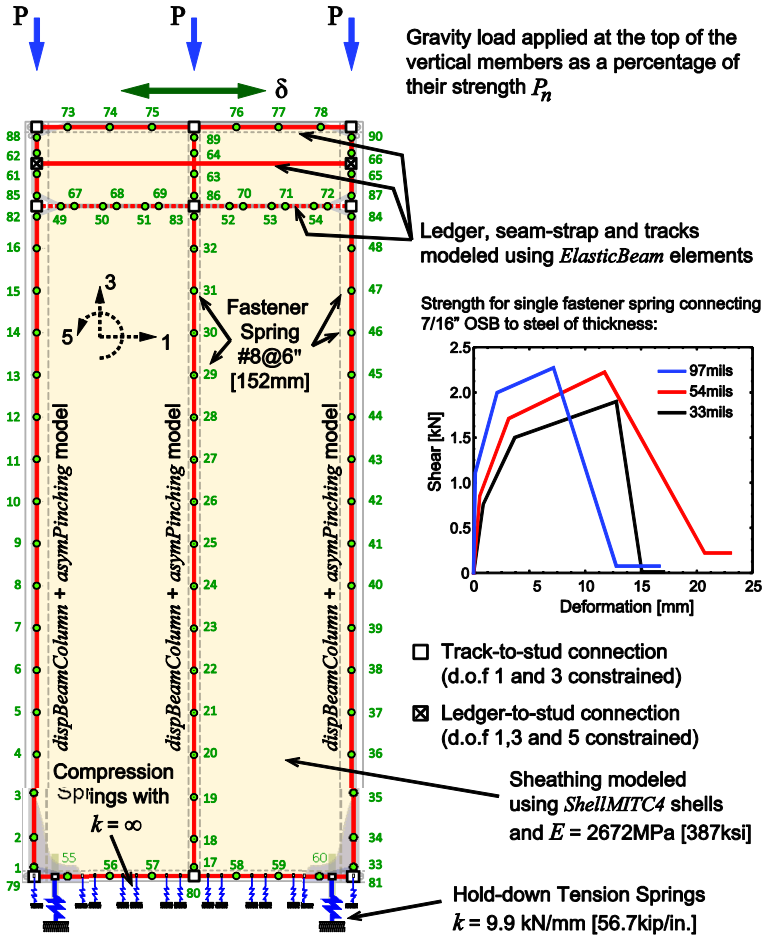

Fig. 6.4. Shear wall model and fastener properties.

Table 6.1. Shear wall model matrix.

Model	Gravity Load P [kN] (a)	Fastener Schedule	Chord Stud (a)	Infill Stud (a)	Stud λ_ℓ	Stud Type	Sheathing
SW1-a	$0.00P_n$= 0.0	#8 @ 152mm	2x54	1x54	1.89	*asymPinching*	7/16" OSB
SW1-b	$0.25P_n$= 16.9	#8 @ 152mm	2x54	1x54	1.89	*asymPinching*	7/16" OSB
SW1-c	$0.50P_n$= 33.8	#8 @ 152mm	2x54	1x54	1.89	*asymPinching*	7/16" OSB
SW1-d	$0.75P_n$= 50.7	#8 @ 152mm	2x54	1x54	1.89	*asymPinching*	7/16" OSB
SW2-a	$0.00P_n$= 0.0	#8 @ 152mm	2x33	1x33	2.51	*asymPinching*	7/16" OSB
SW2-b	$0.25P_n$= 5.6	#8 @ 152mm	2x33	1x33	2.51	*asymPinching*	7/16" OSB
SW2-c	$0.50P_n$= 11.2	#8 @ 152mm	2x33	1x33	2.51	*asymPinching*	7/16" OSB
SW2-d	$0.75P_n$= 16.8	#8 @ 152mm	2x33	1x33	2.51	*asymPinching*	7/16" OSB
SW3	$0.50P_n$= 11.2	#8 @ 152mm	2x33	1x33	2.51	*Elastic*	7/16" OSB
SW4	$0.50P_n$= 11.2	#8 @ 152mm	2x33	1x33	2.51	*Pinching4*	7/16" OSB
SW5-a	$0.50P_n$= 50.6	#8 @ 152mm	L1	L1	1.06	*asymPinching*	7/16" OSB
SW6-a	$0.50P_n$= 41.4	#8 @ 152mm	L2	L2	1.42	*asymPinching*	7/16" OSB
SW7-a	$0.50P_n$= 33.9	#8 @ 152mm	L3	L3	1.89	*asymPinching*	7/16" OSB
SW8-a	$0.50P_n$= 30.8	#8 @ 152mm	L4	L4	2.15	*asymPinching*	7/16" OSB
SW9-a	$0.50P_n$= 27.5	#8 @ 152mm	L5	L5	2.51	*asymPinching*	7/16" OSB
SW5-b	P= 27.5	#8 @ 152mm	L1	L1	1.06	*asymPinching*	7/16" OSB
SW6-b	P= 27.5	#8 @ 152mm	L2	L2	1.42	*asymPinching*	7/16" OSB

SW7-b	*P*= 27.5	#8 @ 152mm	L3	L3	1.89	*asymPinching*	7/16" OSB
SW8-b	*P*= 27.5	#8 @ 152mm	L4	L4	2.15	*asymPinching*	7/16" OSB
SW9-b	*P*= 27.5	#8 @ 152mm	L5	L5	2.51	*asymPinching*	7/16" OSB

(a) See Table 6.2.

Table 6.2. Framing element properties.

Name (a)	SSMA Section	P_y [kN]	A [cm^2]	I_y [cm^4]	I_x [cm^4]	Slenderness λ_ℓ	Predicted Strength [kN]
2x54	600S162-54	250.4	7.26	24.21	243.987	1.89	135.2
1x54	600S162-54	123.7	3.59	7.50	118.959	1.89	67.6
2x33	600S162-33	101.0	4.44	14.55	149.152	2.51	44.9
1x33	600S162-33	50.5	2.22	4.83	74.572	2.51	22.5
L1	-	-	3.59	7.50	118.959	1.06	101.1
L2	-	-	3.59	7.50	118.959	1.42	82.7
L3	-	-	3.59	7.50	118.959	1.89	67.7
L4	-	-	3.59	7.50	118.959	2.15	61.6
L5	-	-	3.59	7.50	118.959	2.51	55.0

(a) 2x indicates a built-up member and 1x indicates a single member

Table 6.3. Fastener backbone and *Pinching4* properties.

Connection	δ_1	δ_2	δ_3	δ_4	V_1	V_2	V_3	V_4	r_δ	r_f	u_f
7/16"OSB-to-97mils	0.152	2.101	7.165	12.789	1.108	1.998	2.274	0.077	0.410	0.010	0.001
7/16"OSB-to-54mils	0.559	3.145	11.740	20.711	0.855	1.710	2.224	0.220	0.420	0.010	0.001
7/16"OSB-to-33mils	0.871	3.701	12.779	15.080	0.760	1.500	1.900	0.012	0.410	0.010	0.001

See Fig. 6.2

6.4 Monotonic and cyclic response of the shear wall base model

The monotonic and cyclic responses of the base model (SW1) are shown in Fig. 6.5 and compared to the experimental response obtained from the full scale tests performed by Liu et.al [12]. Local buckling was included in the vertical members using the *asymPinching* model and properties from Table 6.3 for the 7/16”OSB-to-54mils fastened connection were selected. Gravity loads were not applied at the top of the load. The simulated monotonic and cyclic responses show reasonable agreement to the experimental response including the failure mechanism. The failure mechanism observed in the tests consisted of fastener failure along the bottom and bottom-side edges of the wall which resulted on the sudden drop in strength observed in the curves shown in Fig. 6.5. Some difference exists in the post-peak monotonic response due to the inclusion of the contact springs along the bottom track, however this difference is neglected for the purpose of the study presented in this chapter and the numerical model adopted is considered adequate.

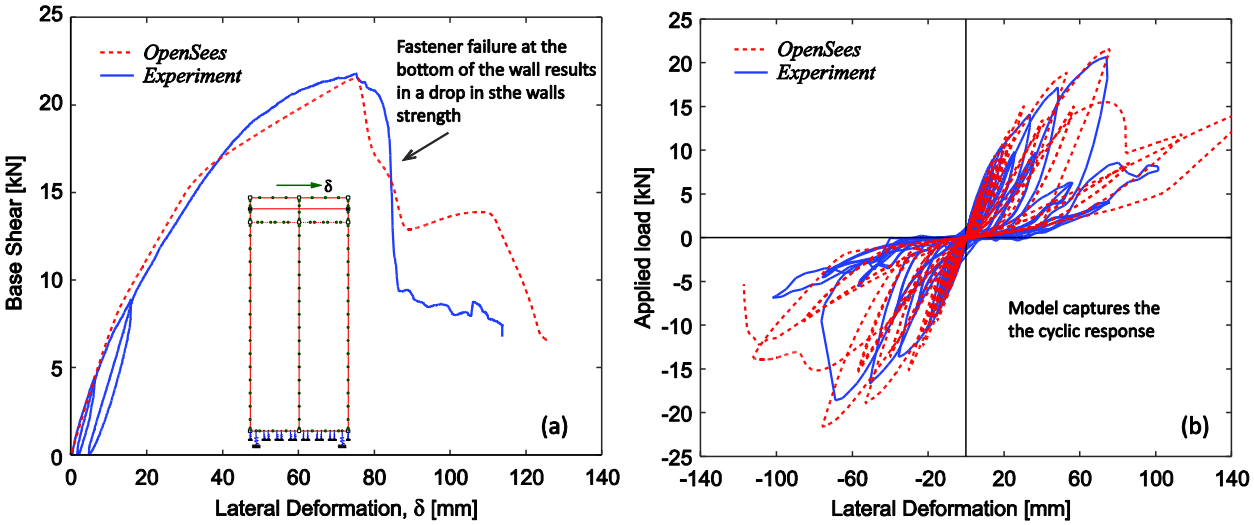

Fig. 6.5. Simulation to experiments comparison shows reasonable agreement between responses.

6.5 Nonlinear stud vs. linear stud behavior effects on the CFS shear wall response

Local buckling in the vertical framing members in walls is commonly addressed as a strength limit state only in design but rarely accounted explicitly during lateral load analysis and in CFS structures. Local buckling can affect greatly the shear wall response and failure mechanism observed in analysis. To illustrate this, responses of a modified version of the shear wall base model subjected to both gravity load and lateral pushover loading are compared. In the modified model the vertical members were replaced with thinner stud (600S162-33) which strength is governed by local buckling. Three approaches for modeling the studs were considered, in the first one (labeled SW3 in Table 6.1) the members are modeled as elastic beam-column elements with axial stiffness k_1 given in Table 4.3. For the second approach (SW2-c in Table 6.1), local buckling in the members was included using the *asymPinching* model. In the third approach (SW4 in Table 6.1) local buckling was included using the alternative equations given in Chapter 4 for the *Pinching4* model. Gravity loading is simulated as point loads applied at the top end of each vertical member and corresponding to 50% of the individual stud strength (i.e., $P = 0.5P_n$).

The pushover responses compared in Fig. 6.6 show clearly that the wall with elastic vertical members can reach higher strength at larger deformation than the wall that includes local buckling in the studs. From Fig. 6.7 and 6.9 the failure mechanism in the wall with elastic framing members is as expected driven by fastener failure along the edges. Moreover, in this wall the compression load developed in the stud to the right increases from an initial value of

0.5P_n to a value twice the predicted single stud strength P_n. This high compressive load occurs before the drop in strength shown in the pushover curve in Fig. 6.6 after which the studs unload considerably (see Fig. 6.7b-g). Conversely, for the wall including local buckling in the studs, the failure mechanism is triggered by local buckling on the compression stud (right) as shown in Fig. 6.8. Most fasteners exhibit low force and deformation demands with most of them remaining on the ascending part of their load deformation response (Fig. 6.10). The axial load in the compression stud is capped at the predicted stud strength which occur slightly before the drop in strength shown in the corresponding pushover curve (Fig. 6.8).

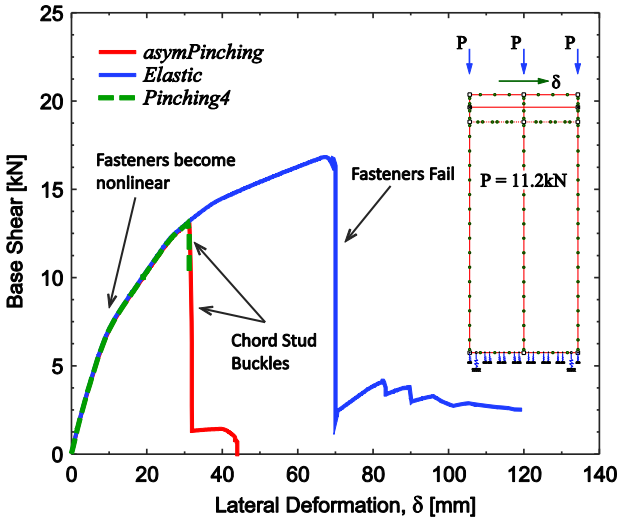

Fig. 6.6. Comparing shear wall with and without including local buckling (SW2-c and SW4). Modeling the chord studs elastic results in overestimation of the wall strength and maximum top displacement.

The main conclusion drawn from this comparison relates to the need to include local buckling when analyzing structural systems with thin walled members such that all possible design limit states are considered. Recalling the response for the base model (no gravity load) in Fig. 6.5, the vertical members were modeled including local buckling but they remained elastic with loads below their predicted strength, and the failure mechanism was fastener controlled like in the test. Using elastic beam column in the base model would yield the same response as if local buckling in the studs is considered. However, a small but significant modification such as changing the thickness of the vertical members can trigger a different failure mechanism, and reduce the wall strength and ductility. This difference can go unnoticed if the nonlinear behavior is not included.

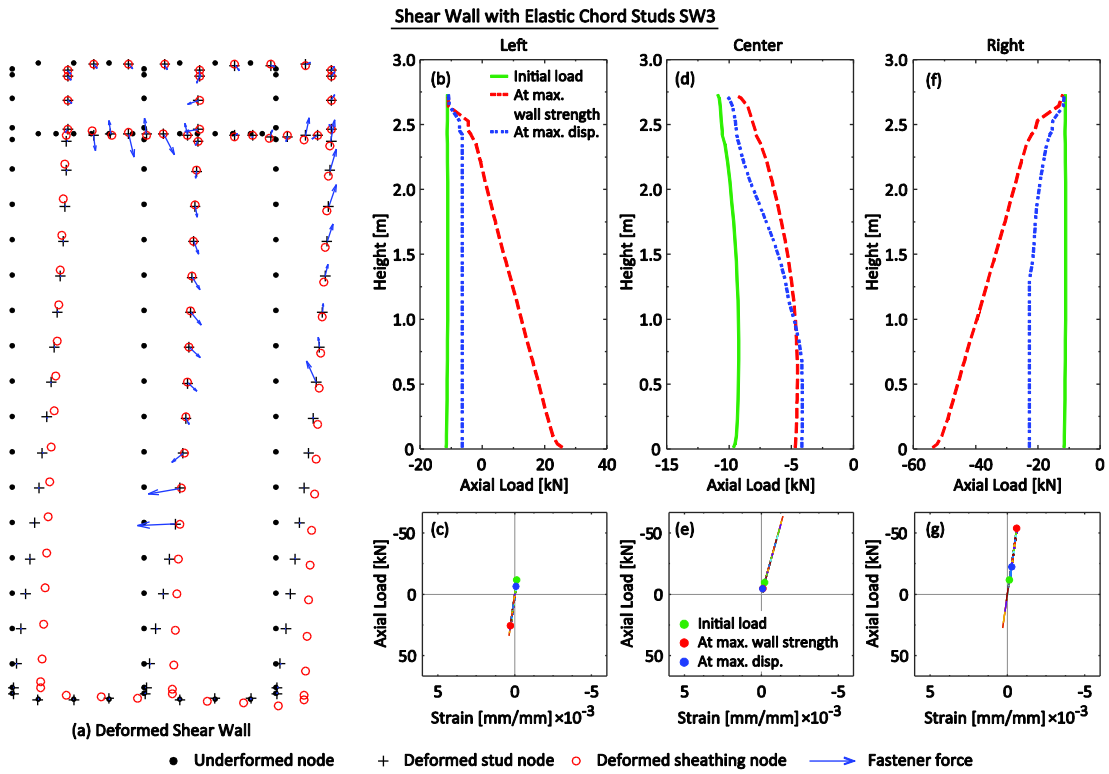

Fig. 6.7. Shear wall (SW3) deformed shape (a) showing the wall failure mechanism triggered by failure of the bottom fasteners, while the studs remain elastic even though $P > P_n$ on the right chord stud (f, g).

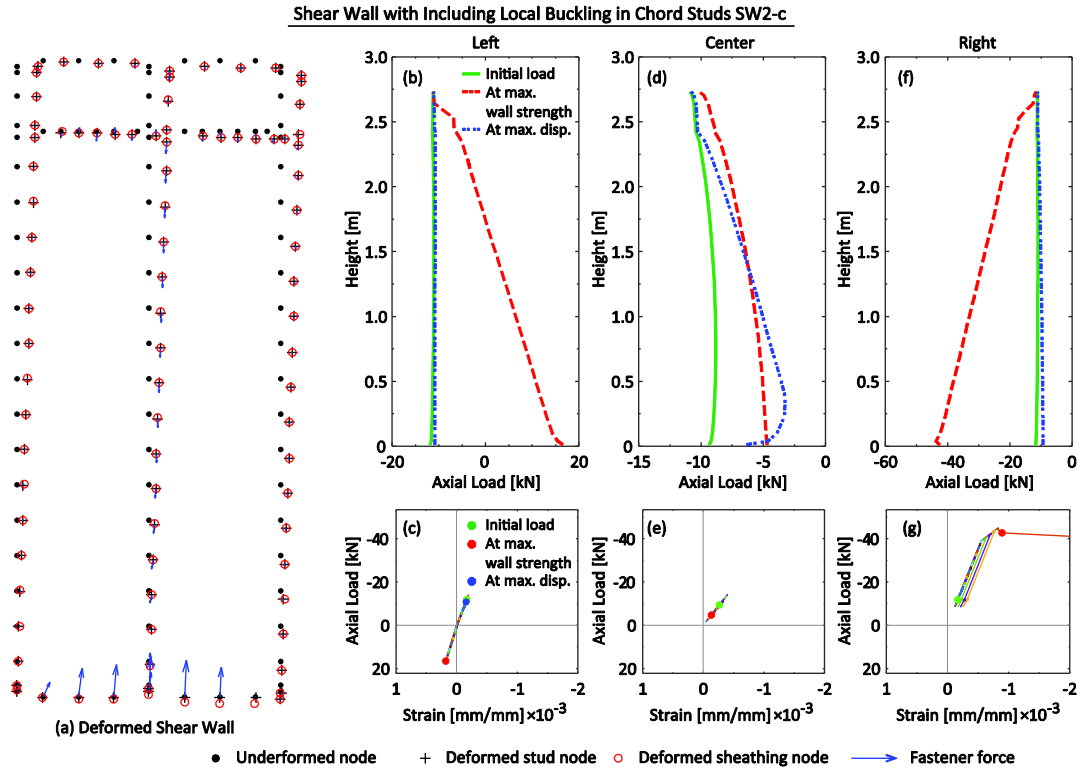

Fig. 6.8. Shear wall (SW2-c) deformed shape (a) showing the wall failure mechanism triggered by buckling of the compression chord stud, while fasteners exhibit low load and deformation demands.

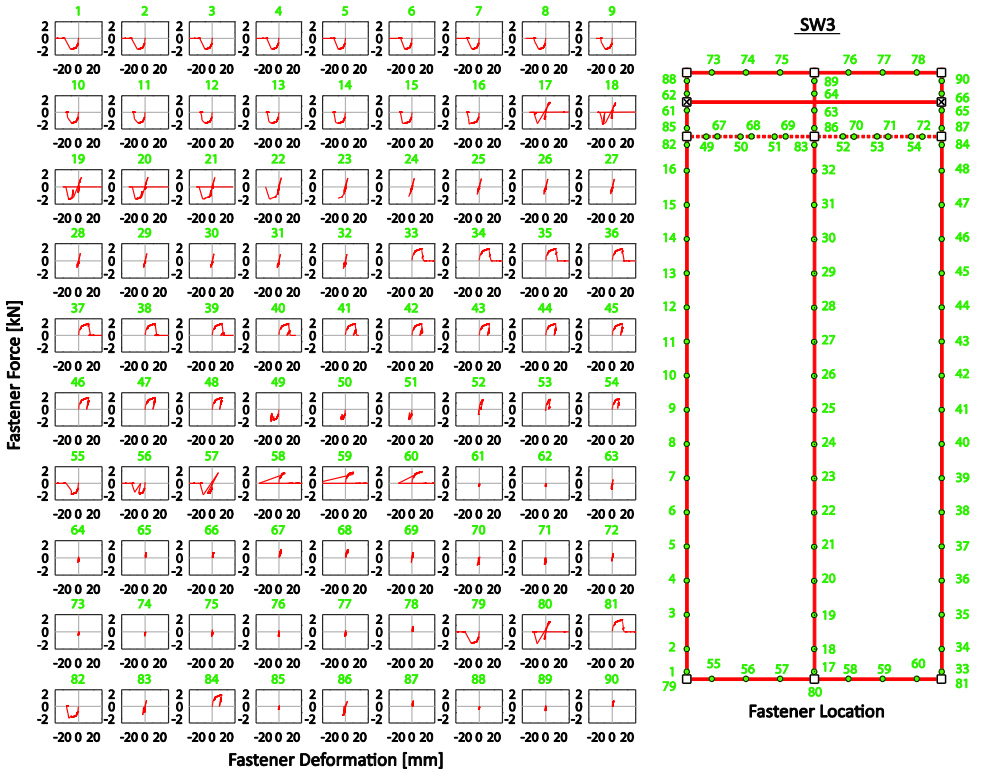

Fig. 6.9. Fastener load-deformation responses in shear wall with elastic chord studs (SW3) show the bottom fasteners along the sides failing that results on the wall's loss of strength.

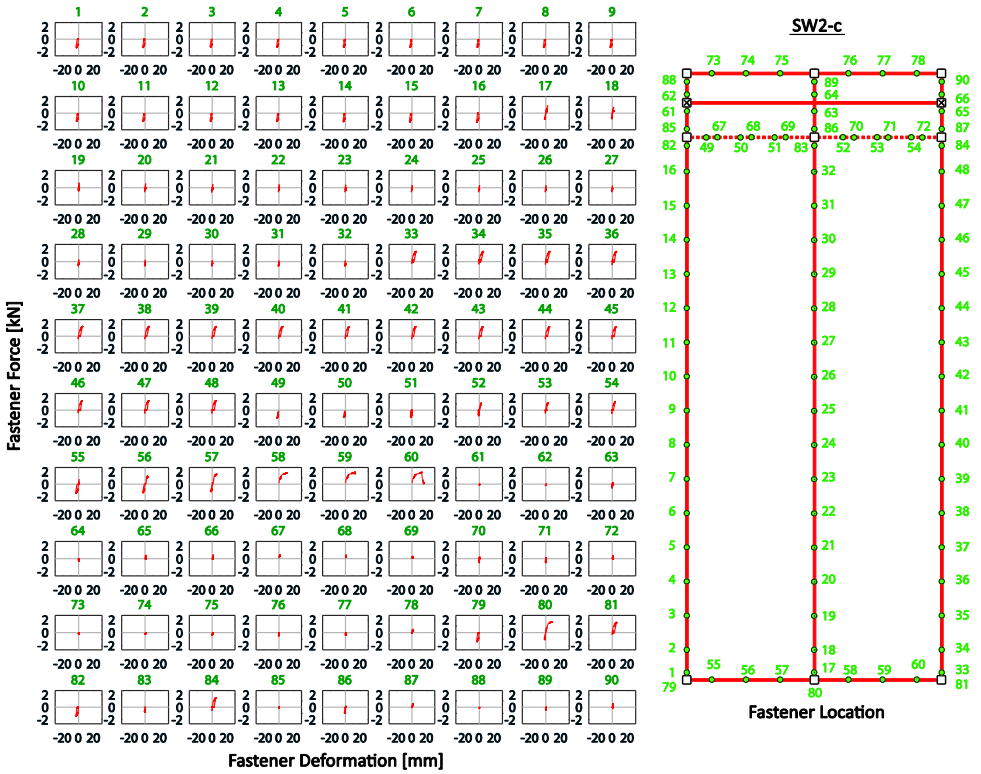

Fig. 6.10. Fastener load-deformation responses in shear wall with nonlinear studs (SW2-c) where fastener exhibit force and deformations below their prescribed strength.

6.6 Gravity load effects on the CFS shear wall response

Gravity load effects on the shear wall monotonic response were explored for two different shear wall configurations listed in Table 6.1 as SW1 and SW2. The first wall model corresponds to the base model and the second is the modified version of the base model with thinner vertical studs (600S162-33). Gravity loading was simulated as point loads applied at the top end of each vertical member and corresponding to a percentage of the individual stud strength (i.e., $P = 0.25P_n$, $0.5P_n$ and $0.75P_n$).

The gravity load influence on the shear wall response is of interest since its effects added to the vertical forces developed in the studs due to lateral loads can trigger sooner local buckling and change the failure mechanism. For instance, in the case of the shear wall base model (SW1) when the gravity load is increased, an expected reduction on the maximum strength is observed as well as decrement on the wall deformation at which point softening of the response occurs (see Fig. 6.11a). However, for the higher gravity load values (0.5 and 0.75) the failure mechanism involves some amount of local buckling developed in the infill stud after the fasteners on the compression side edge had failed. The influence of local buckling in the described case is small and plays a roll only after the fasteners have failed and for gravity loads close to the strength of the vertical members.

In the case of the shear wall with thinner studs (SW2), the effects of the gravity load is more pronounced. Local buckling affects the failure mechanism even for the low gravity load case ($0.25P_n$) where the fastener failure along the right edge and buckling at the bottom of the right stud happens almost simultaneously (see Fig. 6.12 and 6.13). Because the stud can still carry load the wall response shows a lower plateau (see Fig. 6.11b) where more fasteners fails until either buckling of the stud happens (e.g., case of $0.5P_n$) or all fastener have failed. As the gravity load applied is increased local buckling governs the failure mechanism and fasteners remain at low deformations and force demands and the post-peak plateau is not developed.

An additional effect observed of the gravity loads on the shear wall lateral response is an increase of the initial stiffness of the wall. For instance, in shear walls where the failure mechanism is mainly driven by fastener failure like in the base model case (SW1), the initial lateral stiffness of the wall increases about 50% as shown in Fig. 6.11a. There is a similar increase on the initial stiffness as well (25% to 48%) in the case of the shear wall SW2 where local buckling is driving the failure mechanism (Fig. 6.11b). This increase of the initial stiffness

for example was not captured in the shear wall test described in [12] as gravity load was not applied. While other few studies (e.g., [3]) have considered gravity load effects on the lateral response of CFS shear walls, the amount of testing needed to evaluate the effects of gravity load in a reliable way would be expensive. In this case, having the capability offered by the proposed analysis framework including the nonlinear behavior of the framing members would be of benefit.

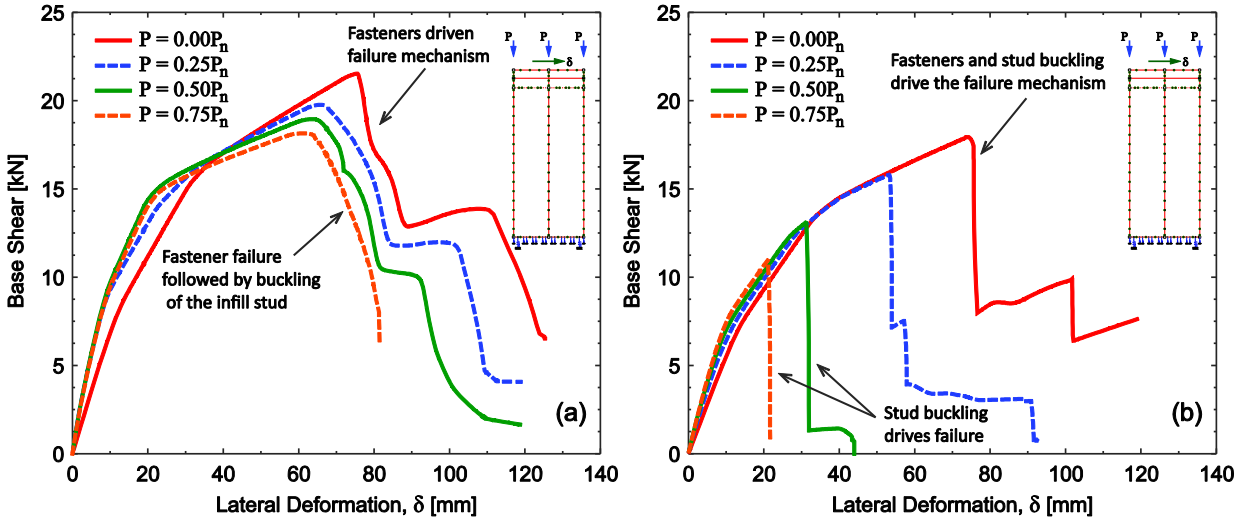

Fig. 6.11. Effects of gravity load on the shear wall lateral force-deformation response for (a) the base model SW1, and (b) the modified shear wall with thinner vertical members SW2.

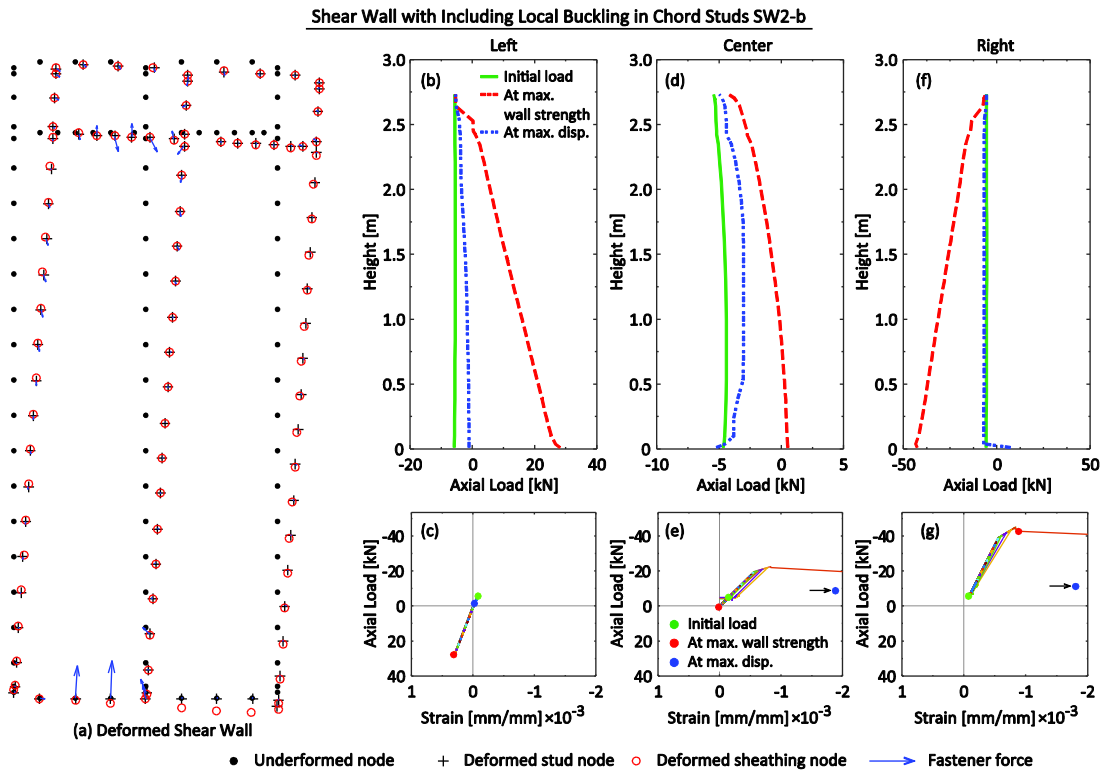

Fig. 6.12. Shear wall (SW2-b) deformed shape (a) showing fastener failure and local buckling and in the compression chord stud happening almost simultaneously when the wall reaching its maximum strength.

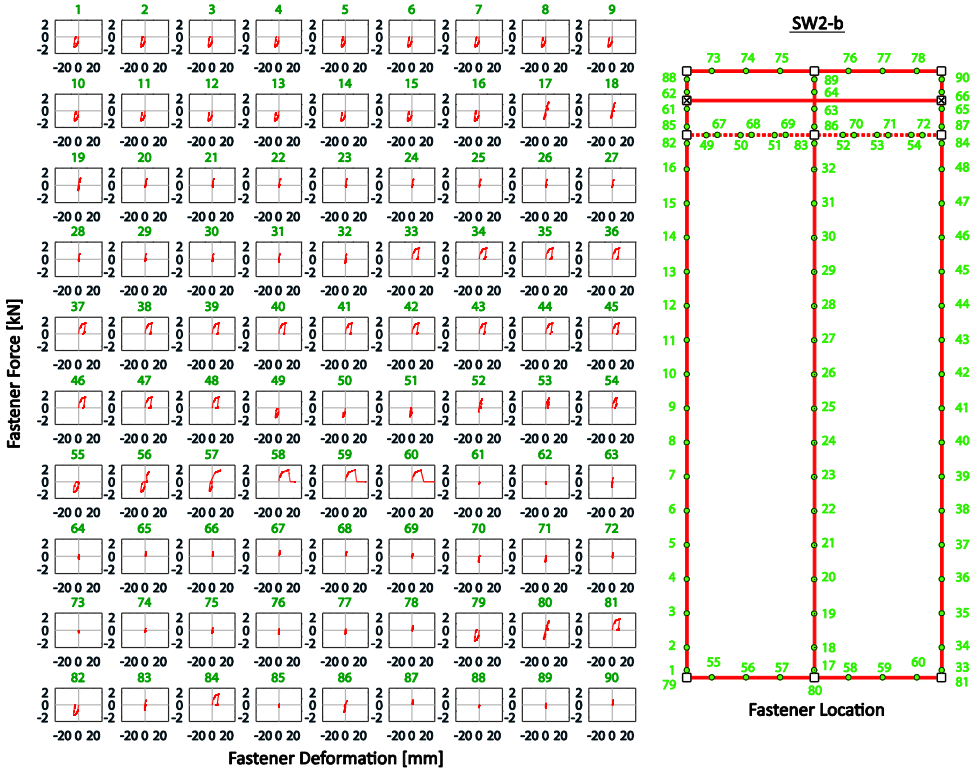

Fig. 6.13. Fastener load-deformation responses in shear wall SW2-b where fasteners failure and local buckling of the compression chord stud happen almost simultaneously.

6.7 Member slenderness effects on the CFS shear wall response

To evaluate the sensitivity of the shear wall response to the vertical member cross-section slenderness λ_ℓ. The vertical member cross-section slenderness is set to five different values in the interval 1.0 to 2.5 while keeping the remaining properties (i.e., thickness, area and inertia) unchanged from the base model SW1. The *asymPinching* model is used to model the cross-section behavior including local buckling. Because the thickness of the members is kept constant the properties for the fastened connection are the same as those in the base model SW1. Two gravity loading scenarios are considered, in the first one (SW5-a to SW9-a) the applied load corresponds to a 50% of the predicted stud strength P_n, while in the second scenario (SW5-b to SW8-b) the applied load is the same, P = 27.5kN, for all shear walls modeled. This last value of axial load corresponds to the 50% of the predicted strength P_n of the more slender stud considered in this example, i.e., members in wall SW9-a (see Table 6.1).

The monotonic responses for the first gravity load scenario (P =0.5P_n) in Fig. 6.14a show that the failure mechanism is triggered by local buckling of the compression chord stud except in wall SW5-a. For this wall failure is fastener driven where the studs remain practically elastic (see Fig. 6.15) resulting in smooth softening branch of the response. The axial load developed in the studs from lateral loading added to the 0.5P_n initial load takes the studs beyond the deformation corresponding to the peak strength, e.g., see Fig. 6.16 and 6.17. This reflects as discussed previously in the abrupt drop in wall strength of the wall shown in the pushover curves in Fig. 8.13a. Development of a plateau after the peak strength for the first gravity loading scenario is not possible for walls SW6-a to SW9-a because of the buckled compression chord.

In the second gravity loading scenario, the pushover responses of the walls show similar behavior to the previous case where buckling of the compression chord stud leads to an abrupt drop in the wall strength (see Fig. 6.14b). However, because the initial load in this scenario is set to be the same for all walls and smaller than 0.5P_n, each wall can sustain much larger deformations compared to the first gravity loading scenario. For example, the deformation at peak load for the SW7-b wall is 40mm, 70% more than the deformation at peak (24mm) experienced by wall SW7-a. Failure of the wall is triggered when the total axial load acting compression chord stud reaches P_n and buckling occurs. In the case of walls SW5-b and SW6-b, the response is almost identical because the initial gravity load is small enough that the studs in both cases remain practically elastic and wall failure is fastener driven. In two of the wall

analyzed (SW7-b and SW8-b) a post-peak increase in strength is observed that corresponds to fasteners reloading after they first unloaded when buckling of the stud occurred.

Summarizing, the effects of slenderness are more noticeable as the initial gravity load acting on the wall increases such that added to the axial loads developed from lateral loading get closer to the vertical member strength. In this case the failure mechanism changes from the smooth fastener driven mechanism to a more abrupt failure mechanism triggered by local buckling of the studs.

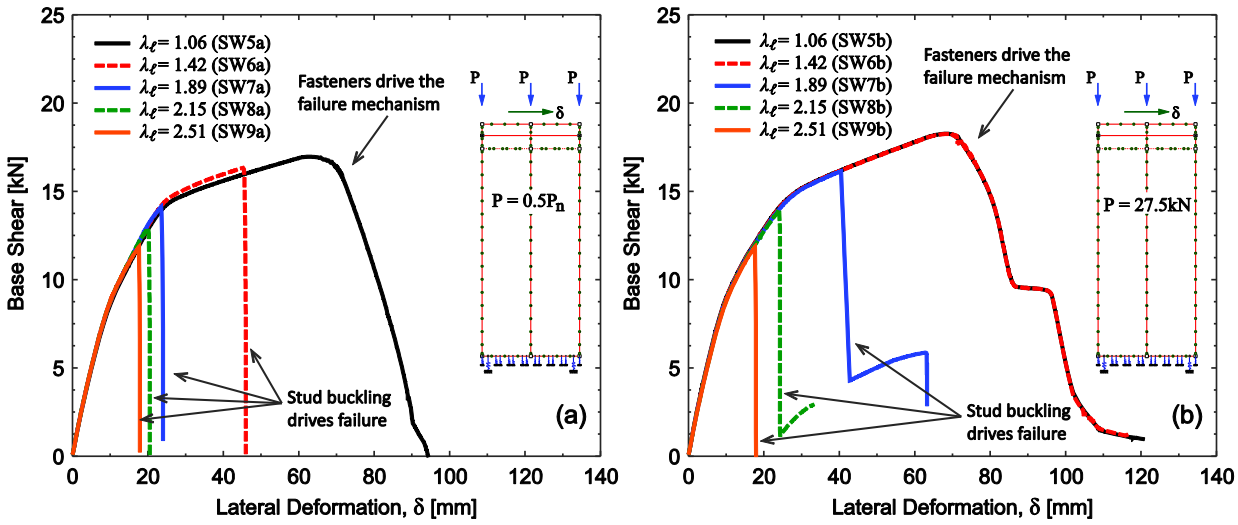

Fig. 6.14. Shear wall response sensitivity to the vertical member cross-section slenderness.

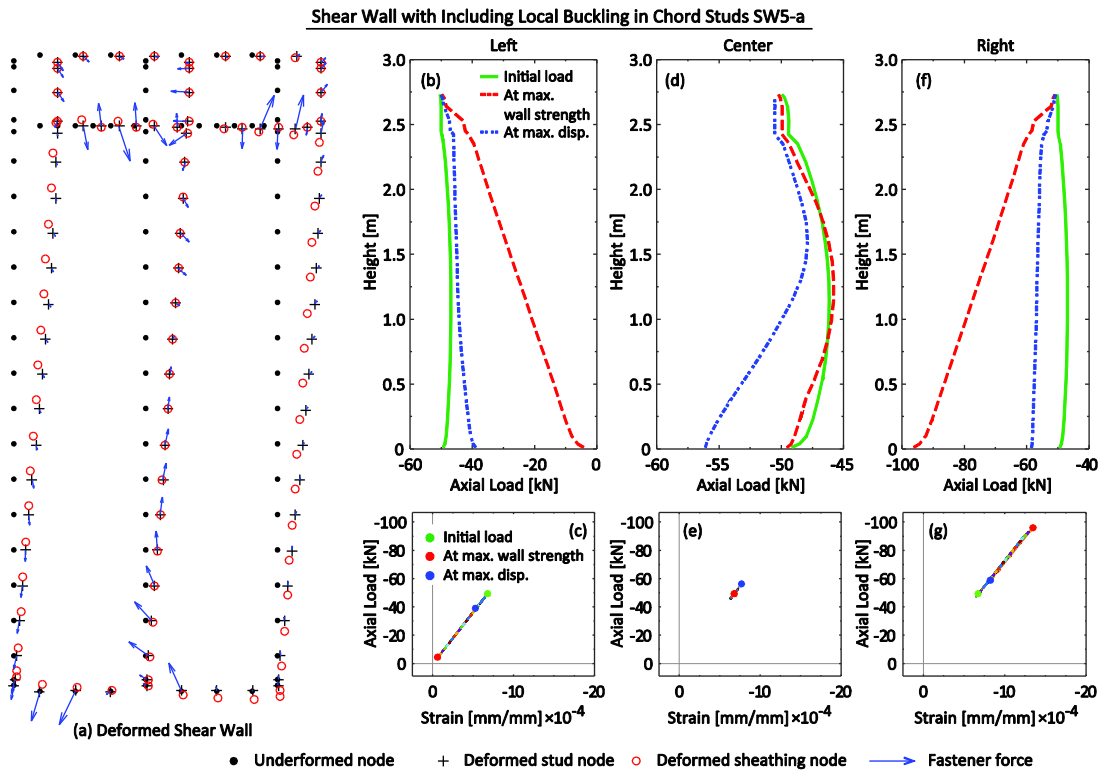

Fig. 6.15. Shear wall (SW5-a) deformed shape (a) showing fastener failure along the edges and studs remain elastic and always in compression.

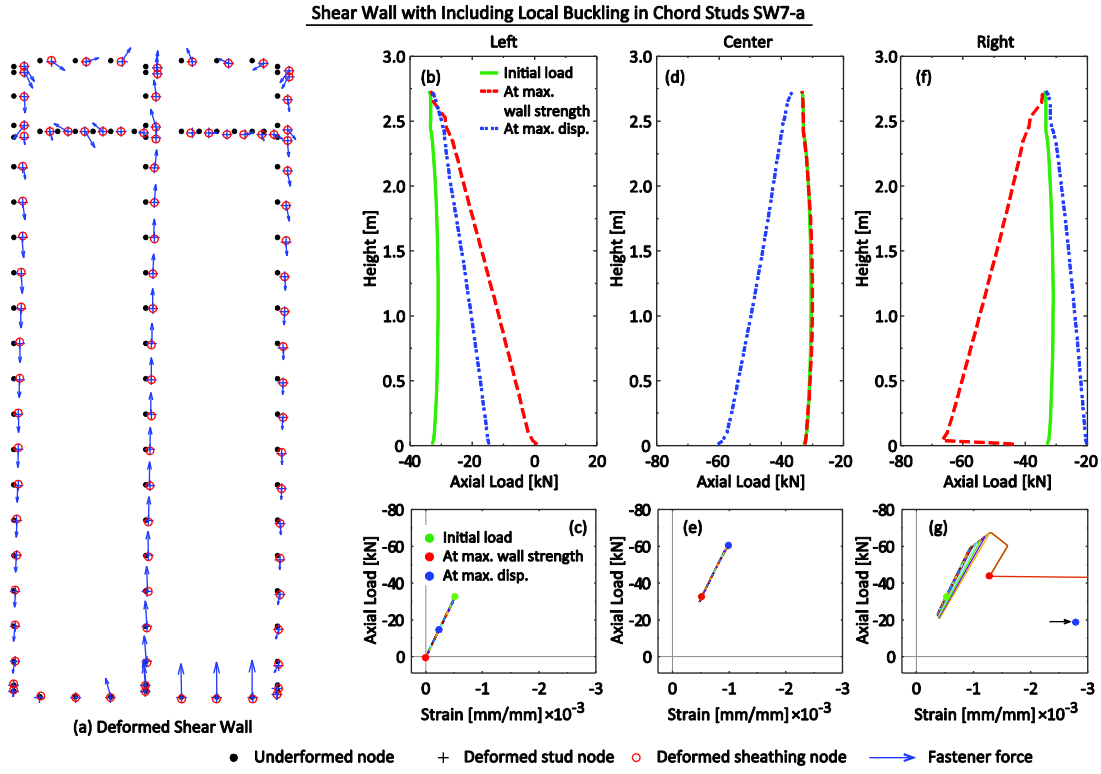

Fig. 6.16. Shear wall (SW7-a) deformed shape (a) showing the wall failure mechanism triggered by local

buckling of the compression chord stud, while fasteners have low load and deformation demands.

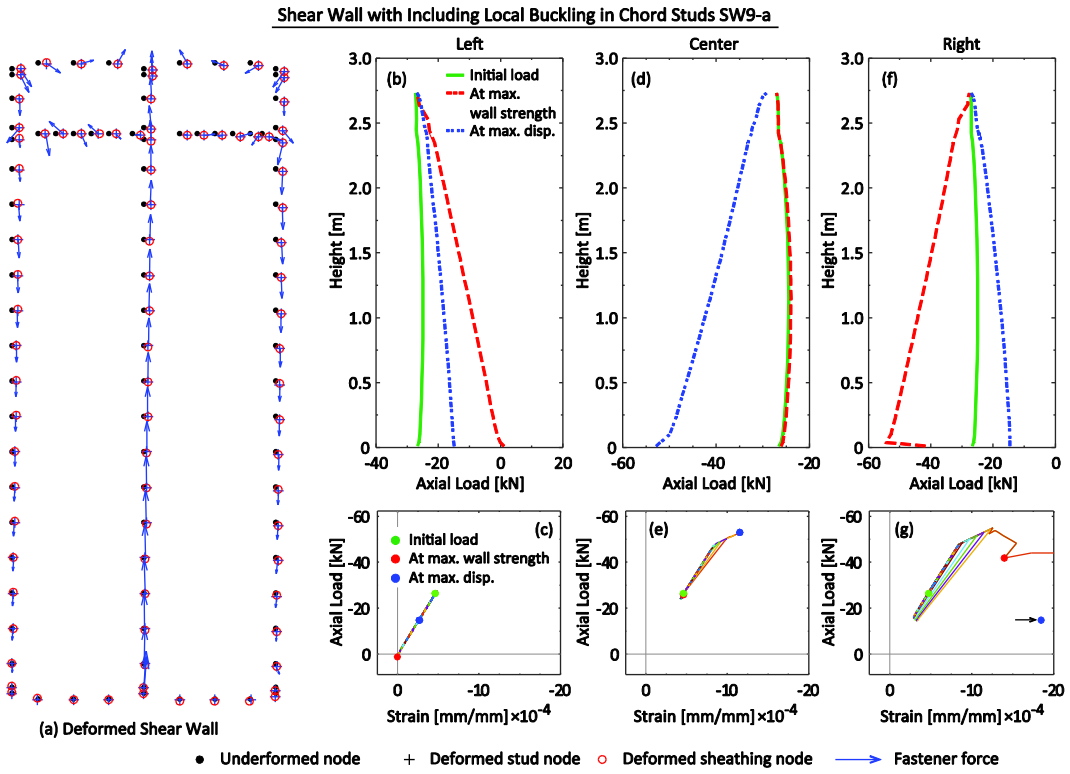

Fig. 6.17. Shear wall (SW9-a) deformed shape (a) showing the wall failure mechanism triggered by local buckling of the compression chord stud followed by buckling in the infill stud.

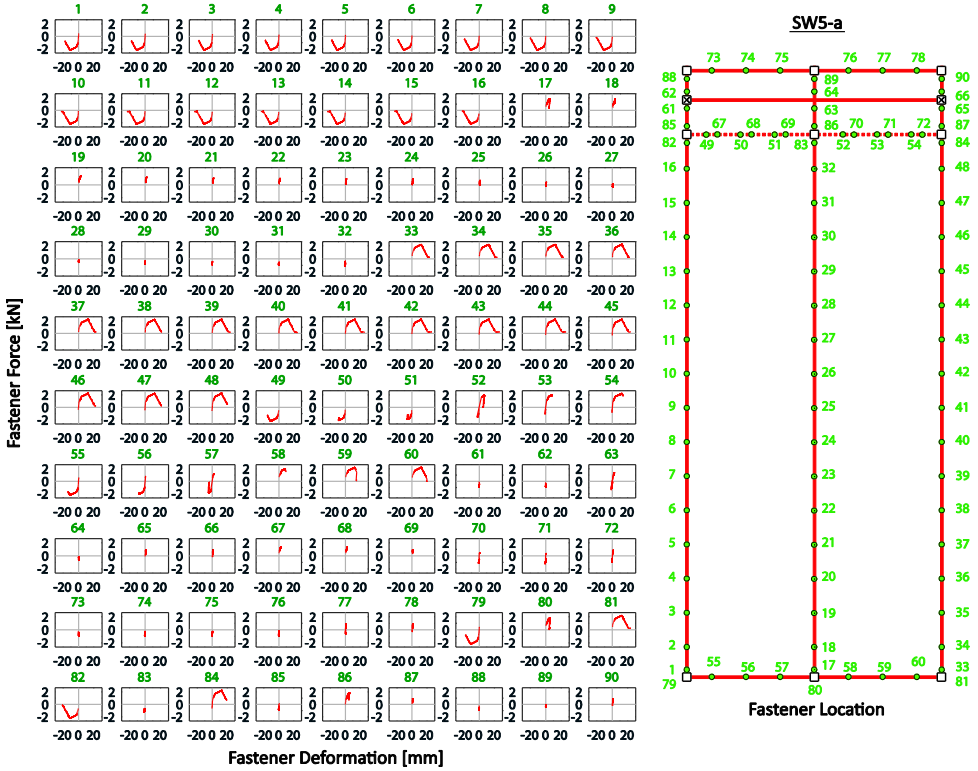

Fig. 6.18. Fastener load-deformation responses in shear wall with less slender studs (SW5-a) where

bottom fasteners along the sides fail, while the studs remain elastic.

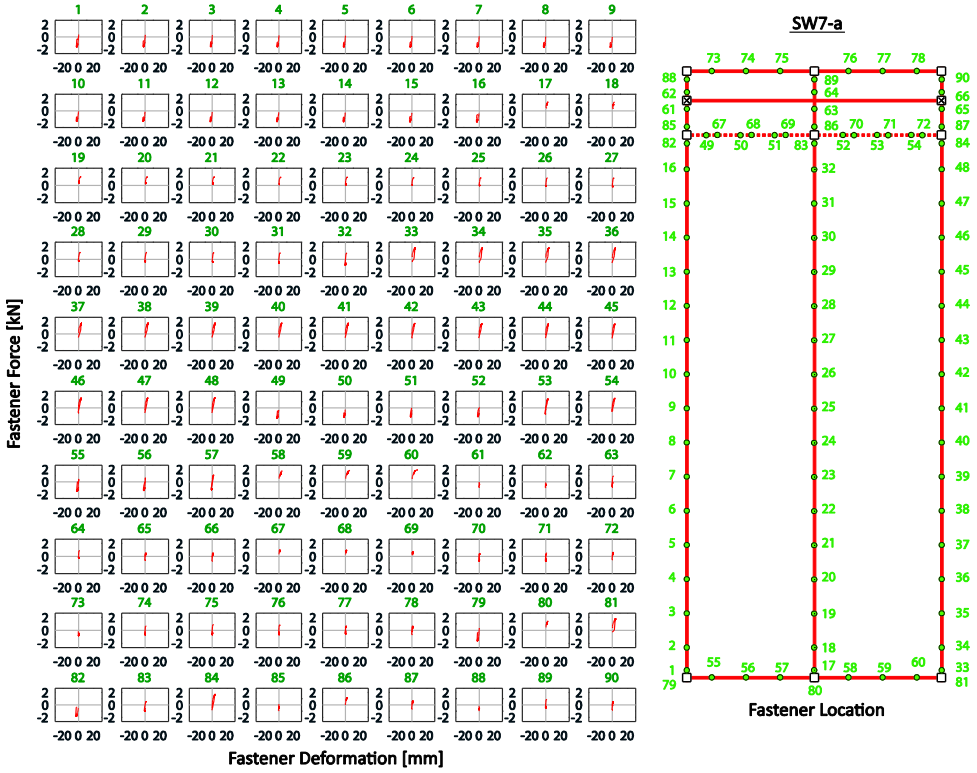

Fig. 6.19. Fastener load-deformation responses in shear wall (SW7-a) where failure is triggered by buckling in the compression chord stud while the other vertical members remain elastic.

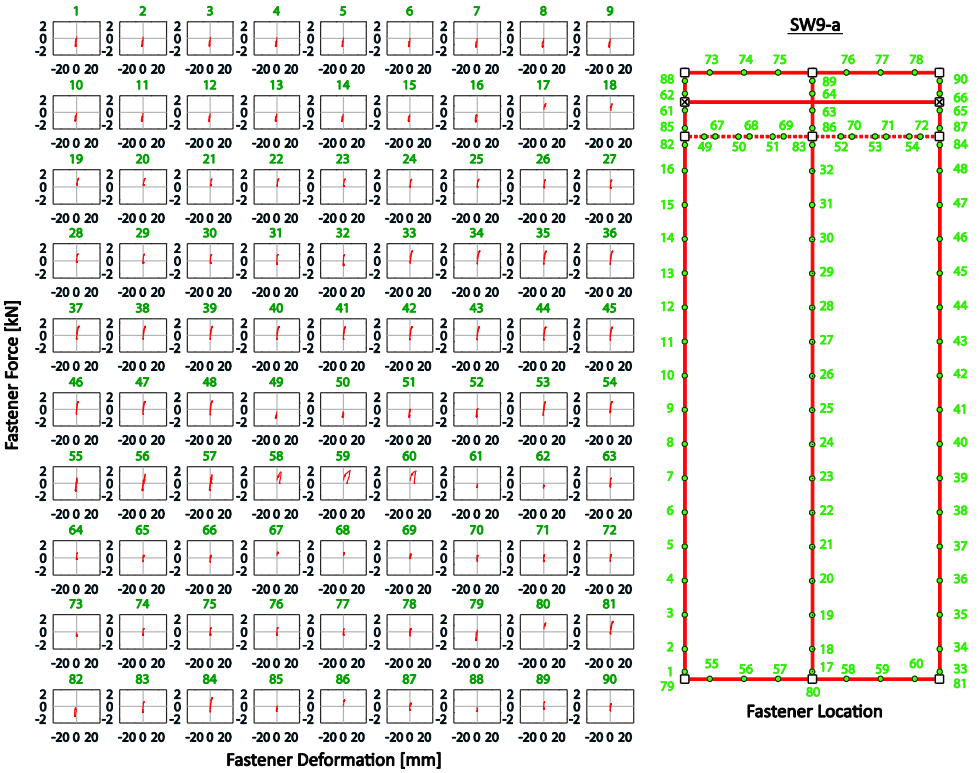

Fig. 6.20. Fastener load-deformation responses in shear wall with slender studs (SW9-a) where failure is triggered by buckling in the compression stud and infill stud reaches loads close to its strength P_n.

6.8 Shear wall cyclic response

Shear wall cyclic responses were obtained to investigate the influence of gravity load and sensitivity to the vertical member cross-section slenderness λ_ℓ. The resulting responses exhibit similar characteristics to the pushover responses previously described. Thus, increasing initial gravity loading acting on the wall reflects in a decrement of the cyclic envelope and increase of the initial lateral stiffness similar to that observed from the pushover responses, see Fig. 6.21a. The failure mechanism exhibited depends as well on the slenderness and magnitude of the applied initial gravity loads. Fig. 6.22 shows the typical response for a wall (SW1-c) where the failure mechanism is fastener driven, and the forces in the vertical studs remain elastic. Fig. 6.23 shows each fastener force-deformation response for the same wall (SW1-c) where it is seen the edge fasteners are the first ones to fail.

For the case of changing the vertical member cross-section slenderness effects, the responses also exhibit the same type of behavior than the corresponding pushover responses, see Fig. 6.21b. The failure mechanism is as well similar to the one observed for the pushover

analysis, and it varies from fastener driven to chord stud buckling triggered depending on the vertical members slenderness. For example Fig. 6.24 shows the response for wall SW7-b, where akin its monotonic response shows buckling in the chord studs. In this case most fasteners connecting the lower OSB panel experience force demands close to the fastener maximum strength, see Fig. 6.25.

In all cyclic responses obtained, vertical members do not experience large nonlinear cycles and therefore cyclic strength and stiffness degradation in this members and their effect on the overall shear wall response is minimal. This result is a consequence of the specific nature of the structural system analyzed where chord stud buckling immediately renders instability. If the analysis were included for example in the context of a whole building analysis where the wall were connected to other elements and redistribution is possible, then more dissipation from the chord studs could be expected. Additionally, the parameters used in this study to define the fastener behavior model do not include strength and/or stiffness cyclic degradation. It is expected that including these two phenomena would result in additional degradation especially for those walls where the failure mechanism is fastener driven.

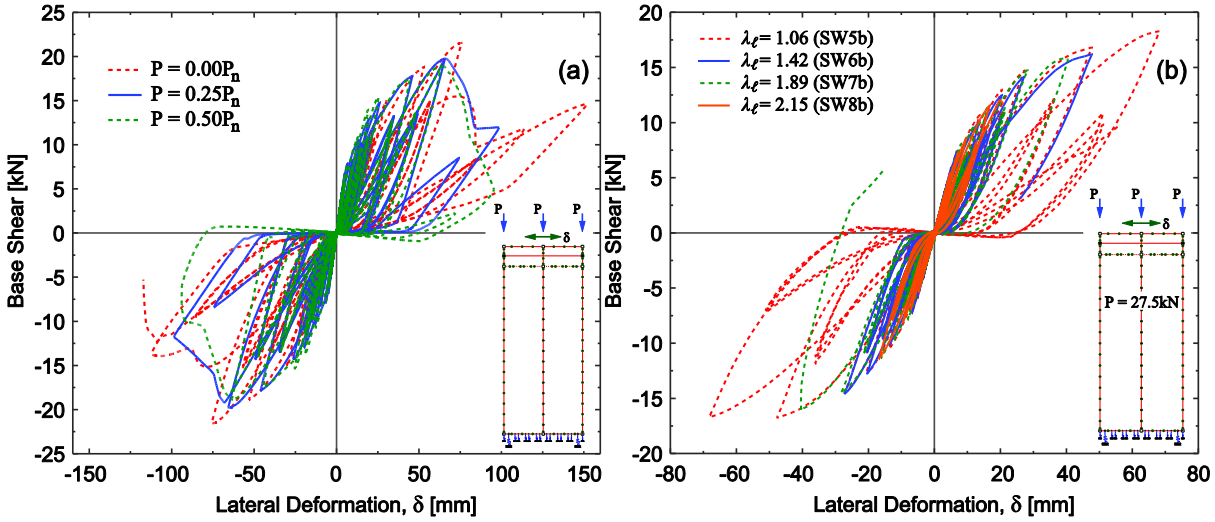

Fig. 6.21. Cyclic response for the shear wall SW1 (a) shows the reduction on the strength envelope because of increasing initial gravity loads, and (b) shows the shear wall response sensitivity to the vertical member cross-section slenderness (SW5b-9b).

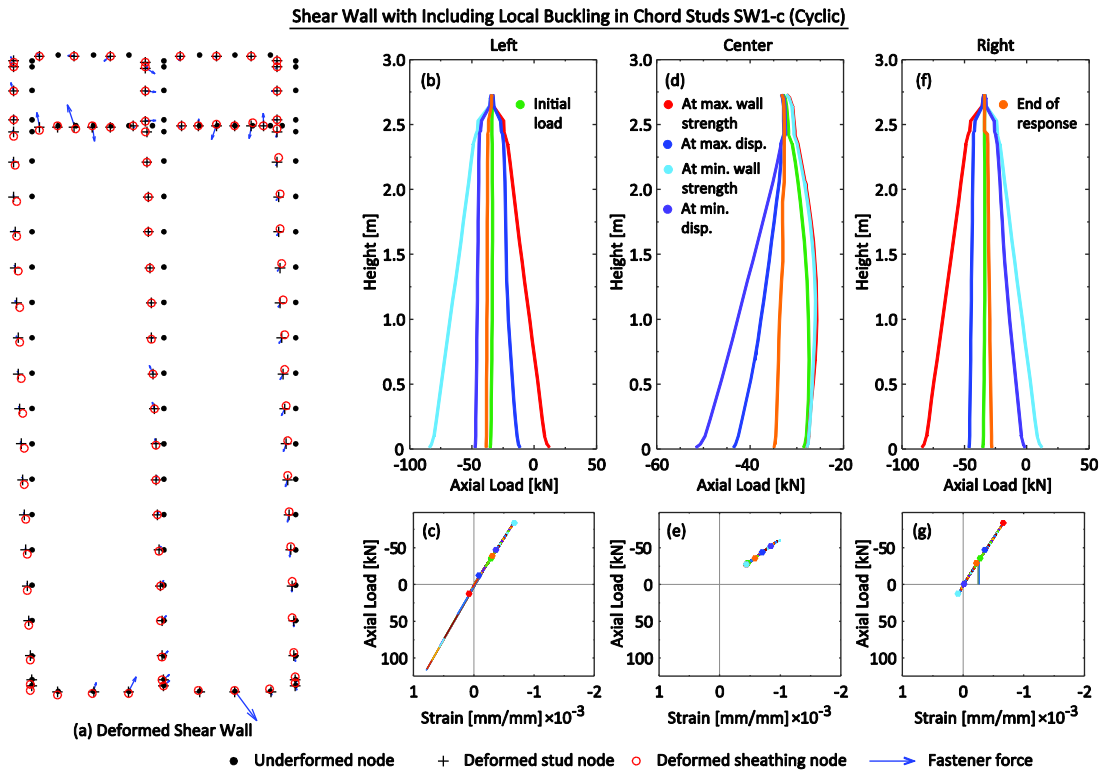

Fig. 6.22. Shear wall (SW1-c) deformed shape from cyclic loading (a) showing fastener failure along the edges and (b) studs remain elastic.

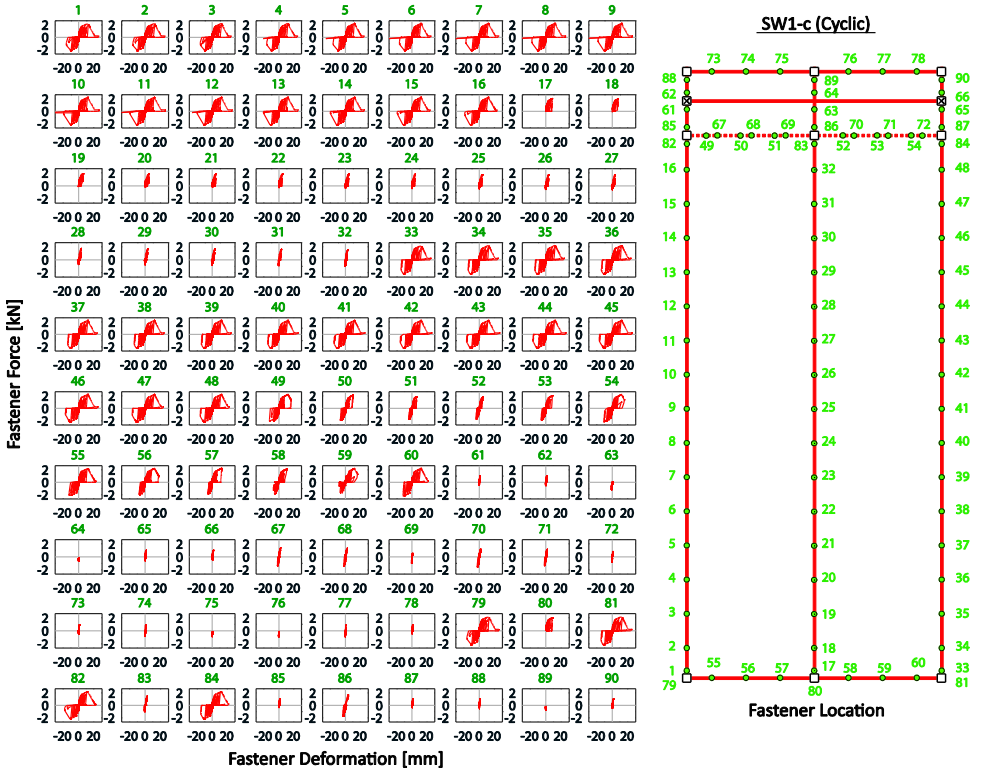

Fig. 6.23. Fastener cyclic responses in shear wall (SW7-b) where edge fasteners fail, while the studs remain elastic

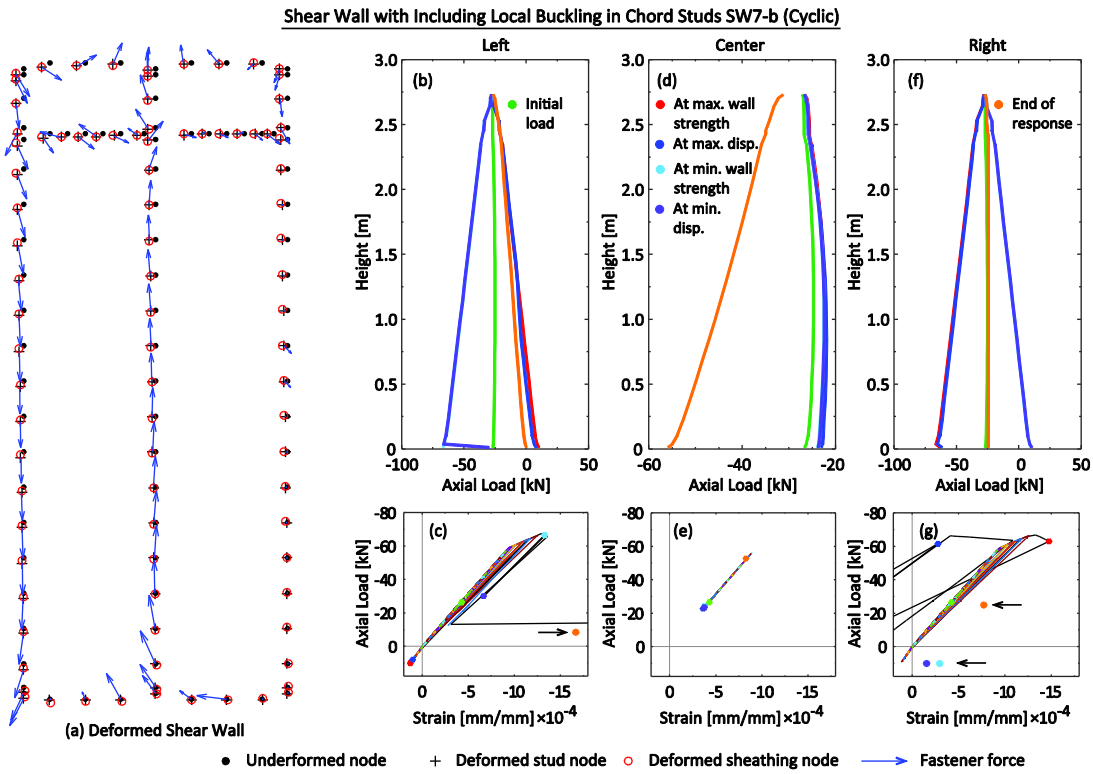

Fig. 6.24. Shear wall (SW7-b) deformed shape from cyclic loading (a) showing the wall failure mechanism triggered by local buckling of the chord studs.

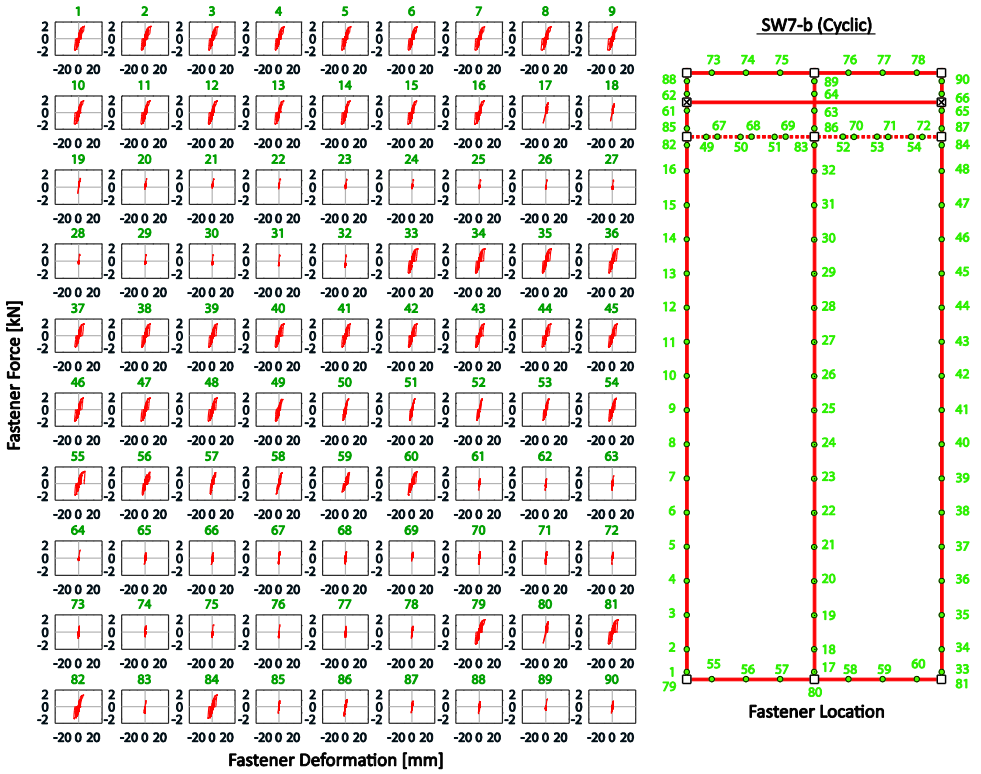

Fig. 6.25. Fastener load-deformation responses in shear wall (SW7-b) where failure is triggered by buckling in the chord studs.

6.9 High-fidelity shear wall simulation model in ABAQUS

In this section, the shear wall in Fig. 6.3 is modeled using thin-shell finite elements for framing members and the UEL proposed in Chapter 5 to simulate the member-to-sheathing screw-fastened connections. Simulations are carried out using a modified model based on the work by Ngo [96] as shown in Fig. 6.29. The wall dimension is 4 ft. by 9 ft. Only front sheathing (OSB) is installed and there is no gypsum sheathing. The rating of the OSB sheathing is APA 24/16 Exposure 1. The thickness is 7/16 in. The cold-formed steel frames consist of five studs, two tracks and one ledger. The dimension of studs is 600S162-54 mil (50 ksi). The dimension of track is 600T150-54 mil (50 ksi). The dimension of ledger is 1200T200-97 mil (50 ksi). Studs are fastened by #10 Hex head washer back to back on the left and right side of the shear wall to form the chord studs. The tracks are fastened to studs by #10x3/4 in. flat head screws. The OSB are connected to CFS members by #8x1-15/16 in. flat head. Fastener spacing is 6 in. There is a seam existing between the two OSB sheathing boards. However, for simplicity, the seam and fastener connecting steel strap to OSB sheathing boards are not modeled.

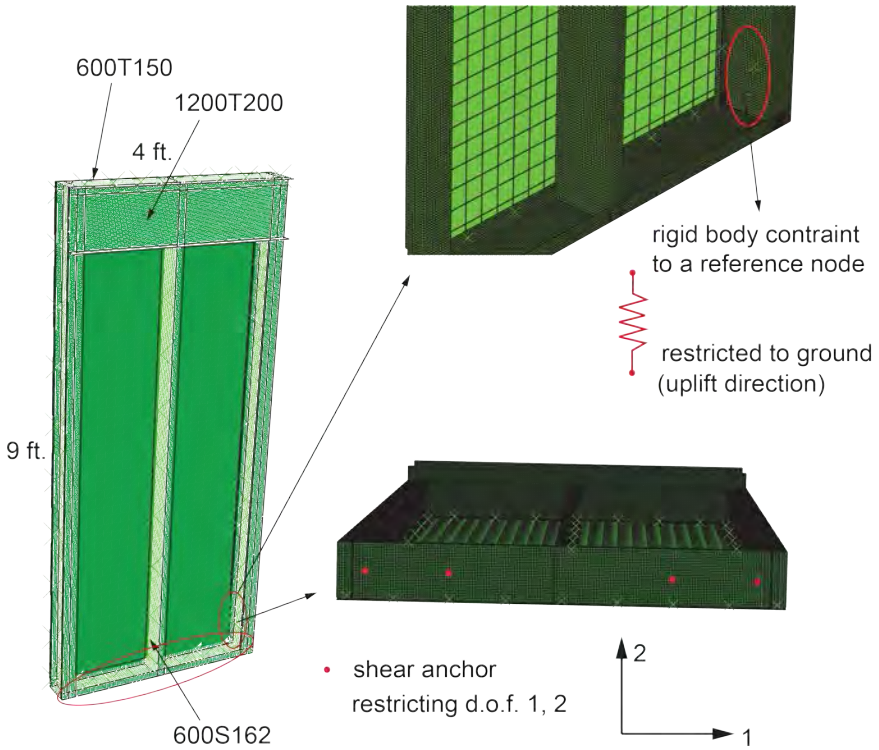

Fig. 6.26. Shear wall numerical ABAQUS model [96]

6.9.1 OSB sheathing modeling

The S4R shell element in ABAQUS is used to model the 11mm (7/16in.) thick OSB sheathing boards. The original model created by Ngo [xx] assumes OSB sheathing as rigid diagrams by assuming very large modulus of elasticity to OSB material. To consider flexural and shear deformation of OSB sheathing board, the OSB material is modified based on reported panel strength values from APA Panel Design Specification [98]. Elastic Young modulus and shear modulus are back calculated using Eq. respectively from the APA reported values as suggested in [97].

$$E = 12EI_w / t_w^3 \quad 6.1$$

$$G = Et_w / t_w \quad 6.2$$

OSB is an orthotropic material and the APA Panel Design Specification [98] considers this by specifying panel strength in the direction parallel to the strength axis and perpendicular to the strength axis. The panel strengths considered in this study are listed in Table 6.4 as flexure and shear rigidities. By converting panel rigidity to modulus of elasticity, orthotropic OSB material parameters can be determined.

Table 6.4. OSB Panel flexural and shear rigidity

Plate bending stiffness (strength axis) E_1I_w (lbf-in.^{2}/ft.)	**Plate bending stiffness (non-strength axis)** E_2I_w (lbf-in.^{2}/ft.)	**Shear rigidity (through thickness)** $G_{v1}t_v$ (lbf/in.)
78000	16000	83500

Table 6.5. Converted OSB material modulus of elasticity

Modulus of elasticity (strength axis) E_1 (ksi)	**Modulus of elasticity (non-strength axis)** E_2 (ksi)	**Shear modulus (through thickness)** G_{12} (ksi)
1068	219	200

For orthotropic elastic material definition in ABAQUS, modulus of elasticity parameters and Poisson's ratio in 3-dimensions are required. The flexural modulus in the direction normal to the wall plane is not important in this analysis. The flexural modulus E_3 is assumed to be equal to E_2 as 219 ksi. Because out-of-plane shear deformation is not significant in shear wall analysis, the shear modulus corresponding to out-of-plane direction is taken to be the same as in-plane. Therefore, G_{13} is set be to 200 ksi. Poisson's ratio in all directions are taken as 0.30.

6.9.2 CFS members modeling

CFS members (i.e., studs, tracks and ledger) are Modeled using S4R thin-shell elements. A fine meshing is used for CFS members to capture better the thin-walled behavior. The steel material is modeled with isotropic hardening. The choice of plastic or elastic material model has little effect on general shear wall load-deformation response. However, it affects simulation of CFS members' torsion and buckling behaviors. With elastic material model, it is found that unreasonably high stress concentration will occur at the bottom track close to hold-downs and anchor bolts. Comparison is made between monotonic shear wall analysis with elastic steel material in Fig. 6.27 and one with plastic material in Fig. 6.28.

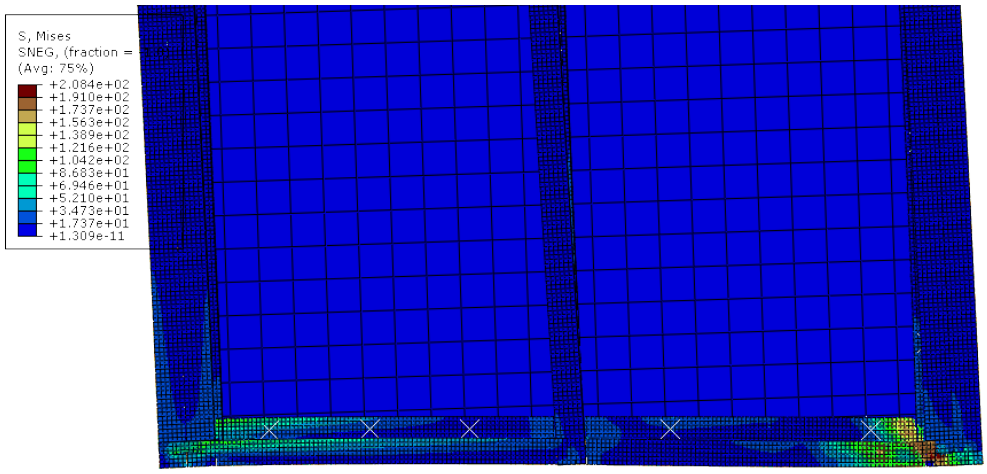

Fig. 6.27. Stress distribution in bottom track at maximum wall deformation using elastic steel material

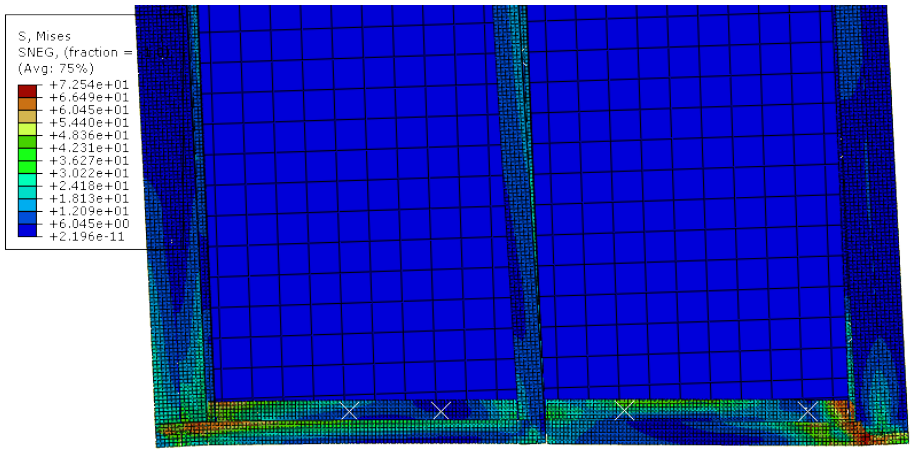

Fig. 6.28. Stress distribution in bottom track at maximum wall deformation using plastic steel material

Therefore, it is recommend herein that plastic material model should be used to model cold-formed steel instead of only using elastic model. The steel elastic properties are 29,500 ksi (Young's modulus) and 0.3 (Poisson's Ratio). The isotropic hardening parameters are taken from the work by Moen [47].

Table 6.6. Isotropic hardening parameters

Plastic Strain	**Stress** ksi
0	55.1
0.003	60.3
0.008	64.9
0.013	68.4
0.023	74
0.033	78.1
0.043	81.3
0.053	83.8
0.063	86.2

6.9.3 Fastened connections modeling

There are mainly two types of screw-fastened connections in the shear wall modeled here, steel-to-steel and steel-to-OSB. Steel-to-steel connections are relatively "rigid" compared to steel-to-OSB connections. From experiments, rarely were any steel-to-steel connections found to have failed. There, multi-point constraint pin type (MPC PIN) is used to simulate steel-to-steel connections.

The UEL proposed in Chapter 5 is used to model steel-to-OSB connections. The configuration of these connections is 54 mils to 7/16'' OSB. Calibrated *Pinching4* model parameters from [95] are assigned to the UEL so that connection nonlinearity can be simulated. In order to consider changes in displacement trajectory, the radial spring model is used for the UEL. The distance between CFS node and OSB node is set to be 0.2373'' equal to the distance between CFS and OSB centerlines.

6.10 Pushover analysis in ABAQUS

6.10.1 Influence of analysis procedures

The cold-formed steel frame shear model modeled in this section was already tested in an experiment. It was found that the shear wall displayed a "brittle" loss of capacity after reaching its peak load (Fig. 6.29). Such sudden loss of capacity presents potential challenge for numerical analysis. In some cases, default Newton-Raphson method in ABAQUS may not be able to

capture post-peak response of shear walls. In order to find a reliable solution procedure, several analysis procedure options are explored in this section. Their results are compared and discussed.

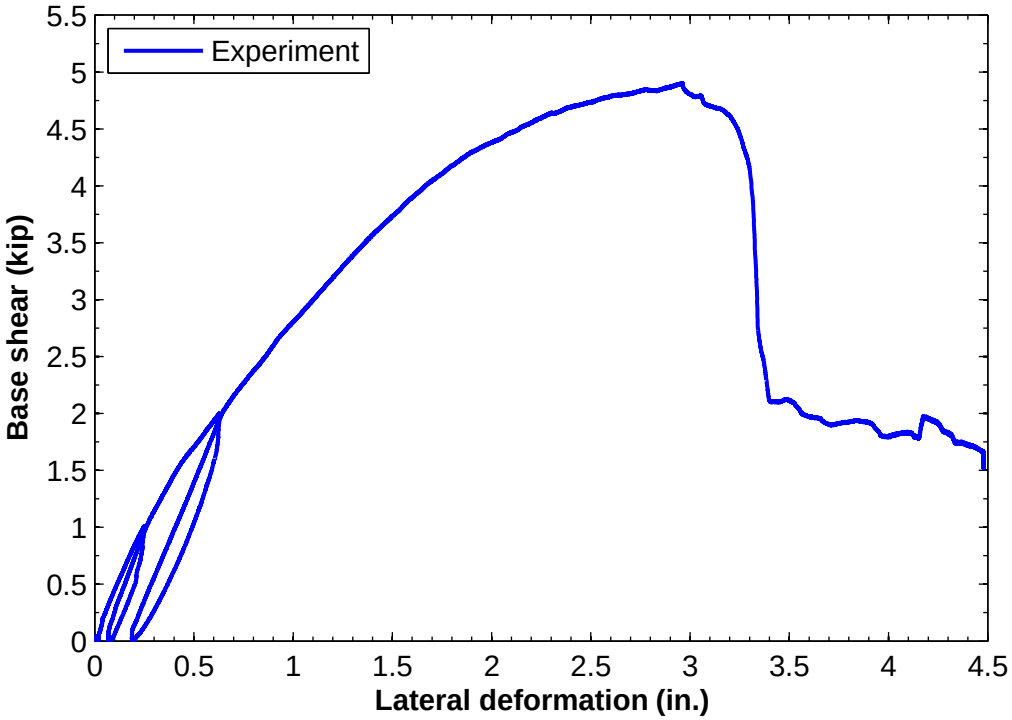

Fig. 6.29. Load-deformation response of shear wall under monotonic loading

The solution techniques applied are Newton-Raphson method, Riks method and implicit dynamic method. The Newton-Raphson method is the default nonlinear solution technique in ABAQUS/Standard. It needs the inverse Jacobian matrix in every iteration to calculate incremental displacement correction, which makes it sometimes numerically expensive for obtaining solution. It is an effective and accurate analysis procedure for most of problems. However, for problems tracing scenarios of unstable collapse or post-buckling, Newton-Raphson method sometimes fails to converge. For these problems, Riks method can be more reliable, especially for cases with geometric nonlinear collapse. Riks method iterates by the use of "arc length". Both displacement and load are unknown variables to be solved. However, because of the way that Riks method is formulated, it cannot be used for cyclic analysis.

The implicit dynamic analysis is also investigated here. Even though implicit dynamic method stills uses Newton-Raphson method, it considers damping and acceleration, which can potentially "dissipate" nodal residuals and improve convergence. The study also demonstrates

the UEL's potential for dynamic analysis. The solution procedure and time increment input are based on the work done by Moen [47].

For implicit dynamic analysis, material mass is applied to cold-formed steel and OSB sheathing based on real material density. The UEL is only assigned with the mass of a fastener. Rayleigh mass proportional damping with α equal to 0.005 is assigned for energy dissipation. The loading rate is taken as 0.00004 in./sec to minimize inertia effects.

The cold-formed steel shear wall model introduced in this chapter is analyzed in ABAQUS using Newton-Raphson method, Riks method and implicit dynamic analysis. The shear wall load-deformation curves are shown in the Fig. 6.30. The results from three different analysis methods are compared. The horizontal axis "Displacement" corresponds to the drift at the top the shear wall. The vertical axis "Load" corresponds to the shear wall base shear.

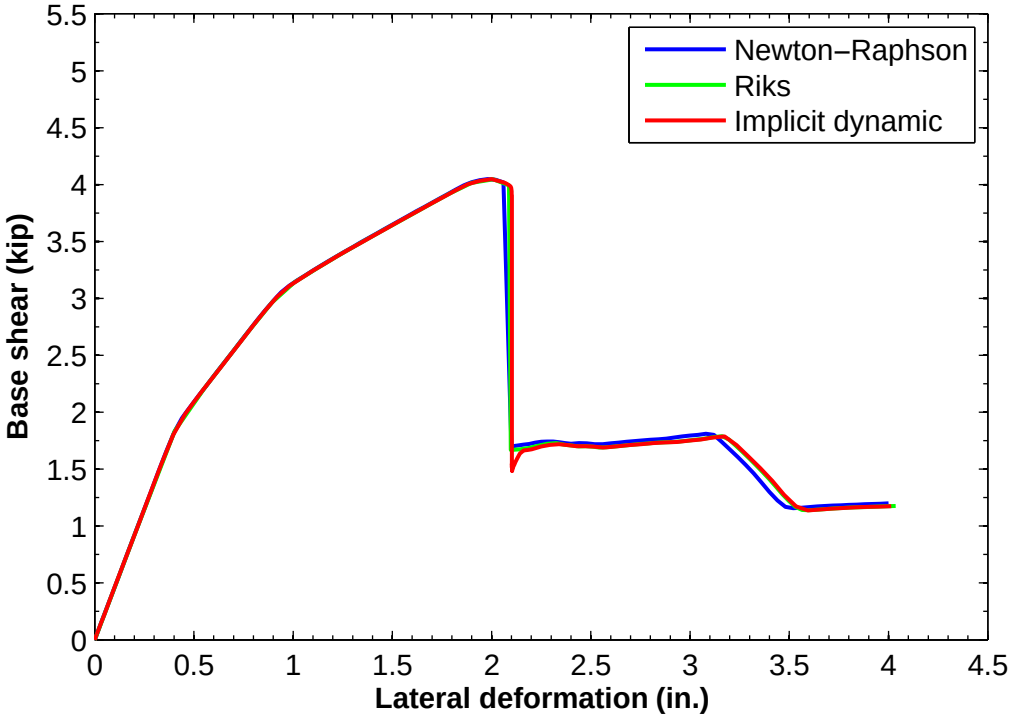

Fig. 6.30. Comparison of numerical analysis results using different solution procedures

All of the three analysis methods succeed in capturing post-peak response and eventually converge. As shown in the Fig. 6.30, the three analysis procedures predict basically the same peak load and corresponding displacement. Prior to reaching the peak load, same shear wall response is calculated by the three methods. After reaching the peak load, there is minimal

difference between Newton-Raphson static method and Riks method. Implicit dynamic method creates slightly different post-peak behaviors with lower post-peak load immediately after loss of capacity. However, it gradually catches up with load-deformation paths of the other two methods. This means that the difference might be caused by acceleration induced by the "sharp" capacity loss since this difference is eventually dissipated.

From this comparison, it can be shown that Newton-Raphson method is sufficient for obtaining converged solution for shear wall pushover analysis. But for the case when Newton-Raphson method fails to converge, Riks method and implicit dynamic method are available.

6.10.2 Comparison to experiment

Shear wall numerical analysis result is compared to experiment in this section. In this analysis, radial spring model is selected for simulating screw-fastened connections and Newton-Raphson method is used for obtaining solution. The steel-to-sheathing connection Pinching4 parameters are taken from work by Padilla-Llano [99]. These Pinching4 parameters are shown in Table 6.7 and Table 6.8.

Table 6.7. Steel-to-sheathing Pinching4 backbone parameters

ePd_1	ePd_2	ePd_3	ePd_4	ePf_1	ePf_2	ePf_3	ePf_4
	(in.)				(kip.)		
0.022	0.124	0.462	0.815	0.192	0.384	0.5	0.049
ePd_1	ePd_2	ePd_3	ePd_4	ePf_1	ePf_2	ePf_3	ePf_4
	(in.)				(kip.)		
-0.022	-0.124	-0.462	-0.815	-0.192	-0.384	-0.5	-0.049

Table 6.8. Steel-to-sheathing Pinching4 pinching path parameters

rDispP	*rForceP*	*uForceP*	*rDispN*	*rForceN*	*uForceN*
0.42	0.01	0.001	0.42	0.01	0.001

The load-deformation curve of numerical analysis in comparison to experiment result is shown in Fig. 6.31. The numerical analysis gives very accurate prediction of shear wall response with slight inelasticity as shown in the first and second "legs" of the curve. However, the shear wall stiffness is underestimated after the shear wall enters severe softening state as shown in the third "leg". Regardless of the discrepancy caused by underestimated stiffness, the predicted post-peak response closely resembles experiment result.

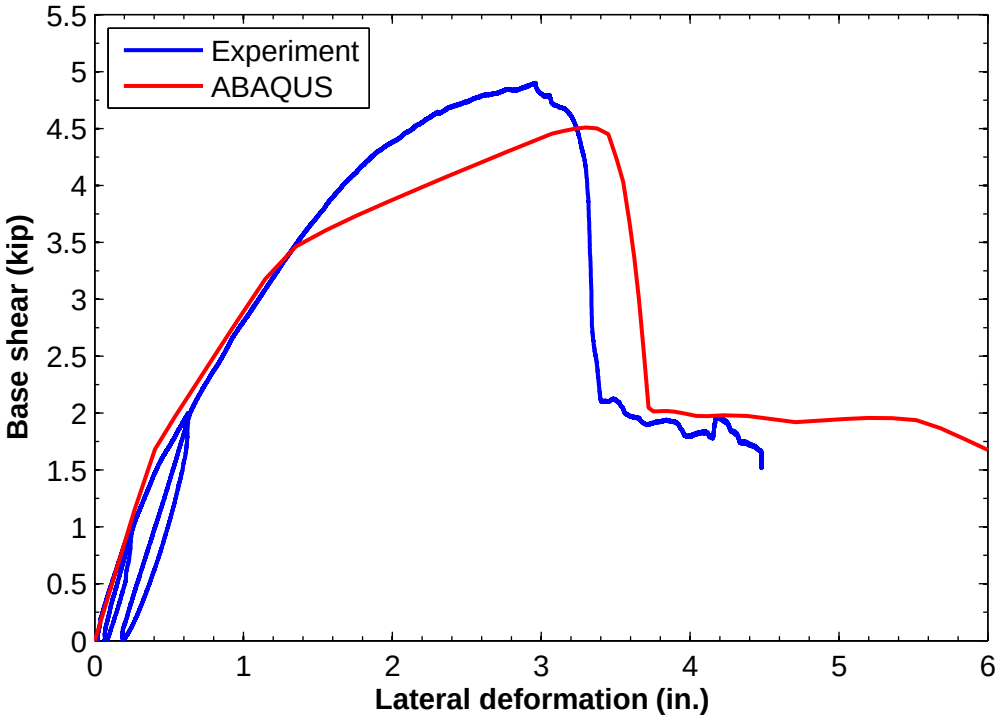

Fig. 6.31. Comparison of numerical analysis result to experiment

According to experiment data, the response of cold-formed steel frame shear wall under monotonic loading is controlled by screw-fastened connection failures where sequential connection failures lead to gradual softening of shear wall response until the number of failed connections is enough to lead to shear wall failure. Therefore, the input for connection Pinching4 parameters is critical for obtaining correct simulation. Curves of connection force with respect to shear wall lateral displacement are created in Appendix C. It is found that the initiation and end of three pre-peak legs in these curves correspond to the three legs in the shear wall load-deformation curve. Thus, the third leg of connection Pinching4 backbone might be inappropriately chosen, which results into the difference between experiment results and numerical analysis. More study on single screw-fastened connection may need to be done in order to obtain closer simulation result.

The shear wall general deformed shear wall is shown in the Fig. 6.32. The shear wall as a whole deforms as a deep beam. The cold-formed steel frames is deformed as a parallelogram with slight bending. Torsion occurs on the middle stud as shown in Fig. 6.34, which is induced by fasteners connecting studs only on one side. The top portion of the cold-formed steel studs

experience relatively high stress. This is possibly due the restraint created the ledger. The highest stress concentration on cold-formed steel studs occur at the hold-down areas, where steel around track-to-stud connections have entered hardening stage (Fig. 6.35). The OSB sheathing is found to rotate relative the cold-formed steel frame as shown in Fig. 6.36. It experiences much lower stress compared to cold-formed steel.

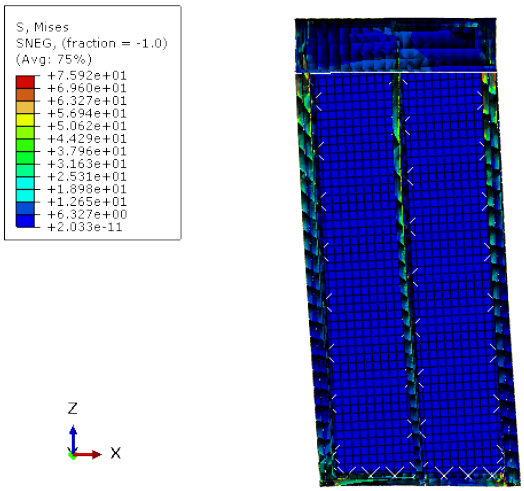

Fig. 6.32. Shear wall general deformed shape at maximum shear wall displacement

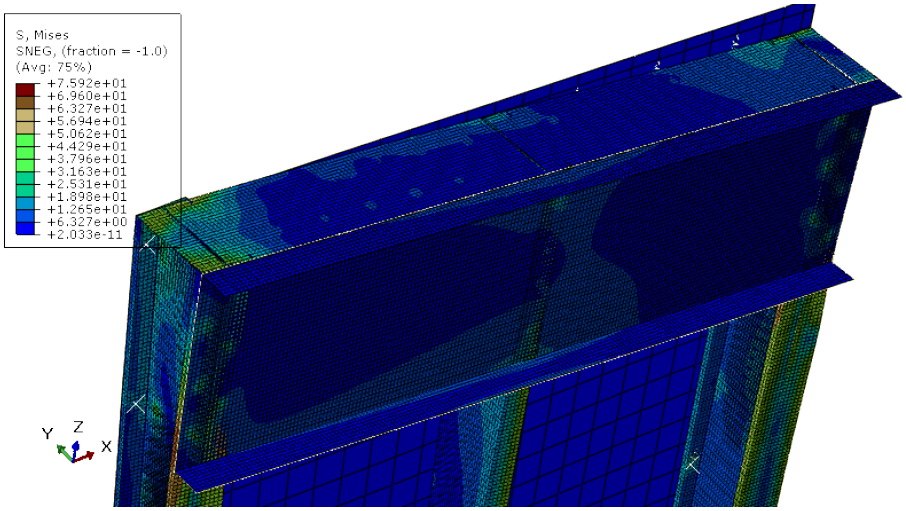

Fig. 6.33. Shear wall top track and ledger area Von Mises stress distribution at maximum shear wall displacement

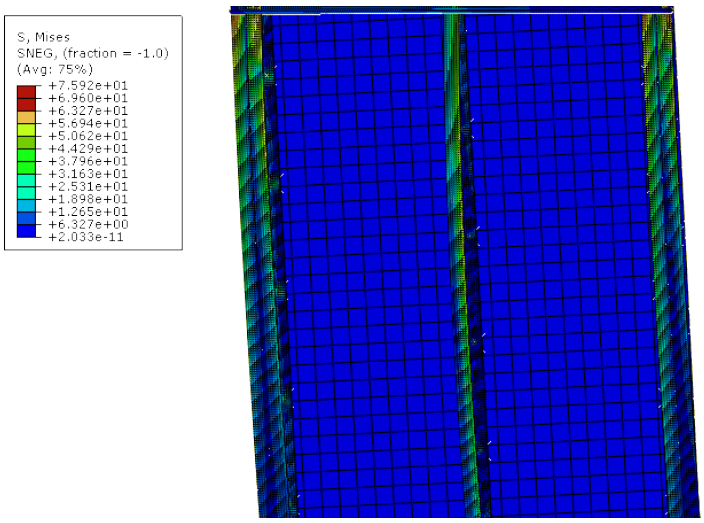

Fig. 6.34. Torsion of cold-formed steel studs of the shear wall at maximum lateral deformation

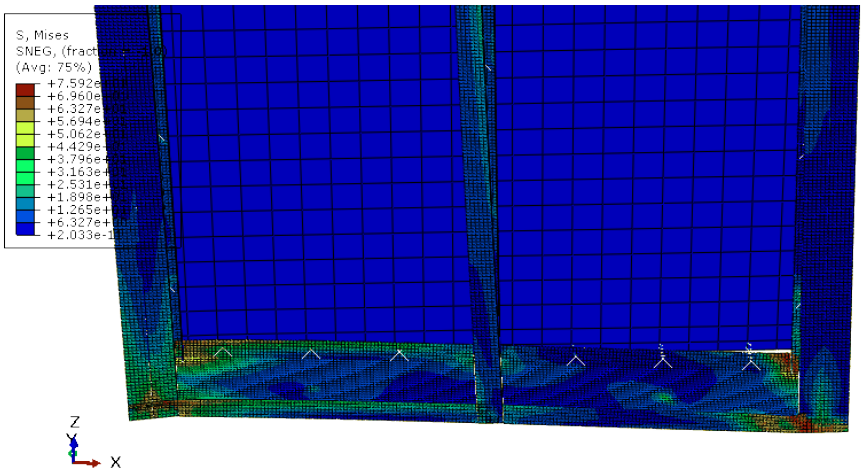

Fig. 6.35. Shear wall bottom track and stud stress distribution at maximum shear wall deformation

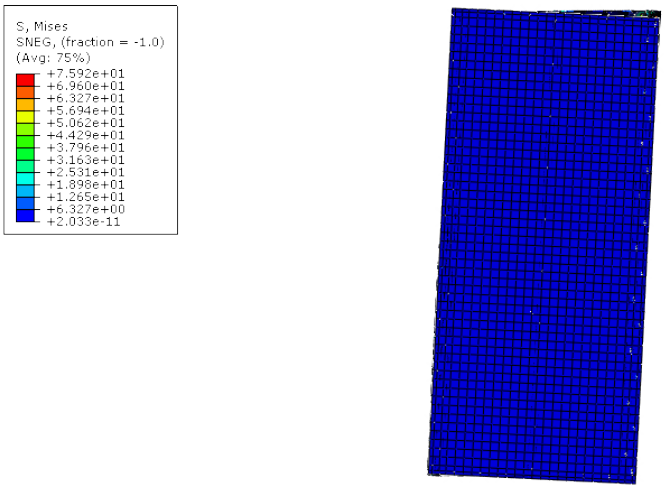

Fig. 6.36. Rotation of OSB sheathing at the maximum shear wall displacement

In terms of connection behavior, as shown in Fig. 6.37, the connections with distinctive failures during testing are labeled. Most of connection failures occurred at the bottom of the shear wall. Almost all track-to-sheathing connections failure by sheathing pull-through failure. Failures of stud-to-sheathing connections are mostly located at the stud lower part close to hold-downs. However, more connections failed on the right side than the left side. This might be explained by the difference between hold-down tension and compression stiffness.

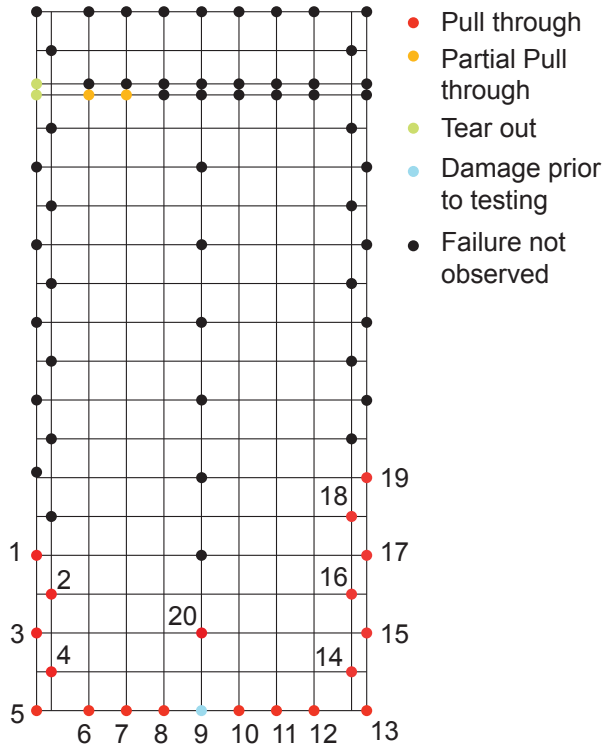

Fig. 6.37. Distribution of failed connections on the shear wall during testing [96]

The Fig. 6.38, Fig. 6.39 and Fig. 6.40 are created showing respectively the response of the damaged connections on the left side, right side and the bottom. It can be seen that all connections shown here have been loaded past their strength, which agrees with experiment observation. However, connections post-peak behaviors are very different. Many connections on the left and bottom undergoes unloading after reaching peak load, while the right side connections continue being loaded along the backbone curves. This phenomenon may be caused by the difference of hold-down stiffness in compression and tension.

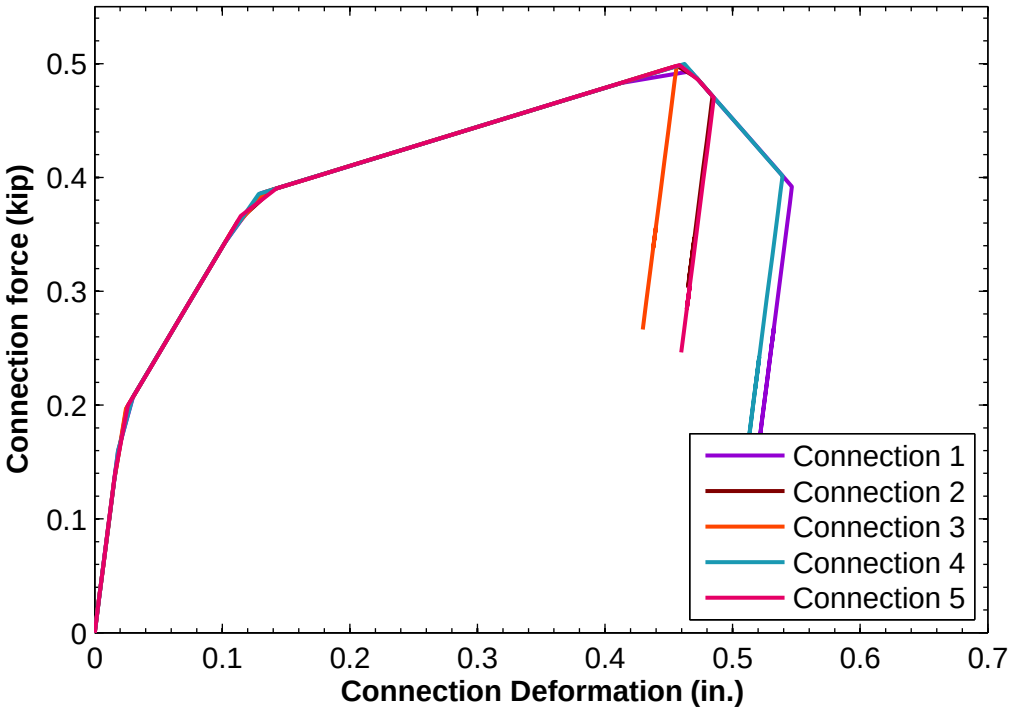

Fig. 6.38. Load-deformation response of the connections on the left stud bottom

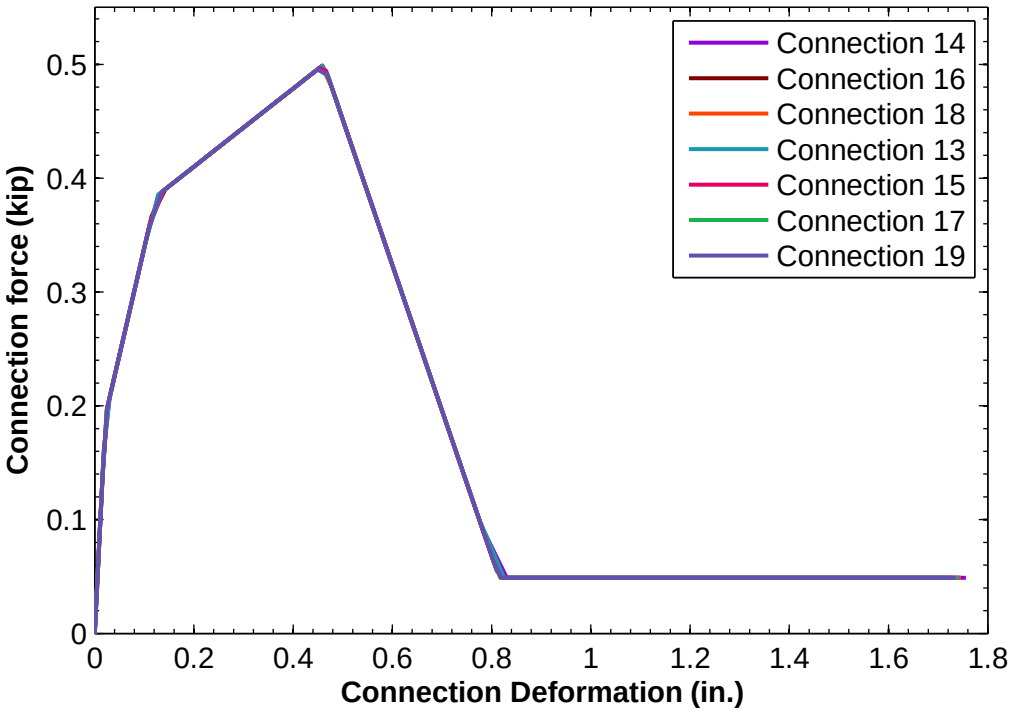

Fig. 6.39. Load-deformation response of the connections on the right stud bottom

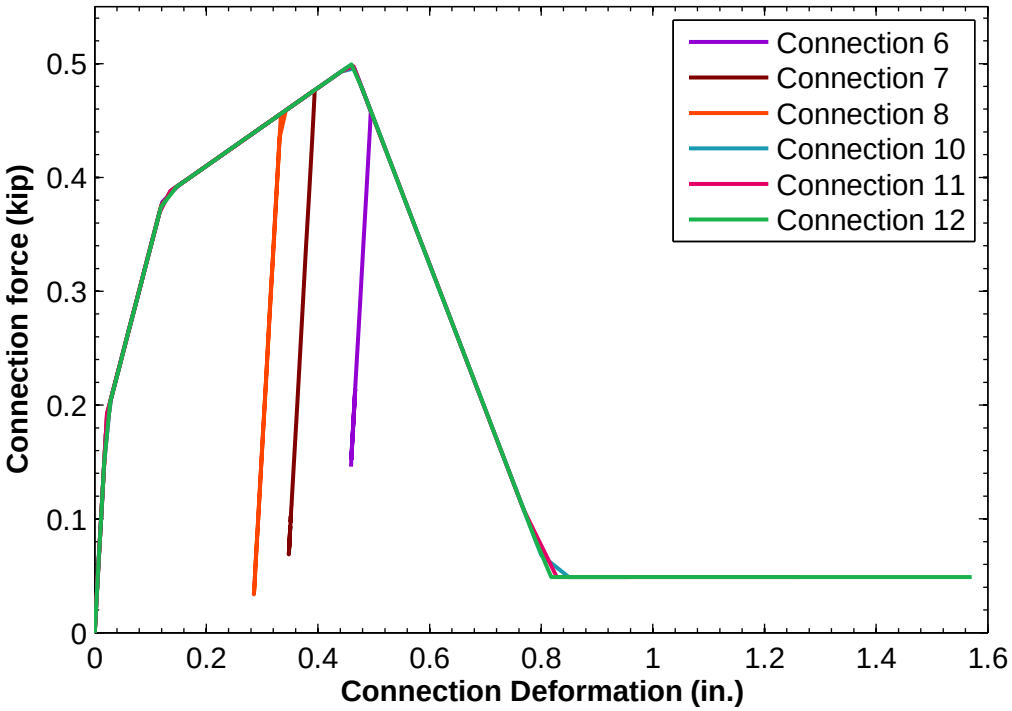

Fig. 6.40. Load-deformation response of the connections on the bottom track

6.11 Cyclic analysis in ABAQUS

6.11.1.1 Fastener-only model study

Compared to pushover analysis, loading and unloading in cyclic analysis adds more numerical difficulty for convergence. In order to settle on robust modeling technique, a fastener-only model (Fig. 6.41) is created by modifying original high-fidelity shear wall discussed in the last section. All the shell elements from the original shear wall model are discarded leaving only the screw-fastened connections modeled by the UEL. Rigid diaphragm assumption is assigned to the UEL nodes originally connected to sheathing shell elements. The other nodes on UEL are pinned to the ground. Cyclic displacement loading is prescribed on the reference node the top of the rigid diaphragm. The cyclic loading protocol used in Chapter 5 is applied here with scale factor of 1.5. Under the cyclic displacement loading, the UEL will experience relative displacement between its two nodes and then establish resistance. Instead of trying to simplify original shear wall model, this fastener-only model is intended to mimic the relative displacement between CFS members and OSB sheathing which is the deformation of the UEL.

It is found that the model quickly divergences after two cycles when some fasteners enter inelastic state. The reason for this divergence is that change in stiffness of fasteners causes reestablishment of fastener orientation. Orientation reestablishment sometimes leads to change in element deformation. For radial spring model, the spring orientation is updated in each iteration. Combined with nonlinear model, the spring orientation can oscillate by a large amount and thusly create a cycle of reloading and unloading in one increment. This possibly contributes to divergence.

In order to solve the divergence issue, the element formulation in the original UEL is modified. Instead of being a zero length element free to rotate its orientation, the element orientation is "locked" in the prescribed direction. The direction is determined based on the orientation that element establish in elastic state. The spring orientation "locking" only occurs after connection begins yielding corresponding to Pinching4 backbone after the first curve "leg". This modification is based on the assumption that certain amount damage on the steel-to-sheathing connection will create a deformation path on the sheathing. Connection displacement along this deformation path has the lowest potential energy. Thus, any connection displacement is assumed to follow this deformation path. In summary, before connection begins yielding, the spring remains radial spring capable of rotating its orientation. After the connection begins yielding, the spring "locks" its orientation and changes into modified radial spring. Still only spring is used in order to avoid overestimation of strength and stiffness. It is assumed that screw during testing is relatively "locked" along the sheathing damaged trajectory. With this modification, the fastener-models can converge. The fastener-only model response is shown in Fig. 6.42. It can be seen that the fastener-model result shows clear resemblance to fastener hysteretic response. Both peak load and pinching are simulated in this model.

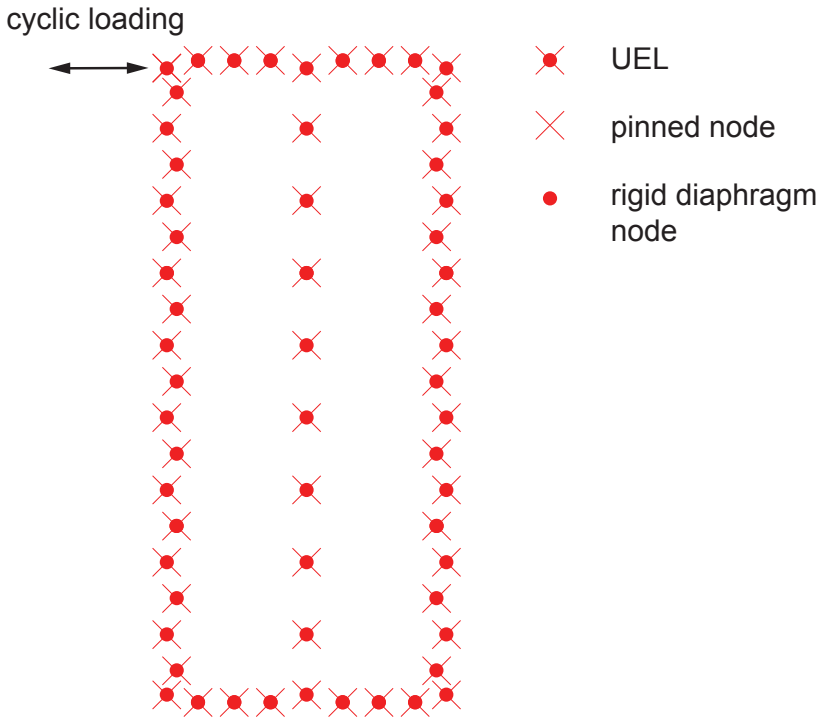

Fig. 6.41. Fastener-only model

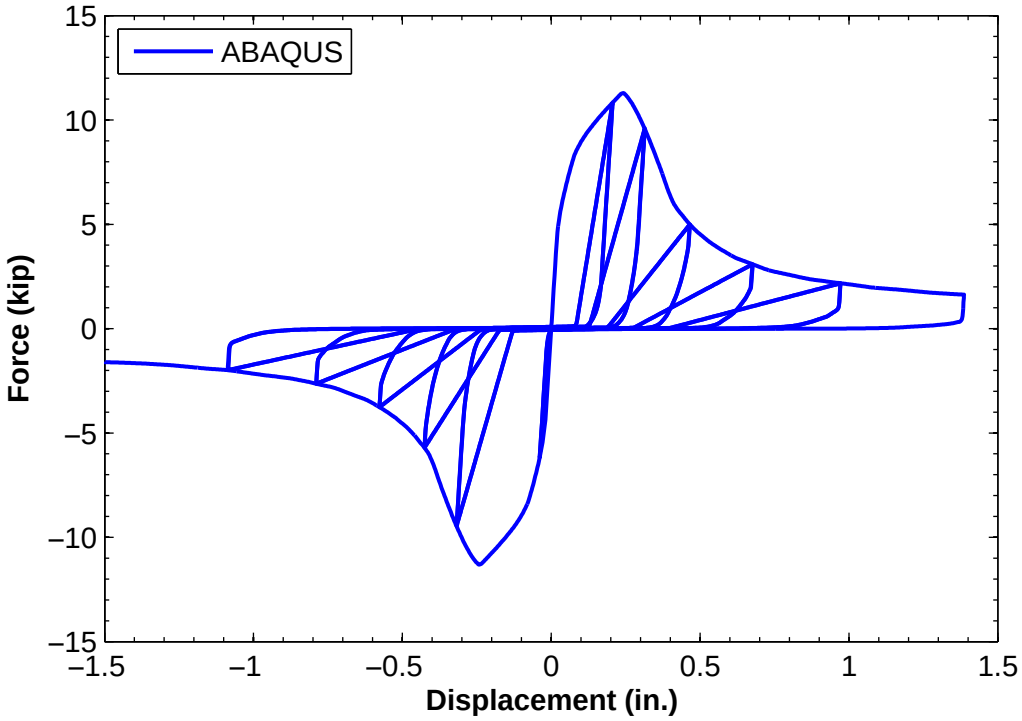

Fig. 6.42. Hysteretic response of fastener-only model

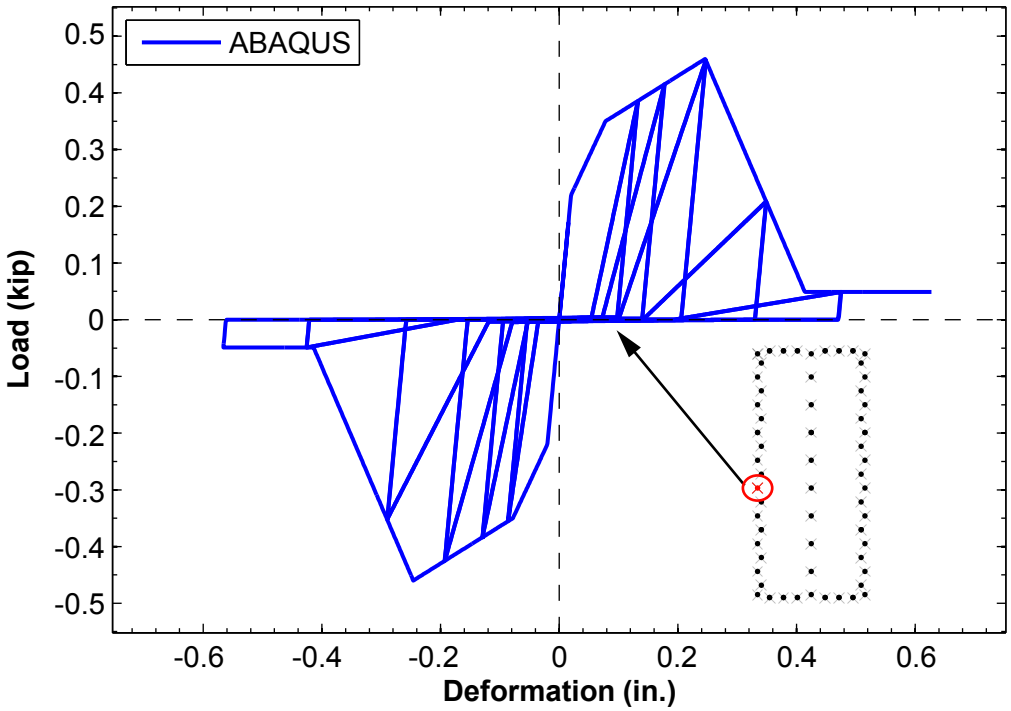

Fig. 6.43. Hysteretic response of one fastener in fastener-only model

6.11.2 High-fidelity model

With the convergent solution obtained in the fastener-only model, the high-fidelity shear wall model analyzed monotonically is assigned with cyclic displacement loading. Still, the modified UEL is used for analysis. Newton-Raphson method is used for obtaining the solution.

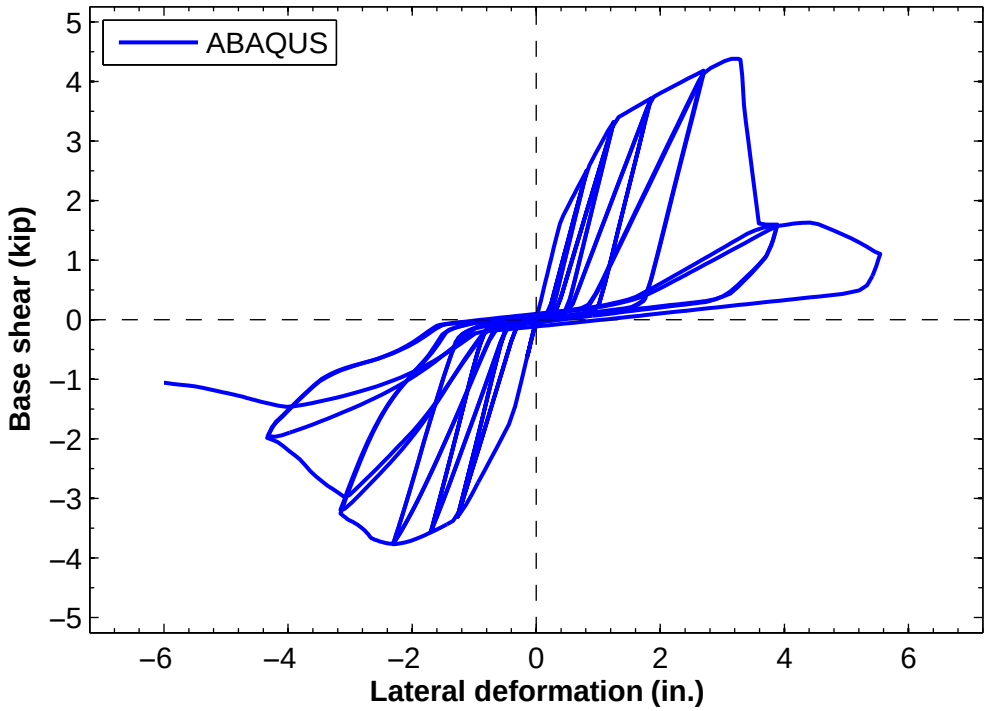

Fig. 6.44. Cyclic response of high-fidelity shear wall model

Shear wall cyclic response shows a nonlinear backbone and pinching. It can be seen that the shear wall cyclic response highly resembles the hysteretic behavior of individual fasteners. Because the shear wall hysteretic response is actually the combination of all individual fastener responses, the shear wall load-deformation curve is smoother than fastener. The response of one of the connections on the top track is shown in the Fig. 6.45.

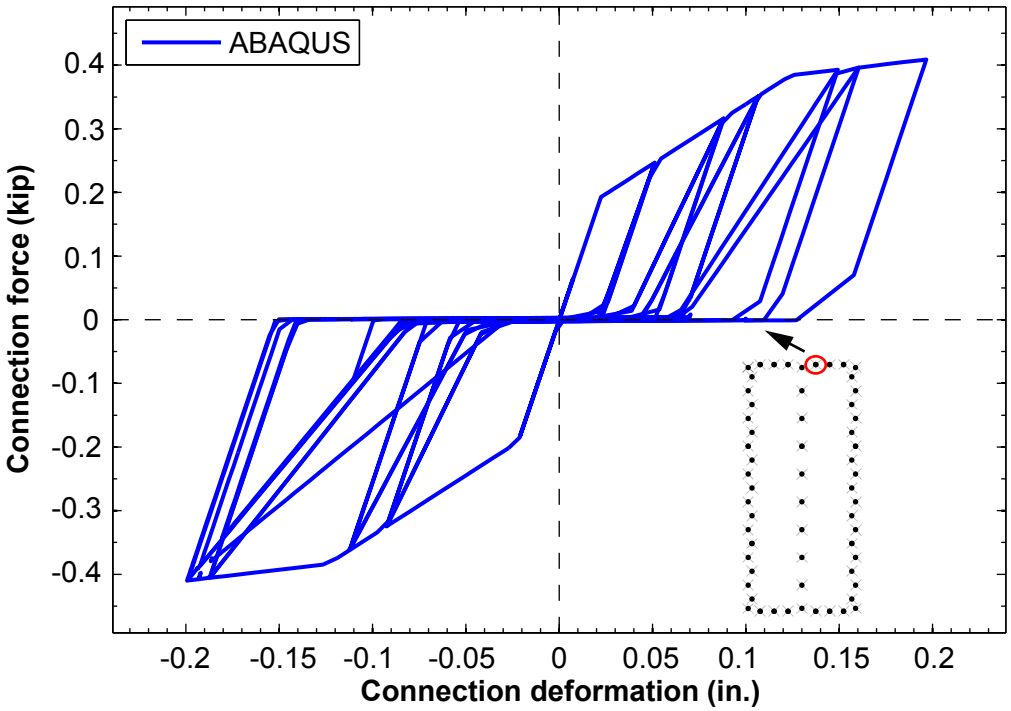

Fig. 6.45. Hysteretic response of one screw-fastened connection

Before the shear wall reaches its peak load, the total shear wall stiffness and strength is mostly provided by the steel-to-sheathing connections. As shown in Fig. 6.46, at shear wall peak load, there is no significant deformation on the CFS framing members except high stress concentration around hold-downs. The CFS steel frame is deformed as parallelogram providing little strength and stiffness. However, after most steel-to-sheathing connections fails, the lateral rigidity from OSB sheathing cannot be provided. In this condition, the CFS frame begins to resist the lateral displacement. This changes the failure mechanism. CFS frame in this period experiences very large deformation. The studs on the compression side experiences flexural-torsional buckling as shown in Fig. 6.47. Since steel-to-sheathing connections have already failed, the studs become unbraced along its full length making them susceptible to global buckling. Overall, this

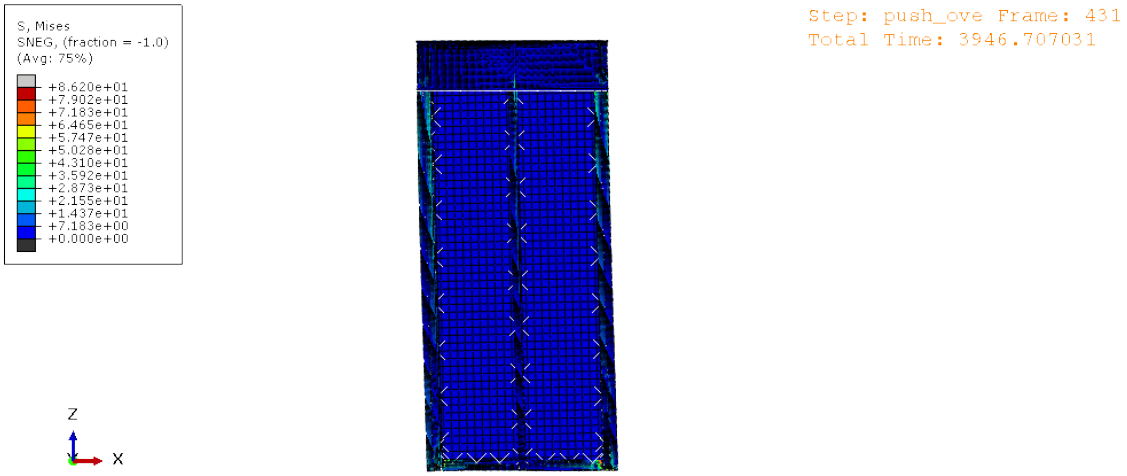

Fig. 6.46. Deformed shape of the shear wall at the maximum load

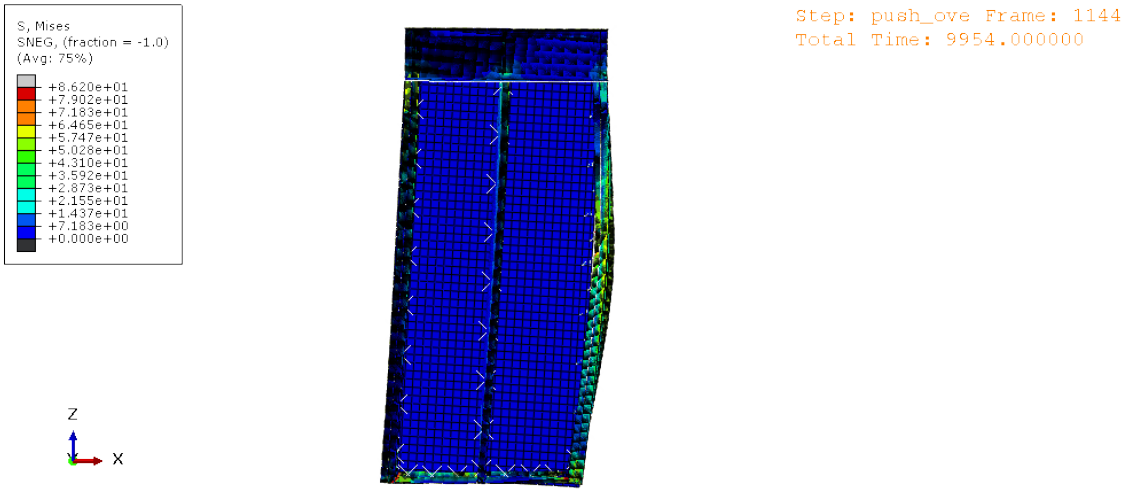

Fig. 6.47. Deformed shape of the shear wall at the maximum displacement

6.12 Conclusions

In this chapter a computationally efficient component based simulation framework for cold-formed steel structures that captures the nonlinear behavior in all critical components was introduced. Cold-formed shear walls were simulated and discussed to illustrate the use of the framework and its advantages. Nonlinear behavior in critical components was included using the *asymPinching* model developed in Chapter 4 for framing members, and *Pinching4* for screw-fastened connections. The capability of the framework to easily modify the geometry or material properties allows exploring different loading scenarios as it was demonstrated by the small study on the shear wall behavior discussed. The results from the shear wall study highlighted the need to include local buckling behavior when analyzing structural systems with thin-walled members.

Including local buckling and any other nonlinear behavior can reveal additional limit states and failure mechanisms that may go unnoticed if not included.

The introduction of the user element from Chapter 5 in the simulations using thin-shell finite elements in ABAQUS permitted simulating shear wall responses while including explicitly the thin-walled behavior in the framing members and sheathing. The inclusion of this UEL would allow designers to include fastener behavior where properties can easily be derived from common screw-fastened connection tests.

Chapter 7: Conclusions and Future Work

7.1 Conclusions

A computationally efficient component-based framework for the analysis of light-framed steel structures was introduced. The framework is supported by nonlinear hysteretic models that capture thin-walled behavior in framing members and nonlinear behavior in screw-fastened connections. Models needed for the framework were calibrated from cyclic tests conducted at Virginia Tech.

Finite element analyses using ABAQUS were performed to explore cyclic behavior and energy dissipation mechanisms in thin steel plates. Energy dissipation in thin-plates occurs through accumulation of plastic deformations at localized damaged zones that coincide with the leading buckling half-wave. The shape of the initial imperfections influenced where these damaged zones occurred. This study provided insight into the cyclic behavior and energy dissipation in thin-walled cross-section elements, such as webs and stiffened elements.

A framework to include thin-walled behavior into the modeling of framing axial and flexural steel members was introduced. This framework consisted of a hysteretic model that captures the nonlinear behavior including thin-walled behavior attached to a nonlinear beam column or spring element. The results from the experimental program were used to develop the hysteretic model parameters including backbone curves, strength degradation, and stiffness degradation for each of the tests. This set of parameters were used to illustrate the approach to model thin walled behavior in steel axial and flexural members using beam-column elements and hysteretic springs.

The framework for modeling thin-walled behavior in steel members was then specialized into the hysteretic model, *asymPinching* for simulating steel columns cyclic behavior including local buckling. General expressions were develop for backbones, total energy dissipation capability, strength degradation and stiffness degradation as a function of the member local slenderness λ_ℓ. These expressions were developed from monotonic and cyclic responses obtained through nonlinear finite element simulations in ABAQUS of cold-formed steel columns which strength predicted by AISI-S100-12 [22] is govern by local buckling. The set of columns simulated covered a wide interval of cross-section local slenderness from stocky to slender thin-

walled cross-sections (λ_ℓ from 0.69 to 3.39). Initial imperfections simulated using a 1D spectral approach were included, as well as steel plasticity implemented using combined nonlinear isotropic-kinematic hardening. Steel damage initiation and evolution was also included to simulate the effects of material deterioration due to cold-bending and fracture. The nonlinear finite element modeling protocol was validated against the cyclic responses obtained experimentally.

Even though the proposed methodology is established for thin-walled cold-formed steel members, the *asymPinching* model parameters are presented generally as a function of local buckling slenderness λ_ℓ and could be extended to hot-rolled steel members and cross-sections with future validation. The same methodology could be applied to thin-walled cold-formed steel members that experience distortional and global buckling with further validation. Moreover, the *asymPinching* model can be applied to any material, component or subassembly that exhibits asymmetric pinched hysteretic behavior.

A computationally efficient component based simulation framework for cold-formed steel structures that captures the nonlinear behavior in all critical components was introduced. The framework includes the *asymPinching* to model thin-walled behavior in framing members and allows to consider different loading scenarios and changes in geometries in the analyzed structural system. An illustrative example highlighted the need to include local buckling behavior and any other nonlinear behavior in components when analyzing structural systems with thin walled members as it can reveal additional limit states and failure mechanisms that may go unnoticed if these are not included.

7.2 Future research topics

The following are research topics that are identified as needed to advance the framework for CFS structures.

Computationally efficient models for components and structures:

Efficient models to simulate the behavior of members and connections are needed to advance performance analysis based engineering of light-framed steel structures. Additional work to further advance the modeling approach described in this dissertation to include thin walled behavior in modeling members is warranted. Similarly, there is need for efficient models

to simulate the typical connections in a light-framed steel structure. The following list summarizes ideas for future research needed on this topic:

- Complete the modeling framework for thin-walled axial members: The framework presented in Chapter 4 to simulate the cyclic behavior including local buckling in axial members needs to be expanded to include the other buckling limit states considered in AISI-S100-12 [22]. Plans are set to developed expressions as a function of slenderness for distortional and global buckling limit states to be used with the *asymPinching* model.
- Sensitivity analysis and validation of the modeling framework for thin-walled members: A sensitivity analysis and validation of the expressions in Chapter 4 is needed. The sensitivity analysis and validation should focus in checking the approach for different cold-formed steel cross-section shapes and possibly hot-rolled steel cross sections.
- Develop general expressions for CFS flexural member hysteretic models: To complete the framework it is necessary to develop expressions for CFS flexural members like the ones described in Chapter 4. The expressions can be set as functions of the member slenderness for local, distortional and global buckling.
- Screw-fastened connection models: General expressions to define the hysteretic model based on fastener and connected parts properties is needed. Currently research is underway to define this parameters.
- A comprehensive beam-column model for thin-walled members: The approach described in Chapter 3 to model cyclic response including thin-walled behavior presents some shortcomings the most relevant being interaction and localization. Axial load-moment interaction which is one important load case for members that are part of the lateral-load resisting system in CFS structures is not included. Localization of the damage as it was observed in the tests and finite element analysis is also not included because of the beam-column element used in this dissertation.

  A comprehensive element model for thin-walled members that can model thin wall behavior is needed. In addition to interaction, the model should capture the buckling phenomena with localization of deformations for most member loading cases, as well as material plasticity and fracture. These element model should be computationally more efficient than a thin-shell finite element model of the member but comparatively accurate. Parameters in the form of

those presented in Chapter 4 can be developed.

- Validation of the analysis framework through high-end finite element analysis or experiments: The analysis framework described in Chapter 6 needs further validation by comparing simulated responses using the framework to experimental responses of shear walls or other CFS systems. In addition to experimental responses, high-end finite simulations (e.g., thin-shell finite element analysis in ABAQUS) can be used for validation.

Assessment and performance factor quantification for CFS structures:

As mentioned in the introduction of this dissertation, there is an ongoing effort to advance performance based analysis and design of cold-formed steel structures. The simulation framework and models introduced in this dissertation can be used to quantify seismic performance factors R, Ω_0 and C_d for cold-formed steel structures and assemblies following the FEMA P695 approach [2]. Also the framework can be used in seismic performance assessment of CFS buildings using the FEMA P58 methodology [86].

Acknowledgements

The authors are grateful to the American Iron and Steel Institute (AISI) for supporting this project, to the AISI Project Monitoring Task Group especially Bonnie Manley, Ben Schafer, Jay Larson, Colin Rogers, Steve Tipping.

References

[1] AISI S213-07. *North American Standard for Cold-Formed Steel Framing: Lateral Design*, American Iron and Steel Institute, Washington, D.C. ANSI/AISI-S213-07, 2007.

[2] FEMA, *FEMA P695-Quantification of Building Seismic Performance Factors*, Federal Emergency Management Agency (FEMA), Document No. FEMA 965, Washington, D.C., 2009.

[3] DaBreo J, Balh N, Ong-Tone C, Rogers CA. Steel sheathed cold-formed steel framed shear walls subjected to lateral and gravity loading. Thin-Walled Structures 2014;74:232–245.

[4] Balh N, DaBreo J, Ong-Tone C, El-Saloussy K, Yu C, Rogers CA. Design of steel sheathed cold-formed steel framed shear walls. Thin-Walled Structures 2014;75:76–86.

[5] Zeynalian M, Ronagh H. Experimental Study on Seismic Performance of Strap-Braced Cold-Formed Steel Shear Walls. Advances in Structural Engineering 2013;16:245–257.

[6] Shamim, I., and Rogers, C. A., "Steel sheathed/CFS framed shear walls under dynamic loading: Numerical modelling and calibration." Thin-Walled Structures, 71, 57 - 71, 2013.

[7] Shamim I, DaBreo J, Rogers C. Dynamic Testing of Single- and Double-Story Steel-Sheathed Cold-Formed Steel-Framed Shear Walls. Journal of Structural Engineering 2013;139:807–17.

[8] Yu C, Li C. Behavior and strength of cold-formed steel framed shear walls sheathed with composite panels. 21st International Specialty Conference on Cold-Formed Steel Structures, October 24, 2012 - October 25, 2012, Center for Cold-Formed Steel Structures; 2012, p. 637 – 651.

[9] Yu C, Li C. Experimental investigation of cold-formed steel shear walls sheathed with steel-gypsum composite panels. Structural Stability Research Council Annual Stability Conference 2012, April 18, 2012 - April 21, 2012, Structural Stability Research Council (SSRC); 2012, p. 298 – 309.

[10] Nithyadharan M, Kalyanaraman V. Behaviour of cold-formed steel shear wall panels under monotonic and reversed cyclic loading. Thin-Walled Structures 2012;60:12–23.

[11] Peck Q, Rogers N, Serrette R. Cold-Formed Steel Framed Gypsum Shear Walls: In-Plane Response. Journal of Structural Engineering 2012;138:932 – 941.

[12] Liu P, Peterman KD, Yu C, Schafer BW. Cold-formed steel shear walls in ledger-framed buildings. Structural Stability Research Council Annual Stability Conference 2012, April 18, 2012 - April 21, 2012, Structural Stability Research Council (SSRC); 2012, p. 310 – 323.

[13] Liu P, Peterman KD, Yu C, Schafer BW. Characterization of cold-formed steel shear wall behavior under cyclic loading for the CFS-NEES building. 21st International Specialty Conference on Cold-Formed Steel Structures, October 24-25, 2012, Center for Cold-Formed Steel Structures; 2012, p. 703 – 722.

[14] Dastjerdi MZ, Ronagh HR. Seismic performance of steel sheathed cold-formed steel shear walls. 21st International Specialty Conference on Cold-Formed Steel Structures, October 24, 2012 - October 25, 2012, Center for Cold-Formed Steel Structures; 2012, p. 671 – 685.

[15] B. W. Schafer, D. Ayhan, J. Leng, P. Liu, D. A. Padilla-Llano, K. D. Peterman, M. Stehman, S. G. Buonopane, M. R. Eatherton, R. L. Madsen, B. Manley, C. D. Moen, N. Nakata, C. A. Rogers, and C. Yu, "The CFS-NEES Effort: Advancing Cold-Formed Steel Earthquake Engineering," presented at the 10th U.S. National Conference on Earthquake Engineering, Anchorage, AK, 2014.

[16] Peterman K, Nakata N, Schafer B. Cyclic Behavior of Cold-Formed Steel Stud-to-Sheathing Connections. 15th World Conference on Earthquake Engineering, Lisbon, Portugal: 2012.

[17] Okasha A. Performance of steel frame/wood sheathing screw connections subjected to monotonic and cyclic loading. M.Sc. Thesis. University of McGill, 2004.

[18] Ayhan D.and Schafer B.W., Characterization of moment-rotation response of cold-formed steel beams. Proceedings of the Annual Stability conference, SSRC, April 18-21, 2012, Grapevine, Texas.

[19] Madsen, R.L., Nakata, N., and Schafer, B.W., "CFS-NEES Building Structural Design Narrative", Research Report, RR01, access at www.ce.jhu.edu/cfsness, October 2011, revised RR01c May 2012.

[20] K. D. Peterman, M. Stehman, S. G. Buonopane, N. Nakata, R. L. Madsen, and B. W. Schafer, "Stability behavior of full-scale cold-formed steel buildings under seismic excitations," in Structural Stability Research Council Annual Stability Conference 2014, SSRC 2014, March 25-28, 2014.

[21] Lowes, L., Mitra, N., Altoontash, A., *A Beam-Column Joint Model for Simulating the Earthquake Response of Reinforced Concrete Frames*, PEER Report 2003/10, Pacific Earthquake Engineering Research Center., 2004.

[22] AISI-S100-12, North American Specification for the Design of Cold-Formed Steel Structural Members. American Iron and Steel Institute, Washington, D.C. ANSI/AISI-S100-07. 2007.

[23] ABAQUS. ABAQUS Documentation v6.13, Dassault Systèmes Simulia Corp., Providence, RI, USA, 2013.

[24] Mazzoni, S., McKenna, F., Scott, M.H., Fenves, G.L. *Open System for Earthquake Engineering Simulation User Command-Language Manua*l, *OpenSees Version 2.0*, Berkeley, California, 2009.

[25] MATLAB, Version 7.12.0.635. The Mathworks, Inc., www.mathworks.com, 2011.

[26] L.E. McAnallen, D.A. Padilla-Llano, X. Zhao, C.D. Moen, B.W. Schafer, M.R. Eatherton, "Initial Geometric Imperfection Measurement and Characterization of Cold-Formed Steel C-Section Structural Members with 3D Non-Contact Measurement Techniques". Proceedings of the Annual Stability conference, SSRC 2014, March 25-28, 2014, Toronto, Canada.

[27] A. Filiatrault, P. Léger, and R. Tinawi, "On the computation of seismic energy in inelastic structures," Engineering Structures, vol. 16, no. 6, pp. 425–436, 1994.

[28] Zeinoddini VM, Schafer BW. Simulation of geometric imperfections in cold-formed steel members using spectral representation approach. Thin-Walled Structures 2012;60:105–17.

[29] Schafer BW, Pekoz T. Computational modeling of cold-formed steel: characterizing geometric imperfections and residual stresses. Journal of Constructional Steel Research 1998; 47(3):193–210.

[30] FEMA, FEMA 461 - Interim protocols for determining seismic performance characteristics of structural and nonstructural components through laboratory testing, Federal Emergency Management Agency (FEMA), Document No. FEMA 461. 2007.
[31] Higginbotham, A. B., and Hanson, R. D., Axial Hysteretic Behavior of Steel Members. Journal of the Structural Division, 1976; 102(7), 1365-1381.
[32] Ikeda, K., and Mahin, S. A., Cyclic Response of Steel Braces. Journal of Structural Engineering, 1986; 112(2), 342.
[33] Tang, X., and Goel, S. C., Seismic Analysis and Design Considerations of Concentrically Braced Steel Structures. Report No UMCE 87-4, Department of Civil Engineering, The University of Michigan, Ann Arbor, MI. 1987.
[34] Papadrakakis, M., and Loukakis, K., Elastic-plastic hysteretic behaviour of struts with imperfections. Engineering Structures, 1987; 9(3), 162-170.
[35] Nonaka, T., An elastic-plastic analysis of a bar under repeated axial loading." International Journal of Solids and Structures, 1973; 9(5), 569-580.
[36] Sohal, I. S., and Chen, W. F., Local buckling and inelastic cyclic behavior of tubular sections. Thin-Walled Structures, 1988; 6(1), 63-80.
[37] Goel, S. C., Cyclic Post-Buckling Behavior of Steel Bracing Members. Stability and Ductility of Steel Structures Under Cyclic Loading. pp75-84 CRC Press, 1992.
[38] Goggins, J. M., Broderick, B. M., Elghazouli, A. Y., and Lucas, A. S., Behaviour of tubular steel members under cyclic axial loading. Journal of Constructional Steel Research, 2006; 62(1–2), 121-131.
[39] Popov, E. P., and Black, R. G., Steel Struts under Severe Cyclic Loadings. Journal of the Structural Division, 1981; 107(9), 1857-1881.
[40] Jain, A. K., Hanson, R. D., and Goel, S. C., Hysteretic Cycles of Axially Loaded Steel Members. Journal of the Structural Division, 1980; 106(8), 1777-1795.
[41] Popov, E. P., Mahin, Stephen A, and Zayas, V. A., Cyclic Inelastic Buckling of Thin Tubular Columns. Journal of the Structural Division, 1979; 105(11), 2261-2277.
[42] Yao, T., and Nikolov, P. I., Numerical Experiment on Buckling/Plastic Collapse Behavior of Plates under Cyclic Loading. Stability and Ductility of Steel Structures Under Cyclic Loading. pp203-214 CRC Press. 1992.
[43] Usami, T., and Ge, H. B., Cyclic behavior of thin-walled steel structures–numerical analysis. Thin-Walled Structures, 1998; 32(1–3), 41-80.
[44] Watanabe, E., Sugiura, K., Mori, T., and Suzuki, I., Modeling of Hysteretic Behavior of Thin-Walled Box Members. Stability and Ductility of Steel Structures Under Cyclic Loading. pp225-235 CRC Press. 1992.
[45] Calderoni, B., De Martino, A., Formisano, A., and Fiorino, L., Cold formed steel beams under monotonic and cyclic loading: Experimental investigation. Journal of Constructional Steel Research, 2009; 65(1), 219–227.
[46] SSMA Steel Stud Manufacturers Association, Product Technical Information, ICBO ER-4943P, <http://www.ssma.com>, December 15, 2011.
[47] Moen, C. D., Direct strength design for cold-formed steel members with perforations. Ph.D. dissertation, Johns Hopkins University, Baltimore. 2008.
[48] Schafer BW, Adany S. Buckling analysis of cold-formed steel members using CUFSM: conventional and constrained finite strip methods. In: Proceedings of the 18th international specialty conference on cold-formed steel structures. Orlando, FL, United states: University of Missouri-Rolla; 2006.

[49] ASTM. E8M-13, Standard Test Methods for Tension Testing of Metallic Materials (Metric). ASTM International, West Conshohocken, PA. 2004.
[50] Moncarz, P.D., and Krawinkler H., Theory and Application of Experimental Model Analysis in Earthquake Engineering. The John A. Blume Earthquake Engineering Center Report No. 50. 1981.
[51] AISI-S910-08, Test Method for Distortional Buckling of Cold-Formed Steel Hat Shaped Compression Members. American Iron and Steel Institute, Washington, D.C. ANSI/AISI-S910-08. 2008.
[52] Moen CD, Schafer BW. Experiments on cold-formed steel columns with holes. Thin-Walled Structures 2008; 46(10):1164–1182.
[53] Zeinoddini, V. M., Geometric imperfections in cold-formed steel members. Ph.D. dissertation, Johns Hopkins University, Baltimore. 2011.
[54] Padilla-Llano, D.A., Moen, C.D., and Eatherton, M.R., *Energy Dissipation of Thin-Walled Cold-Formed Steel Members*. Virginia Polytechnic Institute and State University Research Report No. CE/VPI-ST-13/06, Blacksburg, VA. 2013.
[55] ASTM-C955, Standard Specification for Load-Bearing (Transverse and Axial) Steel Studs, Runners (Tracks), and Bracing or Bridging for Screw Application of Gypsum Panel Products and Metal Plaster Bases. West Conshohocken, PA. 2009.
[56] Moen, C.D., Igusa, T., and Schafer, B.W., "Prediction of Residual Stresses and Strains in Cold-Formed Steel Members." Thin-Walled Structures, 46(11), 1274-1289, 2008.
[57] VTechWorks, <http://hdl.handle.net/10919/18721> (May, 2012).
[58] M. Wong and K. Chung, “Structural behaviour of bolted moment connections in cold-formed steel beam-column sub-frames,” *Journal of Constructional Steel Research*, vol. 58, no. 2, pp. 253–274, Feb. 2002.
[59] C.-M. Uang, A. Sato, J.-K. Hong, and K. Wood, “Cyclic testing and modeling of cold-formed steel special bolted moment frame connections,” Journal of Structural Engineering, vol. 136, no. 8, pp. 953–960, 2010.
[60] A. Bagheri Sabbagh, M. Petkovski, K. Pilakoutas, and R. Mirghaderi, “Experimental work on cold-formed steel elements for earthquake resilient moment frame buildings,” *Engineering Structures*, vol. 42, pp. 371–386, Sep. 2012.
[61] S. Yin, E. Corona, and M. Ellison, “Degradation and Buckling of I-Beams under Cyclic Pure Bending,” *Journal of Engineering Mechanics*, vol. 130, no. 7, pp. 809–817, 2004.
[62] G. C. Lee and E. T. Lee, “Local buckling of steel sections under cyclic loading,” *Journal of Constructional Steel Research*, vol. 29, no. 1–3, pp. 55–70, 1994.
[63] H.-L. Hsu and P.-S. Chi, “Flexural performance of symmetrical cold-formed thin-walled members under monotonic and cyclic loading,” *Thin-Walled Structures*, vol. 41, no. 1, pp. 47–67, Jan. 2003.
[64] M. Elchalakani, X. Zhao, and R. Grzebieta, “Cyclic Bending Tests to Determine Fully Ductile Section Slenderness Limits for Cold-Formed Circular Hollow Sections,” *Journal of Structural Engineering*, vol. 130, no. 7, pp. 1001–1010, 2004.
[65] P. K. Shaw and S. Kyriakides, “Inelastic analysis of thin-walled tubes under cyclic bending,” *International Journal of Solids and Structures*, vol. 21, no. 11, pp. 1073–1100, 1985.
[66] S. Kyriakides and P. K. Shaw, “Inelastic Buckling of Tubes Under Cyclic Bending,” *J. Pressure Vessel Technol.*, vol. 109, no. 2, pp. 169–178, May 1987.

[67] E. Corona and S. Kyriakides, “An experimental investigation of the degradation and buckling of circular tubes under cyclic bending and external pressure,” *Thin-Walled Structures*, vol. 12, no. 3, pp. 229–263, 1991.
[68] S. P. Vaze and E. Corona, “Degradation and collapse of square tubes under cyclic bending,” *Thin-Walled Structures*, vol. 31, no. 4, pp. 325–341, Aug. 1998.
[69] B. Calderoni, A. De Martino, A. Formisano, and L. Fiorino, “Cold formed steel beams under monotonic and cyclic loading: Experimental investigation,” *Journal of Constructional Steel Research*, vol. 65, no. 1, pp. 219–227, 2009.
[70] B. Calderoni, C. Giubileo, and A. De Martino, “Assessment of hysteretic cyclic behaviour of plastic hinge in cold-formed steel beams,” in *5th International Conference on Behaviour of Steel Structures in Seismic Areas - Stessa 2006, August 14, 2006 - August 17, 2006*, 2006, pp. 185–190.
[71] A. De Martino, A. Formisano, and B. Calderoni, “Flexural cyclic behaviour and low-cycle fatigue of cold-formed steel members,” in *Improvement of Buildings’ Structural Quality by New Technologies*, H. Koukkari, L. Bragança, H. Trumpf, G. de Matteis, F. Mazzolani, C. Schaur, J.-P. Jaspart, and G. Huber, Eds. Taylor & Francis, 2005, pp. 301–309.
[72] EN-1993. Eurocode 3: design of steel structures. European Committee for Standardization. Brussels, Belgium; 2006.
[73] Schafer B.W., Ayham, D., Leng, J., Liu, P., Padilla-Llano, D., Peterman, K., Stehman, M., Buonopane, S.G., Eatherton, M., Madsen, R., Manley, B., Moen, C.D., Nakata, N., Rogers, C., and Yu, C. “The CFS-NEES Effort: Advanced Cold-Formed Steel Earthquake Engineering” Submitted for the Proceedings of the 10th National Conference on Earthquake Engineering, July 21-25 2014, Anchorage Alaska.
[74] AISI-S911-08, Method for Testing Cold-Formed Steel Hat Shaped Beams. American Iron and Steel Institute, Washington, D.C. ANSI/AISI-S911-08. 2008.
[75] VTechWorks, <http://hdl.handle.net/10919/18721> (May, 2012).
[76] B. Put, Y. Pi, and N. Trahair, “Lateral Buckling Tests on Cold-Formed Channel Beams,” *Journal of Structural Engineering*, vol. 125, no. 5, pp. 532–539, 1999.
[77] D. A. Padilla-Llano, C. D. Moen, and M. R. Eatherton, “Cyclic axial response and energy dissipation of cold-formed steel framing members,” *Thin-Walled Structures*, vol. 78, pp. 95–107, 2014.
[78] Ibarra, L.F., Krawinkler H., 2005. *Global collapse of frame structures under seismic excitations*, Report No. 152, The John A. Blume Earthquake Engineering Center.
[79] Lemaitre, Jean and Jean-Louis Chaboche. Mechanics of Solid Materials. 1st ed. Cambridge: Cambridge University Press, 1990. Cambridge Books Online. Web. 22 April 2015. http://dx.doi.org/10.1017/CBO9781139167970.
[80] Y. Bao and T. Wierzbicki, “On fracture locus in the equivalent strain and stress triaxiality space,” *International Journal of Mechanical Sciences*, vol. 46, no. 1, pp. 81–98, Jan. 2004.
[81] Lee, Y.W., Wierzbicki, T., “Quick Fracture Calibration for Industrial Use,” Massachusetts Institute of Technology, Impact & Crashworthiness Laboratory Report No. 115, 2004.
[82] S.G., Buonopane, T.H., Tun, B. W. Schafer, “Fastener-Based Computational Models for Prediction of Seismic Behavior of CFS Shear Walls.” 10th U.S. National Conference on Earthquake Engineering, Anchorage, AK, 2014.
[83] K. D. Peterman, N. Nakata, and B. W. Schafer, “Hysteretic characterization of cold-formed steel stud-to-sheathing connections,” *Journal of Constructional Steel Research*, vol. 101, pp. 254 – 264, Oct. 2014.

[84] Bian, G., Padilla-Llano, D.A., Buonopane, S.G., Moen, C.D., Schafer, B.W., OpenSees modeling of wood sheathed cold-formed steel framed shear walls. Structural Stability Research Council Annual Stability Conference. Nashville, TN, March 24-27, 2015.
[85] Padilla-Llano, D.A., Moen, C.D., Eatherton, M.R., OpenSees simulation of steel column axial cyclic response including local buckling. Structural Stability Research Council Annual Stability Conference. Nashville, TN, March 24-27, 2015.
[86] FEMA, FEMA P58-Seismic Performance Assessment of Buildings, Federal Emergency Management Agency (FEMA), Document No. FEMA 58, Washington, D.C., 2012.
[87] Buonopane, S., Tun, T., and Schafer, B. "Fastener-based computational models for prediction of seismic behavior of CFS shear walls." Proc., Proceedings of the 10th National Conference in Earthquake Engineering.
[88] Liu, P., Peterman, K. D., and Schafer, B. W. (2012). "Test Report on Cold-Formed Steel Shear Walls." CFS-NEES – RR03.
[89] Moen, C. D., Padilla-Llano, D. A., Corner, S., and Ding, C. (2014). "Towards Load-Deformation Models for Screw-Fastened Cold-Formed Steel-to-Steel Shear Connections." 22nd International Specialty Conference on Cold-Formed Steel StructuresSt. Louis, Missouri.
[90] Folz, B., and Filiatrault, A. (2000). "CASHEW—Version 1.0: A computer program for cyclic analysis of wood shear walls." Richmond, California
[91] Foschi, R. O. (1974). "Load-slip characteristics of nails." Wood Sci, 7(1), 69-76.
[92] Ramm, E. (1981). Strategies for tracing the nonlinear response near limit points, Springer.
[93] Judd, J. P., and Fonseca, F. S. (2005). "Analytical model for sheathing-to-framing connections in wood shear walls and diaphragms." Journal of Structural Engineering, 131(2), 345-352.
[94] De Borst, R., Crisfield, M. A., Remmers, J. J., and Verhoosel, C. V. (2012). Nonlinear finite element analysis of solids and structures, John Wiley & Sons.
[95] Peterman, K., and Schafer, B. (2013). "Hysteretic shear response of fasteners connecting sheathing to cold-formed steel studs." Research Report, CFS-NEES, RR04.
[96] Ngo, H. H. (2014). "Numerical and experimental studies Of wood sheathed cold-formed steel framed shear walls." Master of Science in Engineering, Johns Hopkins University, Baltimore, Maryland.
[97] Schafer, B. W., Sangree, R., and Guan, Y. (2007). "Experiments on rotational restraint of sheathing." Report for American Iron and Steel Institute-Committee on Framing Standards. Baltimore, Maryland.
[98] APA (2008). "Panel design specification."
[99] Padilla-Llano, D. A. (2015). "A Framework for Cyclic Simulation of Thin-Walled Cold-Formed Steel Members in Structural Systems.", Ph.D. Dissertation, Virginia Tech, Blacksburg, 2015.

Appendix A Displacement-Controlled Protocol for Cyclic Testing of Cold-Formed Steel Members

Cyclic loading protocols attempt to experimentally simulate deformation demands, cumulative deformation, and the number of inelastic cycles a system (or component) might endure during a design level seismic event [A.1]. The peak axial displacement demand, cumulative displacement demand, and number of inelastic cycles in a particular cold-formed steel member depends on many factors such as the location of the member in the building (e.g., chord studs in a shear wall experience larger axial deformation demands than studs in a typical partition wall), end fixity/constraints (i.e., connections may not fully transfer tension, compression, or moments to the member), bracing conditions, the building's dynamic properties (elastic and nonlinear), and ground motion properties (which can vary depending source characteristics, distance to fault, site characteristics, etc.). Because of the inherent challenges associated with predicting demands on specific CFS members, the displacement-controlled testing protocol adopted here instead focuses on the progression of damage limit states in the member rather than reproducing seismic demands for a specific member configuration.

The loading protocol in Fig. 7.1 was adapted from the FEMA 461 quasi-static cyclic deformation-controlled testing protocol. The FEMA 461 protocol was developed to obtain fragility data and hysteretic response characteristics of building components for which damage is best predicted by imposed deformations [A.2]. Cold-formed steel members can experience symmetrical or asymmetrical loading depending on the end connections (e.g., screwed or welded connection), bracing conditions, and location within a building system (e.g., floor joist compared to a stud in a shear wall). The adapted protocol is fully reversed with symmetric deformation amplitudes in both loading directions. Hysteretic models built based on the responses obtained from this protocol are expected to be capable of capturing the behavior under different loading patterns such as one-sided loading.

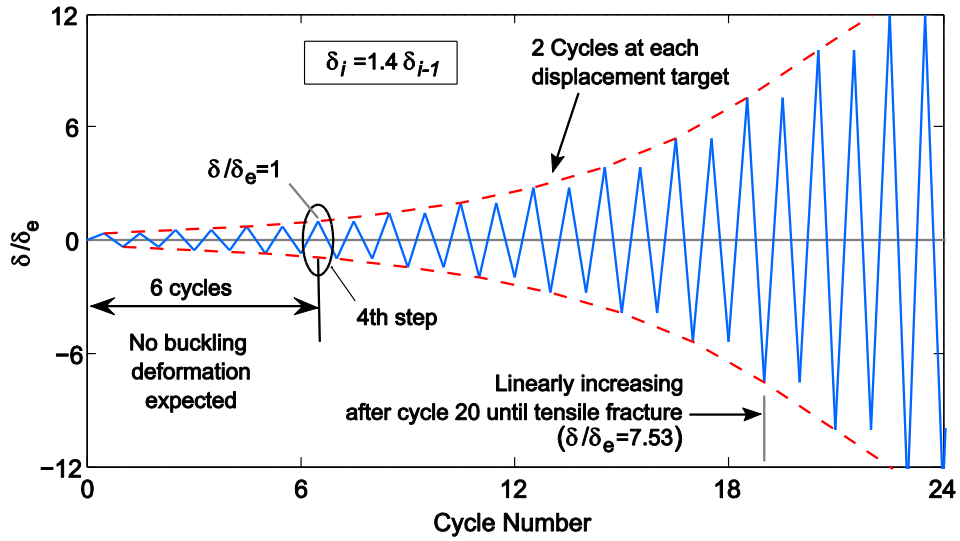

Fig. 7.1. Displacement-controlled testing protocol for cold-formed steel members.

The FEMA 461 protocol is defined to reach a deformation associated with the most severe damage state at a preset point in the loading protocol, such as the 20th cycle. It is also suggested that at least six cycles should be completed prior to reaching the lowest damage state [A.2]. For cold-formed steel members the lowest damage state is assumed to occur when the member stiffness decreases due to buckling deformations. Hence, linear elastic behavior is expected before the corresponding deformation that leads to a reduction of the member initial stiffness. In the adapted protocol this linear behavior is expected to be comprised within the first six cycles (see Fig. 7.1).

The protocol comprises steps of increasing amplitude with two cycles per step. The loading protocol comprises steps of increasing amplitude with two cycles per step. Each step's displacement amplitude is 40% larger than the previous, i.e., $\delta_i = 1.4\delta_{i-1}$, see Fig. 7.1. The loading protocol is anchored to the elastic deformation δ_e at the fourth step (i.e., 7^{th} and 8^{th} cycles). The deformation δ_e is the deformation corresponding to the axial load P_e (axial members) or bending moment M_e associated to with stiffness deterioration due to buckling deformations. The values for P_e and M_e are estimated using slenderness limits defined in the AISI Direct Strength Method (DSM) [A.3].

For CFS axial members, the DSM approach predicts that local buckling deformation initiates at λ_ℓ=0.776 and the distortional buckling deformation initiates at λ_d=0.561. Calculating the slenderness $\lambda=(P_e/P_{cr})^{0.5}$, then P_e=0.60$P_{cr\ell}$ and P_e=0.31P_{crd}. The load where global buckling

deformation influences load-deformation response is assumed to be P_e=0.50P_{cre}. In the axial tests described in [77], the load P_e associated with stiffness deterioration from buckling deformations is given by Eq. A.1.

For CFS flexural members, the DSM approach predicts that local buckling initiates at λ_ℓ=0.776 and distortional buckling initiates at λ_d=0.673. Calculating the slenderness $\lambda=(M_e/M_{cr})^{0.5}$, the moments associated with stiffness degradation from buckling deformations are M_e=0.60$M_{cr\ell}$ and M_e=0.45M_{crd} for local and distortional buckling respectively. The DSM approach estimates that global buckling deformations initiate at M_e=0.36M_{cre}. In the flexural test described in [54], the bending moment M_e associated with stiffness deterioration from buckling deformations is given by Eq. A.2.

$$\delta_e = P_e L / AE \quad \text{A.1}$$

$$\delta_e = aM_e(3L_u + 2a)/6EI \quad \text{A.2}$$

where E is the elastic modulus; A and I are respectively the member area and strong axis moment of inertia; L_u the constant moment span length; a is the shear span.

References

[A.1] Krawinkler, H., "Loading histories for cyclic tests in support of performance assessment of structural components" *The 3rd International Conference on Advances in Experimental Structural Engineering*, October 15-16, 2009, San Francisco, CA. 2009.

[A.2] FEMA, FEMA 461 - Interim protocols for determining seismic performance characteristics of structural and nonstructural components through laboratory testing, Federal Emergency Management Agency (FEMA), Document No. FEMA 461. 2007.

[A.3] AISI-S100-07, North American Specification for the Design of Cold-Formed Steel Structural Members. American Iron and Steel Institute, Washington, D.C. ANSI/AISI-S100-07. 2007.

Appendix B MATLAB Code for *asymPinching* Model

The following MATLAB code illustrates the implementation of the tension-to-compression unloading-reloading path definition for the *asymPinching* model described in Chapter 4. The variables in this code follow the same definitions in the original *Pinching4* model. A compiled version of the *asymPinching* model for OpenSees 2.4.5 can be downloaded from http://edcfs.blogspot.com/aTWSection.

```
function [state3Strain,state3Stress] =
getstate3mod(state3Strain,state3Stress,kunload,kElasticNegDamgd,lowTstateStrain,lowTstateStress,
TminStrainDmnd, envlpNegStrain,envlpNegDamgdStress,hghTstateStrain,hghTstateStress,MDL)
    %=========================================================================
    % File Name: getstate3.m
    % Description: Defines the tension-to-compression unloading path using
    %              trial strain and strain rate, especially for state 3.
    %
    %                          Padilla-Llano David (Dec 2014) - dapadill@vt.edu
    %=========================================================================
    kmax = max([kunload kElasticNegDamgd]);
    TperElong = -(state3Stress(4) - kunload*state3Strain(4))/kunload;

    if (state3Strain(1)*state3Strain(4) <0.0) % Trilinear unload reload path expected
        % Calculate Point at 3:-> End of Unloading from Negative Quadrant
        if (TminStrainDmnd < envlpNegStrain(4))
            state3Stress(3) = MDL.uForceN*envlpNegDamgdStress(5);
        elseif (TminStrainDmnd < envlpNegStrain(3))
            state3Stress(3) = MDL.uForceN*envlpNegDamgdStress(4);
        else
            state3Stress(3) = MDL.uForceN*envlpNegDamgdStress(3);
        end

        state3Strain(3) = hghTstateStrain + (-hghTstateStress + state3Stress(3))/kunload;

        % Check Strain at 3 is not in front of Strain at 4
        if (state3Strain(3) > state3Strain(4))
            state3Strain(3) = state3Strain(4) + (state3Stress(3) - state3Stress(4))/kunload;
        end

        %%% Calculate Point at 2:-> Peak in the Unload-Reload path
        if (MDL.uForceN == 0.0)
            state3Stress(2) = lowTstateStress*MDL.rForceN;
        elseif (MDL.rForceN-MDL.uForceN > 1e-8)
            state3Stress(2) = lowTstateStress*MDL.rForceN;
        else
            if (TminStrainDmnd < envlpNegStrain(4))
                st1 = lowTstateStress*MDL.uForceN*(1.0+1e-6);
                st2 = envlpNegDamgdStress(5)*(1.0+1e-6);
                state3Stress(2) = min([st1 st2]);
            elseif (TminStrainDmnd < envlpNegStrain(3))
                st1 = lowTstateStress*MDL.uForceN*(1.0+1e-6);
                st2 = envlpNegDamgdStress(4)*(1.0+1e-6);
                state3Stress(2) = min([st1 st2]);
            else
                st1 = envlpNegDamgdStress(3)*MDL.uForceN*(1.0+1e-6);
                st2 = envlpNegDamgdStress(5)*(1.0+1e-6);
                state3Stress(2) = min([st1 st2]);
            end
        end
```

```
        % Check that Stress is less than the maximum stress from damaged backbone
        if (state3Stress(2) < envlpNegDamgdStress(3))
            state3Stress(2) = envlpNegDamgdStress(3);
        end

        state3Strain(2) = TperElong + envlpNegStrain(3)*MDL.rDispN;

        % Correct Strain at 2 if reload stiffness exceeds kunload or is negative
        k23 = (state3Stress(2)-state3Stress(3))/(state3Strain(2)-state3Strain(3));
        k13 = (state3Stress(1)-state3Stress(3))/(state3Strain(1)-state3Strain(3));

        if ((state3Strain(2) > state3Strain(3)))
            state3Strain(2) = state3Strain(3) + (state3Stress(2) - state3Stress(3))/kunload;
        elseif (k23 > kunload)
            state3Strain(2) = state3Strain(3) + (state3Stress(2) - state3Stress(3))/kunload;
        elseif ( k23 < 0 )
            % Point 3 should be lower than Point 3
            df = abs(state3Stress(3)/1000);
            state3Stress(2) = state3Stress(3) - df;
            if ( k23 < k13 )
                % pt 2 should be along a line between 1 and 3
                du = state3Strain(1)-state3Strain(3);
                df = state3Stress(1)-state3Stress(3);
                state3Strain(2) = state3Strain(3) + 0.5*du;
                state3Stress(2) = state3Stress(3) + 0.5*df;
            end
        end
    else
        % linear unload reload path is expected
        du = state3Strain(4)-state3Strain(1);
        df = state3Stress(4)-state3Stress(1);
        state3Strain(2) = state3Strain(1) + 0.33*du;
        state3Strain(3) = state3Strain(1) + 0.67*du;
        state3Stress(2) = state3Stress(1) + 0.33*df;
        state3Stress(3) = state3Stress(1) + 0.67*df;
    end

    % checkslope and slope are local variables
    checkSlope = state3Stress(4)/state3Strain(4);
    slope = 0.0;
    % Final Check: Enforces monotonic Increasing Load-Response through
    % State 4 if TperElong is zero
    i = 1;
    while (i<4)
        du = state3Strain(i+1)-state3Strain(i);
        df = state3Stress(i+1)-state3Stress(i);
        if (du<0.0 || df<0.0) && (TperElong <= 0)
            du = state3Strain(4)-state3Strain(1);
            df = state3Stress(4)-state3Stress(1);
            state3Strain(2) = state3Strain(1) + 0.33*du;
            state3Strain(3) = state3Strain(1) + 0.67*du;
            state3Stress(2) = state3Stress(1) + 0.33*df;
            state3Stress(3) = state3Stress(1) + 0.67*df;
            slope = df/du;
            i = 4;
        end
        % If the slope from Start to End of State 4 is less than the slope
        % from zero to point 1 of state4 then unload to zero and load
        % linearly to point 4 of state4
        if (slope > 1e-8 && slope < checkSlope)
            state3Strain(2) = 0.0;
            state3Stress(2) = 0.0;
            state3Strain(3) = state3Strain(4)/2;
            state3Stress(3) = state3Stress(4)/2;
        end
        i = i + 1;
    end
end
```

Appendix C Connection Response in ABAQUS Pushover Analysis

The following figures shows screw-fastened connection force with respect to shear wall lateral displacement. Only those that are reported to have failed during shear experiment are shown here. The Fig. C.2, Fig. C.3 and Fig. C.4 shows failed connections at different locations, namely left stud bottom, right stud bottom and bottom track. The dashed lines in the these figures labels the specific shear wall lateral displacement corresponding to the initiation and end of shear wall load-deformation curve “legs”.

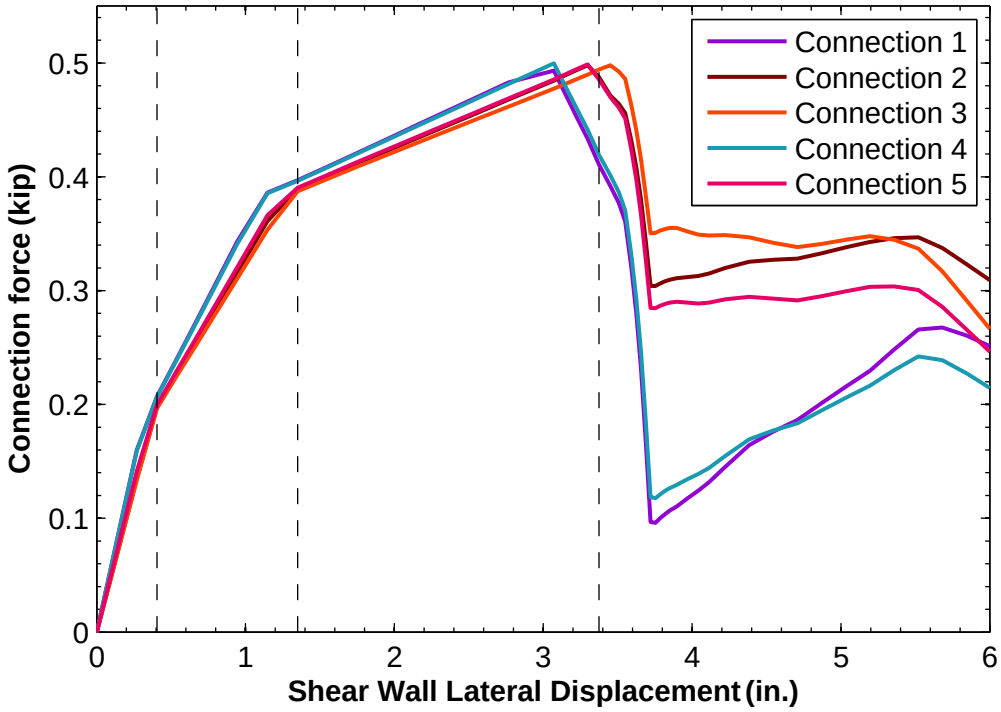

Fig. C.2. Force of left stud bottom connections a shear wall lateral displacement

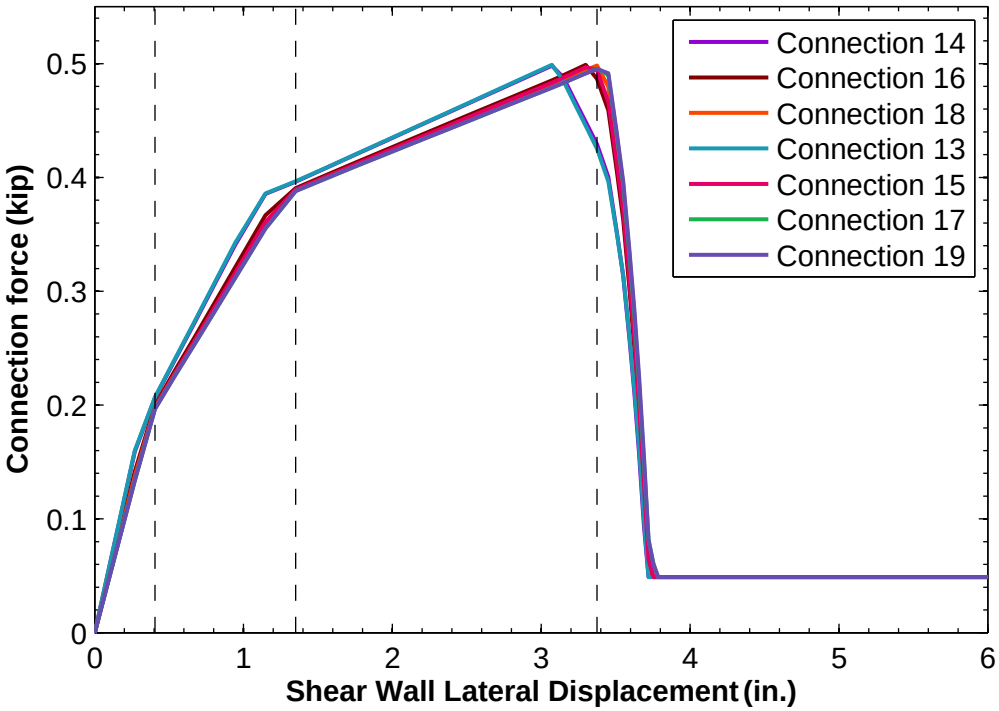

Fig. C.3. Force of right stud bottom connections against shear wall lateral displacement

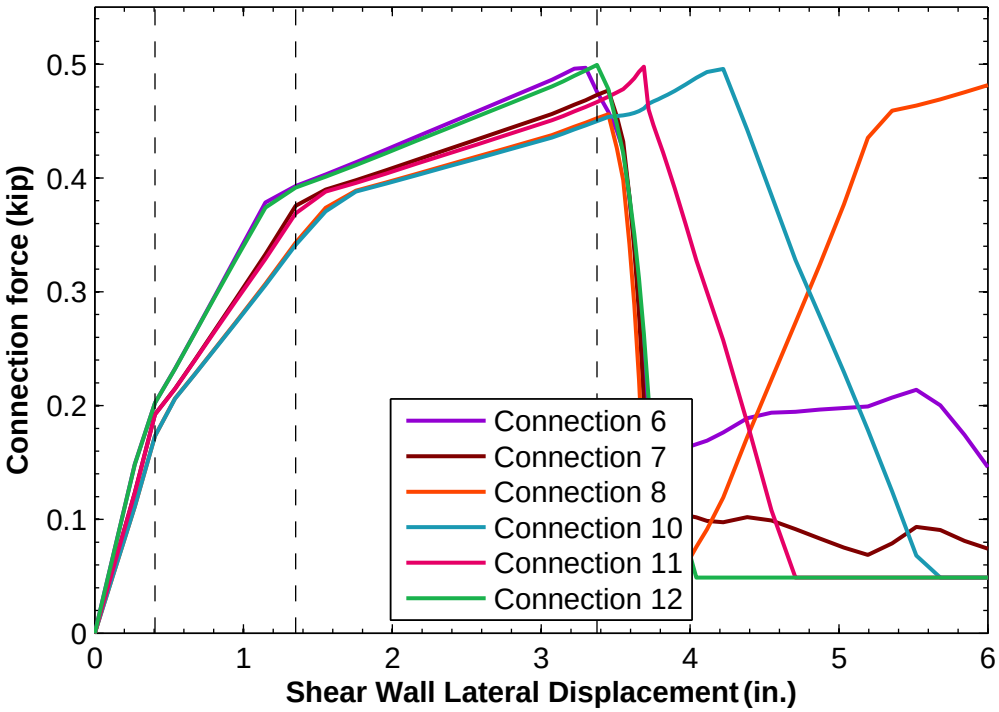

Fig. C.4. Force of bottom track connections against shear wall lateral displacement

Appendix D User Element FORTRAN Code for screw-fastened connection simulation in ABAQUS

The following is the FORTRAN code corresponding to the UEL subroutine for fastened connection simulation in ABAQUS.

```
      SUBROUTINE UEL(RHS,AMATRX,SVARS,ENERGY,NDOFEL,NRHS,NSVARS,
     +     PROPS,NPROPS,COORDS,MCRD,NNODE,U,DU,V,A,JTYPE,TIME,DTIME,
     +     KSTEP,KINC,JELEM,PARAMS,NDLOAD,JDLTYP,ADLMAG,PREDEF,
     +     NPREDF,LFLAGS,MLVARX,DDLMAG,MDLOAD,PNEWDT,JPROPS,NJPROP,
     +     PERIOD)
C     ************************************************************
      INCLUDE 'ABA_PARAM.INC'
C
      PARAMETER (TOL = 1.D-128, ZERO = 0.D0, PONE = 0.1D0, HALF = 0.5D0,
     + ONE = 1.D0, TWO = 2.D0)
C
      DIMENSION RHS(MLVARX,*),AMATRX(NDOFEL,NDOFEL),PROPS(*),
     1 SVARS(*),ENERGY(8),COORDS(MCRD,NNODE),U(NDOFEL),
     2 DU(MLVARX,*),V(NDOFEL),A(NDOFEL),TIME(2),PARAMS(*),
     3 JDLTYP(MDLOAD,*),ADLMAG(MDLOAD,*),DDLMAG(MDLOAD,*),
     4 PREDEF(2,NPREDF,NNODE),LFLAGS(*),JPROPS(*)
C
      DIMENSION SRESID(4)
      DIMENSION SPR_AMATRX(4,4), SPR_SRESID(4)
C
      DOUBLE PRECISION SPR_LEN, SPR_DISP
      DOUBLE PRECISION SPR_COS_X, SPR_COS_Y
      DOUBLE PRECISION SPR_DISP_X, SPR_DISP_Y
      DOUBLE PRECISION SPR_K, SPR_F
      DOUBLE PRECISION SPR_SGN
      DOUBLE PRECISION SPR_K_X, SPR_K_Y
      DOUBLE PRECISION SPR_F_X, SPR_F_Y
C
      DOUBLE PRECISION SPR_K_SEC, SPR_K_SEC_X, SPR_K_SEC_Y
C
      DOUBLE PRECISION SPR_ORIENT_1, SPR_ORIENT_2
C
      DOUBLE PRECISION SPR_DISP1, SPR_DISP2, SPR_F1, SPR_F2, SPR_ENERGY
      DOUBLE PRECISION SPR_DISP_X1, SPR_DISP_X2, SPR_DISP_Y1, SPR_DISP_Y2
      DOUBLE PRECISION SPR_F_X1, SPR_F_X2, SPR_F_Y1, SPR_F_Y2
      DOUBLE PRECISION SPR_ENERGY_X, SPR_ENERGY_Y
C
      INTEGER I_SPR_NUM
      INTEGER KPNT, KSEC, KORIENT
C
      CHARACTER FILENAME*200
      CHARACTER*(*) FILEPATH
C
C     --------------                  Choose spring data output path
C
*************************************************************************************************
      PARAMETER (FILEPATH = E:\')
C
*************************************************************************************************
C
C     --------------                  Select your spring type                          -----------
-
C
*************************************************************************************************
C     * 1: Radial spring, 2: Coupled-spring pair, 3: Uncoupled spring pair
      KPNT = 3
C     * 0: Tangent stiffness, 1: Secant stiffness
      KSEC = 0
```

```
C     * 0: Default deformation quadrants, 1: Displacement-based deformation quadrants
      KORIENT = 1
C     * 0:  Forbid spring data output, 1: Permit spring data output
      KOUTPUT = 1
C
*******************************************************************************************
C
C     Specify fastener mass
      AM   = 4.5D-5
C
C     Initialize vector variables
      DO K1 = 1, NDOFEL
          SRESID(K1) = ZERO
          SPR_SRESID(K1) = ZERO
          DO KRHS = 1, NRHS
              RHS(K1,KRHS) = ZERO
          END DO
          DO K2 = 1, NDOFEL
              AMATRX(K1, K2) = ZERO
              SPR_AMATRX(K1,K2) = ZERO
          END DO
      END DO
C
C     Initialize scalar variables
      SPR_DISP_X = ZERO
      SPR_DISP_Y = ZERO
      SPR_K_X = ZERO
      SPR_K_Y = ZERO
      SPR_F_X = ZERO
      SPR_F_Y = ZERO
C
C     ***************** Generate spring geometry info. ****************
      IF (KPNT .EQ. 1) THEN
C     * Radial-spring model
          CALL
SGEOM(U,COORDS,SPR_LEN,SPR_DISP,SPR_COS_X,SPR_COS_Y,SPR_DISP_X,SPR_DISP_Y,PROPS,SVARS)
      ELSE IF (KPNT. EQ. 2) THEN
C     * Coupled-spring model
          CALL SGEOM_CUP(U,SPR_DISP,SPR_COS_X,SPR_COS_Y,SPR_DISP_X,SPR_DISP_Y)
      ELSE
C     * 2-spring model
          CALL
SGEOM(U,COORDS,SPR_LEN,SPR_DISP,SPR_COS_X,SPR_COS_Y,SPR_DISP_X,SPR_DISP_Y,PROPS,SVARS)
      END IF
C
C     ***************** Save spring original orientation ****************
*     * Set up spring positive/negative deformation rule
C     * Only applicable to radial spring/coupled spring model
      IF (KPNT .EQ. 1 .OR. KPNT .EQ. 2) THEN
C         * Deformation quadrant based on initial displacement
          IF (KORIENT .EQ. 1) THEN
              IF (SVARS(128) .NE. ONE) THEN
C                 * Use default deformation quadrant when deformation is "zero"
                  IF (DABS(SPR_DISP) .LE. TWO * TOL) THEN
                      SVARS(129) = 1.D0/DSQRT(2.D0)
                      SVARS(130) = 1.D0/DSQRT(2.D0)
                  ELSE
C                 * Now use displacement-based quadrant
C                     * Save spring orientation
                      SVARS(129) = SPR_COS_X
                      SVARS(130) = SPR_COS_Y
C                     * Keep spring orientation quadrant fixed now
                      SVARS(128) = SVARS(128) + ONE
                  END IF
              END IF
C             * Retrieve spring orientation
              SPR_ORIENT_1 = SVARS(129)
              SPR_ORIENT_2 = SVARS(130)
C         * Default deformation quadrant
          ELSE
              SPR_ORIENT_1 = 1.D0/DSQRT(2.D0)
```

```
            SPR_ORIENT_2 = 1.D0/DSQRT(2.D0)
        END IF
      END IF
C
C     ***************** Adjust spring deformation sign ****************
C     * Only applicable to radial spring/coupled spring model
      IF (KPNT .EQ. 1 .OR. KPNT .EQ. 2) THEN
        SPR_SGN = ONE
C       * For the case of "real compression"
        IF (SPR_DISP .LT. ZERO) THEN
            SPR_SGN = ONE
C       * For the case of "fake compression" determined by deformation quadrants
        ELSE IF (SPR_DISP_X .NE. ZERO .AND. SPR_DISP_Y .NE. ZERO) THEN
            IF (SPR_ORIENT_1 * SPR_DISP_X + SPR_ORIENT_2 * SPR_DISP_Y .LT. ZERO) THEN
                SPR_SGN = -ONE
            END IF
        END IF
C       * Spring deformation is assinged with positive or negative sign
        SPR_DISP = SPR_SGN * SPR_DISP
      END IF
C
C     ***************** Get spring stiffness and force from nonlinear model ****************
      IF (KPNT .EQ. 1 .OR. KPNT. EQ. 2) THEN
C       Use tangent stiffness definition
        I_SPR_NUM = 1
        CALL PINCHING4(PROPS,SVARS,SPR_DISP,SPR_K,SPR_F,KINC,I_SPR_NUM)
C
C       Use secant stiffness definition
        IF (KSEC .EQ. 1 .AND. DABS(SPR_DISP) .GE. TOL) THEN
            SPR_K_SEC = SPR_F / SPR_DISP
            SPR_K = SPR_K_SEC
        END IF
      ELSE
C       Use tangent stiffness definition
        I_SPR_NUM = 1
        CALL PINCHING4(PROPS,SVARS,SPR_DISP_X,SPR_K_X,SPR_F_X,KINC,I_SPR_NUM)
C
        I_SPR_NUM = 2
        CALL PINCHING4(PROPS,SVARS,SPR_DISP_Y,SPR_K_Y,SPR_F_Y,KINC,I_SPR_NUM)
C
C       Use secant stiffness definition
        IF (KSEC .EQ. 1. AND. DABS(SPR_DISP_X) .GE. TOL .AND. DABS(SPR_DISP_Y) .GE. TOL) THEN
            SPR_K_SEC_X = SPR_F_X / SPR_DISP_X
            SPR_K_SEC_Y = SPR_F_Y / SPR_DISP_Y
            SPR_K_X = SPR_K_SEC_X
            SPR_K_Y = SPR_K_SEC_Y
        END IF
      END IF
C
C     ***************** Generate stiffness matrix and residual force vector ****************
C     * Radial spring model
      IF (KPNT .EQ. 1) THEN
        CALL SAMATRX(SPR_AMATRX, SPR_K, SPR_F, SPR_LEN, SPR_COS_X, SPR_COS_Y, SPR_SGN)
        CALL SNFORCE(SPR_F, SPR_COS_X, SPR_COS_Y, SPR_SRESID, SPR_SGN)
C     * Coupled spring model
      ELSE IF (KPNT .EQ. 2) THEN
        CALL SAMATRX_CUP(SPR_AMATRX, SPR_K)
        CALL SNFORCE(SPR_F, SPR_COS_X, SPR_COS_Y, SPR_SRESID, SPR_SGN)
C     * Uncoupled 2-spring model
      ELSE
        CALL SAMATRX_2(SPR_AMATRX, SPR_K_X, SPR_K_Y)
        CALL SFORCE_2(SPR_SRESID, SPR_F_X, SPR_F_Y)
      END IF
C
C     ***************** Update energy ****************
      IF (KPNT .EQ. 1 .OR. KPNT .EQ. 2) THEN
        SVARS(141) = SVARS(142)         ! Deformation for last increment
        SVARS(142) = SPR_DISP           ! Deformation at current increment
        SVARS(143) = SVARS(144)         ! Spring force from last increment
        SVARS(144) = SPR_F              ! Spring force at current increment
C
```

```
          SPR_DISP1 = SVARS(141)
          SPR_DISP2 = SVARS(142)
          SPR_F1 = SVARS(143)
          SPR_F2 = SVARS(144)
          SPR_ENERGY = HALF * (SPR_F2 + SPR_F1) * (SPR_DISP2 - SPR_DISP1)
          SVARS(145) = SVARS(145) + SPR_ENERGY
      ELSE
          SVARS(141) = SVARS(142)
          SVARS(142) = SPR_DISP_X
          SVARS(143) = SVARS(144)
          SVARS(144) = SPR_DISP_Y
          SVARS(146) = SVARS(147)
          SVARS(147) = SPR_F_X
          SVARS(148) = SVARS(149)
          SVARS(149) = SPR_F_Y
C
          SPR_DISP_X1 = SVARS(141)
          SPR_DISP_X2 = SVARS(142)
          SPR_DISP_Y1 = SVARS(143)
          SPR_DISP_Y2 = SVARS(144)
          SPR_F_X1 = SVARS(146)
          SPR_F_X2 = SVARS(147)
          SPR_F_Y1 = SVARS(148)
          SPR_F_Y2 = SVARS(149)
          SPR_ENERGY_X = HALF * (SPR_F_X2 + SPR_F_X1) * (SPR_DISP_X2 - SPR_DISP_X1)
          SPR_ENERGY_Y = HALF * (SPR_F_Y2 + SPR_F_Y1) * (SPR_DISP_Y2 - SPR_DISP_Y1)
          SPR_ENERGY = SPR_ENERGY_X + SPR_ENERGY_Y
          SVARS(145) = SVARS(145) + SPR_ENERGY
      END IF
C
C     ***************** ABAQUS/Standar analysis procedures ****************
      IF (LFLAGS(3) .EQ. 1) THEN
C         * General static analysis
          IF (LFLAGS(1) .EQ.1 .OR. LFLAGS(1) .EQ. 2) THEN
              DO K1 = 1, 4
                  DO K2 = 1,4
                      AMATRX(K1,K2) = SPR_AMATRX(K1,K2)
                  END DO
                  SRESID(K1) = SPR_SRESID(K1)
                  RHS(K1,1) = RHS(K1,1) - SRESID(K1)
                  ENERGY(2) = SVARS(145)
              END DO
C         * Dynamic analysis (implicit)
          ELSE IF (LFLAGS(1).EQ.11 .OR. LFLAGS(1).EQ.12) THEN
              ALPHA = PARAMS(1)
              BETA  = PARAMS(2)
              GAMMA = PARAMS(3)
              DADU = ONE/(BETA*DTIME**2)
              DVDU = GAMMA/(BETA*DTIME)
C
              DO K1 = 1, NDOFEL
                  AMATRX(K1,K1) = AM*DADU
                  RHS(K1,1) = RHS(K1,1)-AM*A(K1)
              END DO
C
              DO K1 = 1, NDOFEL
                  DO K2 = 1, NDOFEL
                      AMATRX(K1,K2) = AMATRX(K1,K2) + SPR_AMATRX(K1,K2)*(ONE+ALPHA)
                  END DO
                  SRESID(K1) = SPR_SRESID(K1)
              END DO
C
              DO K1 = 1, NDOFEL
                  RHS(K1,1) = RHS(K1,1) - ((ONE+ALPHA)*SRESID(K1)-ALPHA*SVARS(150+K1))
              END DO
C
              ENERGY(1) = ZERO
              DO K1 = 1, NDOFEL
                  SVARS(K1+154) = SVARS(K1+150)
                  SVARS(K1+150) = SRESID(K1)
                  ENERGY(1) = ENERGY(1)+HALF*V(K1)*AM*V(K1)
```

```
            END DO
C
            ENERGY(2) = SVARS(145)
        END IF
C     * Define stiffness matrix only
      ELSE IF (LFLAGS(3) .EQ. 2) THEN
        DO K1 = 1, 4
            DO K2 = 1,4
                AMATRX(K1,K2) = SPR_AMATRX(K1,K2)
            END DO
        END DO
C     * Define mass matrix
      ELSE IF (LFLAGS(3) .EQ. 4) THEN
        DO K1 = 1, NDOFEL
            DO K2 = 1, NDOFEL
                AMATRX(K1,K2) = ZERO
            END DO
        END DO
        DO K1 = 1, NDOFEL
            AMATRX(K1,K1) = AM
        END DO
C     * Half-step residual calculation
      ELSE IF (LFLAGS(3) .EQ. 5) THEN
        ALPHA = PARAMS(1)
        DO K1 = 1, NDOFEL
            SRESID(K1) = SPR_SRESID(K1)
        END DO
        DO K1 = 1, NDOFEL
            RHS(K1,1) = RHS(K1,1)-AM*A(K1)-(ONE+ALPHA)*SRESID(K1) +
     + HALF*ALPHA*(SVARS(K1+150)+SVARS(K1+154))
        END DO
C     * Initial acceleration calculation
      ELSE IF (LFLAGS(3) .EQ. 6) THEN
        DO K1 = 1, NDOFEL
            AMATRX(K1,K1) = AM
            SRESID(K1) = SPR_SRESID(K1)
        END DO
        DO K1 = 1, NDOFEL
            RHS(K1,1) = RHS(K1,1)-SRESID(K1)
        END DO
        ENERGY(1) = ZERO
        DO K1 = 1, NDOFEL
            SVARS(K1+150) = SRESID(K1)
            ENERGY(1) = ENERGY(1)+HALF*V(K1)*AM*V(K1)
        END DO
        ENERGY(2) = SVARS(145)
      END IF
C
C     **************** Ouput spring data ****************
C     * Uncoupled 2-spring model
800   FORMAT(I10, F20.8, F20.8, F20.8, F20.8, F20.8, F20.8, F20.8, F20.8)
C
C     * Radial spring/coupled spring model
900   FORMAT(I10, F20.8, F20.8, F20.8, F20.8, F20.8, F20.8, F20.8, F20.8, F20.8, F20.8)
C
      IF (KOUTPUT .EQ. 1) THEN
        IF (KINC .GE. 1) THEN
            WRITE(FILENAME, fmt='(a, I0, a)') FILEPATH, JELEM, ".txt"
            OPEN(300, FILE=FILENAME, STATUS='UNKNOWN', POSITION='APPEND')
            IF (KPNT .EQ. 1 .OR. KPNT .EQ. 2) THEN
                WRITE(300, 900) KINC, TIME(2), SPR_DISP, SPR_F, SPR_K, ENERGY(2),
     +SPR_SGN, SPR_COS_X, SPR_COS_Y, SPR_DISP_X, SPR_DISP_Y
            ELSE
                WRITE(300, 800) KINC, TIME(2), SPR_DISP_X, SPR_K_X, SPR_F_X,
     +SPR_DISP_Y, SPR_K_Y, SPR_F_Y, ENERGY(2)
            END IF
            CLOSE(300)
        END IF
      END IF
C
      RETURN
```

```
END
```

American Iron and Steel Institute

25 Massachusetts Avenue, NW
Suite 800
Washington, DC 20001

www.steel.org

Research Report RP15-3

The New Steel